Fiber Sensing Based on New Structures and Post-Processing Enhancement

Marta Sofia dos Anjos Ferreira
Physics
Physics Department
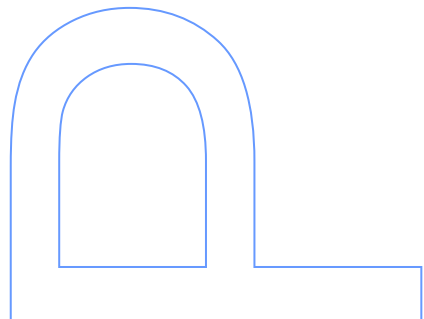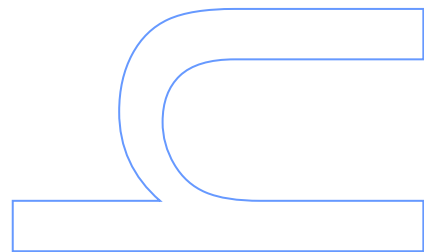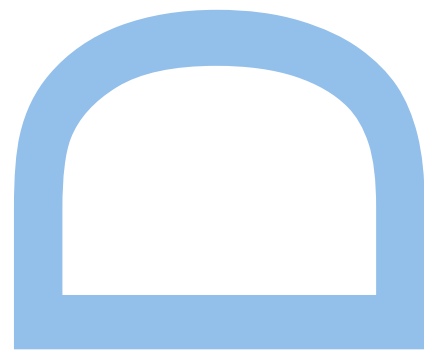2015

Supervisor
Orlando José dos Reis Frazão, Invited Assistant Professor, FCUP

Co-supervisor
José Luís Campos de Oliveira Santos, Full Professor, FCUP

FACULDADE DE CIÊNCIAS DA UNIVERSIDADE DO PORTO

FIBER SENSING BASED ON NEW STRUCTURES

AND POST-PROCESSING ENHANCEMENT

Marta Sofia dos Anjos Ferreira

Thesis submitted to Faculdade de Ciências da Universidade do Porto in partial
fulfillment of the requirements for the degree of Ph.D. in Physics

This Thesis was conducted under the supervision of

Dr. Orlando José dos Reis Frazão

Invited Assistant Professor of Departamento de Física e Astronomia da

Faculdade de Ciências da Universidade do Porto

and

Prof. Dr. José Luís Campos de Oliveira Santos

Full Professor of Departamento de Física e Astronomia da Faculdade

de Ciências da Universidade do Porto

Dedicated to my Mom

ACKNOWLEDGMENTS

I would like to express my deepest gratitude to my supervisor, Dr. Orlando Frazão, for challenging me to pursue the dream of performing investigation in a highly technological field. His help, his knowledge and insight were decisive for the development of this work. To my co-supervisor, Professor José Luís Santos, who was a source of inspiration ever since I started working at INESC. His wise words and the valuable discussions allowed me to grow not only as a physicist, but also as a human being. Thank you, Professor.

Professor António Pereira Leite thank you for all the valuable help in reviewing this Thesis.

I would also like to acknowledge all my colleagues at INESC, companions on this journey, who gave me constant care and supported me right from start. Many thanks, Ricardo Silva, Paula Tafulo, Luís Coelho, Raquel Queirós, Carlos Gouveia, Paulo Caldas, João Moura, Ivo Nascimento, Rita Ribeiro, Susana Silva and Lídia Carvalho. Thank you, Paulo Roriz and Ricardo André, for those wonderful days in the lab. A special hug for you both! You rock!

Thanks to all the senior researchers at INESC for the constant support and attention. To dearest Luísa, such an important figure in our *inescian* lives! Thank you all for the kind words, the smiles, the help and patience.

Throughout this four-year journey, I was fortunate to travel and meet different research groups. I would like to acknowledge Professor Kate Sugden, from the group of Aston Institute of Photonic Technologies, in Birmingham, England. I would also like to thank Dr. Graham Lee and Dr. Neil Gordon. It was such a pleasure to work with you! To Dr. Kaiming Zhou, my deepest thanks for making the lab available for me. Finally, I would like to thank Dr. Mykhaylo Dubov, for the cup of tea and the discussion that changed the way I saw my research.

To my dearest German friends at the Leibnitz Institute of Photonic Technology, in Jena, I am profoundly grateful. To Dr. Kay Schuster, who always welcomed and trusted in me. Thanks to Dr. Jörg Bierlich, for all the nice moments, the conversations and

knowledge sharing. Thanks to Dr. Jens Kobelke, for all the valuable discussions, and for always trying to meet my requests. Thanks to Dr. Martin Becker, for helping in the writing of the fiber Bragg gratings. My deepest thanks to Dr. Anka Schwuchow, to Mathias, to Lara and Lena, for making me feel so welcome.

I would also like to acknowledge INESC TEC, namely the Center for Applied Photonics for receiving me and providing the all the necessary work conditions.

This PhD would have not been possible to accomplish without the doctoral fellowship from the Fundação para a Ciência e Tecnologia (SFRH/BD/76965/2011). The collaborations with the foreign institutions, namely the short missions abroad, were possible due to the support provided by the COST Action TD1001 (OFSeSa). Two of the short missions at the IPHT-Jena were supported by the bilateral cooperation between the Portuguese and the German academic exchange service funding agency (FCT/DAAD).

To my friends, who were present in the several stages of my life, there are no words to express my gratitude. To my friend Teresa, who flew away to the Netherlands to conquer her dreams, but it's like she is still here. To André, even in Germany he is still extremely present in my life. To Otílio, it's hard for me to find the words to express how much he means to me.

Lastly, I would like to thank my family, to my Dad and Luísa, to my brother and to my sister-in-law. To my niece, Joana, who makes my life so much brighter. Finally, thank you Mum for being there, supporting and advising me all the way!

RESUMO

O trabalho descrito nesta Tese de Doutoramento foca-se no pós-processamento de fibra ótica e na sua otimização como elemento sensor. Uma vez que a maioria dos sensores apresentados se baseia em interferómetros de Fabry-Perot, é apresentada uma perspetiva histórica do desenvolvimento deste tipo de sensores em fibra. Esta revisão contempla os trabalhos publicados desde os primeiros anos, no início da década de 1980, até meados de 2015.

A incorporação de microcavidades na ponta de uma fibra monomodo foi alvo de intenso estudo, particularmente para a medição de pressão de nitrogénio e metano no estado gasoso. Essas cavidades foram fabricadas a partir de tubos de sílica ocos e de fibra de cristal fotónico de núcleo oco. Seguindo uma abordagem diferente, fabricaram-se microcavidades entre duas secções de fibra monomodo. Neste caso, destaca-se a baixa sensibilidade à temperatura, que as torna altamente desejáveis para medição de deformação a temperaturas elevadas.

Competências em técnicas de pós-processamento como o ataque químico e a escrita de estruturas periódicas no núcleo da fibra por meio de laser de excímeros ou laser de femtosegundo foram adquiridas e aprofundadas no decorrer do programa doutoral.

Um dos trabalhos consistiu no desenho e fabrico de uma fibra de bainha dupla, cujo índice de refração da bainha interior é superior ao da bainha exterior e ao do núcleo. Deste modo, inicialmente a luz era guiada pela bainha interior e não pelo núcleo. Após efetuar pós-processamento através do ataque químico, a bainha interior foi removida e a luz passou a propagar-se pelo núcleo. Duas aplicações foram encontradas para esta fibra, como sensor de temperatura e como refratómetro ótico, cuja fase varia com o índice de refração de um líquido.

Dois tipos de redes de Bragg em fibra ótica foram caracterizados em deformação e temperatura. A primeira técnica consistiu na inscrição de estruturas sensoras na ponta de uma fibra por meio de um laser de excímeros e recorrendo a uma máscara de fase. Estes elementos foram posteriormente sujeitos a ataque químico. Obtiveram-se extremidades de fibra com dimensões muito reduzidas, com uma sensibilidade à

deformação muito elevada. A outra técnica utilizada para o fabrico das redes de Bragg foi a escrita ponto-a-ponto por meio de um laser de femtosegundo. Neste caso, estes elementos sensores são muito estáveis a temperaturas elevadas e podem ser usados para medir deformação em situações adversas.

A aplicação de lasers em fibra ótica como elementos sensores também foi considerada nesta Tese. Foram estudados dois lasers, um baseado na configuração em anel e outro baseado numa cavidade figura-de-oito. Destes trabalhos é de salientar a qualidade da emissão laser, nomeadamente a sua razão sinal-ruido, a reduzida largura a meia altura e a estabilidade do laser, o que permitiu fazer a medição de diferentes parâmetros físicos como deformação, temperatura e torção.

Por fim, abordou-se a possibilidade de utilizar microesferas como dispositivos de sensorização. Através do arco elétrico produzido pela máquina de fusão, é possível criar microesferas na extremidade de uma fibra ótica. Inclusivamente, através da mesma técnica, podem obter-se cadeias de microsferas, formando interferómetros do tipo Mach-Zehnder, sensíveis a diferentes parâmetros físicos como deformação e temperatura. Os resultados preliminares obtidos usando uma estrutura de suporte para microesferas de sílica foram também apresentados. Neste caso, os sensores foram sujeitos a variações de temperatura.

Todo o trabalho experimental foi conjugado com as respectivas considerações teóricas. Muitas questões foram levantadas ao longo deste percurso, algumas ainda sem resposta definitiva. Assim, novos caminhos de investigação poderão ser trilhados tendo por base as configurações aqui apresentadas.

ABSTRACT

The work described in this PhD Thesis focuses on the post-processing of optical fibers and their enhancement as sensing element. Since the majority of sensors presented are based in Fabry-Perot interferometers, an historical overview of this category of optical fiber sensors is firstly presented. This review considers the works published since the early years, in the beginning of the 1980s, until the middle of 2015.

The incorporation of microcavities at the tip of a single mode fiber was extensively studied, particularly for the measurement of nitrogen and methane gas pressure. These cavities were fabricated using hollow core silica tubes and a hollow core photonic crystal fiber. Following a different approach, the microcavities were incorporated between two sections of single mode fiber. In this case, the low sensitivity to temperature makes these microcavities highly desirable for the measurement of strain at high temperatures.

Competences in post-processing techniques such as the chemical etching and the writing of periodical structures in the fiber core by means of an excimer or a femtosecond laser were also acquired in the course of the PhD programme.

One of the works consisted in the design and manufacturing of a double clad optical fiber. The refractive index of the inner cladding was higher than the one of the outer cladding and the core. Thus, light was guided in the inner cladding instead of propagating in the core. This situation was overcome by applying chemical etching, thus removing the inner cladding. The core, surrounded by air, was then able to guide light. Two different applications were found for this fiber, as a temperature sensor and as an optical refractometer. In the last, the optical phase changes with the liquid refractive index.

Two different types of fiber Bragg gratings were characterized in strain and temperature. Sensing structures obtained through the phase mask technique at the tip of an optical fiber were subjected to chemical etching. In this case, an excimer laser was used. Extremely thin fiber tips were obtained, with an ultra-high sensitivity to strain. The other technique employed to fabricate the fiber Bragg gratings was the point-by-point

femtosecond laser inscription. In this case, the sensing elements are very stable at high temperatures and can be used to measure strain in harsh conditions.

The employment of optical fiber lasers as sensing elements was also considered in this Thesis. Two laser cavities were studied, one based on the ring configuration and the other based on a figure-of-eight configuration. From these works, the quality of the laser emission, namely the signal-to-noise ratio, the reduced full-width at half maximum and the stability should be highlighted. These characteristics allowed the measurement of different physical parameters, such as strain, temperature and torsion.

Lastly, the possibility to use microspheres as sensing elements was considered. Using the electric arc of a fusion splicer, it is possible to create microspheres at the tip of an optical fiber. Furthermore, with this technique it is chains of microspheres can be obtained, constituting Mach-Zehnder-type interferometers which are sensitive to physical parameters like strain and temperature. The preliminary results obtained by introducing silica microspheres in a support structure are also presented. In this case, the sensors were subjected to temperature variations.

All the experimental work was combined with the respective theoretical considerations. Many questions have been raised with the course of this PhD, and there are still some without a definite answer. Thus, new research paths can be followed, having their basis grounded in the configurations here presented.

Table of Contents

LIST OF FIGURES

LIST OF TABLES

LIST OF ACRONYMS

CCD	Charge coupled device
DBR	Distributed Bragg reflector
DCF	Double clad optical fiber
DFB	Distributed feedback
EDFA	Erbium-doped fiber amplifier
FBG	Fiber Bragg grating
FFT	Fast Fourier transform
FIB	Focused ion beam
FP	Fabry-Perot
FSR	Free spectral range
FWHM	Full width at half maximum
GIF	Graded index fiber
HCR-PCF	Hollow-core ring photonic crystal fiber
HF	Hydrofluoric acid
LED	Light emitting diode
LPG	Long period grating
MCVD	Modified chemical vapor deposition
MMF	Multimode fiber
NIM	Nanojet induced mode
OSA	Optical spectrum analyzer
PC	Polarization controller
PCF	Photonic crystal fiber
PM PCF	Polarization maintaining photonic crystal fiber
PZT	Piezoelectric transducer
RI	Refractive index
RIU	Refractive index units
SEM	Scanning electron microscope
SMF	Single mode fiber
SNR	Signal-to-noise ratio
UV	Ultraviolet
VIS	Visible
WDM	Wavelength division multiplexer
WGM	Whispering gallery mode

CHAPTER ONE

Introduction

1.1 Introduction

Optical fiber sensors present several features that make them extremely attractive to be used in several fields, such as electrical engineering, mechanical sciences and engineering, civil engineering, chemical engineering, material science, biology, chemistry, physics, and optics [1]. Living in a highly technological society, the demand for detecting environmental changes, by means of physical, chemical or biological parameters has grown intensely over the last decades. Fiber-based sensors need to be reliable, robust, highly sensitive, and cost-effective to compete with more conventional approaches. The amount of possibilities is immense, depending on the configuration, the measurand and the application for which they are designed.

The post-processing of optical fiber, in the context of the Thesis, corresponds to the physical modifications made to an optical fiber after its production. The ways to achieve it can be by chemical etching, by using a laser to write periodic patterns, such as the fiber Bragg grating, or even to perform micromachining. The fusion splicer can also be used to post-process an optical fiber, by changing its shape. These are the methods explored in this Thesis.

This Chapter gives an overview on the motivation and objectives of this work, followed by a description of the Thesis structure. Finally, the main contributions to the field are presented, as well as the list of publications that resulted from this PhD.

1.2 Motivation and Objectives

The motivation for the work developed in the framework of the PhD programme relied on performing an original study about the development of new structures based on the post-processing of optical fibers and in their enhancement as a sensing element. Besides, this work resulted from the desire to give a contribution to the field, studying and developing different configurations for the measurement of physical parameters. Certainly, another major motivation was to learn new concepts and provide solutions to the different challenges that appeared as the research advanced.

The main objectives relied on:

- the study of diaphragm-free microcavities for gas pressure sensing;

- characterization of sensors based on the post-processing of a purpose-designed double clad optical fiber;

- study of strain measurement in harsh environments, such as in high temperatures;

- development of fiber laser sensors and their respective characterization;

- manufacturing and characterization of interferometric structures based on microspheres.

1.3   Structure of the Thesis

This Thesis is divided in eight Chapters, of which five are relative to experimental work developed in the PhD framework.

Chapter 1 gives an overview of the Thesis structure and its framing within the fiber sensing field. It also contains the main contributions and the list of works published during the PhD.

Chapter 2 provides an historical overview on Fabry-Perot based optical fiber sensors. This review results from the fact most of the sensors described in the Thesis are within this field. The emphasis is done on the cavities configurations, the measurands and the sensitivities achieved so far.

Chapter 3 proposes two different Fabry-Perot cavities for the measurement of gas pressure. The devices are based on a hollow core silica tube and a hollow core ring photonic crystal fiber. The former was the first diaphragm-free Fabry-Perot sensor used in such application reported in the literature. Still in the third Chapter, a prototype for biomedical applications is addressed.

In the Chapter 4, two distinct Fabry-Perot configurations based on the post-processing of a double clad optical fiber are described. The inner cladding, doped with phosphorus, is removed through chemical etching and a tip, protected by the outer

cladding, is formed. The diaphragm free configuration is characterized in high temperature. By introducing a diaphragm in the post-processed structure, an optical-phase refractometer is obtained.

The Chapter 5 is dedicated to the measurement of strain. In a first approach, the control of strain sensitivity is proposed using a hollow core ring photonic crystal fiber Fabry-Perot cavity. Smaller cavities, combined with large lengths over which the strain is applied, result in more sensitive devices. The measurement of strain at high temperatures is studied for the case of a Fabry-Perot cavity and when using a fiber Bragg grating. In both cases the influence of annealing is addressed, in order to achieve better responses to strain.

On the 6th Chapter, the matter of using fiber lasers as active sensors is explored. Besides the characterization of the laser cavities, the sensing elements are subjected to variations of torsion and strain. One of the active sensors, a post-processed fiber Bragg grating, is also studied in a passive configuration, for comparison purposes. An ultra-high sensitivity to strain is achieved with this device.

The sensors described in Chapter 7 are based on microspheres. Two different configurations are explored. One consists of an array of microspheres obtained by post-processing single mode fiber by means of fusion splicing. The second configuration is a Fabry-Perot cavity obtained by placing the soda-lime microspheres inside a hollow core silica tube, which acts as a support structure.

The Chapter 8 presents some lines summarizing the main results achieved during the PhD and describes the opportunities of future work that this investigation has created.

1.4   *Main Contributions*

From the works presented in this Thesis, it is the author opinion that three of them stand out as main contributions to the field. The first was the use of a Fabry-Perot configuration for gas pressure sensing that did not require a diaphragm. Two different hollow core fibers were successfully used in this context, a silica tube and a photonic

crystal fiber. The second contribution was the optical phase refractometer based on a post-processed Fabry-Perot cavity. With such configuration it was possible to detect spectral phase variations with the refractive index. Finally, the new sensing structures based on an array of microspheres that were tested to strain and temperature. The response to strain was dependent on the number of microspheres that constituted the array.

1.5 List of Publications

From the activity developed in the framework of this PhD, a total of 10 articles were published as first author in scientific journals, one of them being an invited paper, and another was a review paper published in the Optical Fiber Technology Journal. Besides, three papers were published as co-author, as a result of collaborations outside the scope of this Thesis. A total of 8 communications in national/international conferences were published during the PhD. The list of works published as first author is presented next.

1.5.1 Scientific Journals

1. M. S. Ferreira, P. Roriz, J. Bierlich, J. Kobelke, K. Wondraczek, C. Aichele, K. Schuster, J. L. Santos, O. Frazão, *Fabry-Perot cavity based on silica tube for strain sensing at high temperatures*, Opt. Express, vol. 23, no. 12, 2015.

2. M. S. Ferreira, J. L. Santos, O. Frazão, *Silica microspheres array sensor*, Opt. Letters, vol. 39, no. 20, 2014.

3. M. S. Ferreira, J. Bierlich, S. Unger, K. Schuster, J. L. Santos, O. Frazão, *Optical phase refractometer based on post-processed interferometric tip sensors*, J. Light. Technol., vol. 32, no. 17, 2014.

4. M. S. Ferreira, J. Bierlich, M. Becker, K. Schuster, J. L. Santos, O. Frazão, *Ultra-high sensitive strain sensor based on post-processed optical fiber Bragg grating*, MDPI Fibers, vol.2, pp.142-149, 2014. **Invited Paper**

5. M. S. Ferreira, P. R. Oliveira, S. Oliveira Silva, J. L. Santos, O. Frazão, *Next generation of Fabry-Perot sensors for high-temperature*, Opt. Fiber Technol., vol.19, 2013. **Review Paper**

6. <u>M. S. Ferreira</u>, J. Bierlich, S. Unger, K. Schuster, J. L. Santos, O. Frazão, *Post-processing of Fabry-Pérot microcavity tip sensor*, IEEE Photonic. Tech. L., vol.25, no.16, pp.1593-1596, 2013.

7. <u>M. S. Ferreira</u>, J. L. Santos, P. Mergo, O. Frazão, *Torsion sensor based on a figure-of-eight cavity fibre laser*, Laser Phys. Lett., vol.10, no. 4, 2013.

8. <u>M. S. Ferreira</u>, J. Bierlich, J. Kobelke, , J. L. Santos, O. Frazão, *Fabry-Pérot cavity based on hollow core ring photonic crystal fiber for pressure sensing*, IEEE Photonic. Tech. L., vol.24, no.23, pp.2122-2124, 2012.

9. <u>M. S. Ferreira</u>, J. Bierlich, J. Kobelke, K. Schuster, J. L. Santos, O. Frazão, *Towards the control of highly sensitive Fabry-Pérot strain sensor based on hollow-core ring photonic crystal fiber*, Opt. Express, vol.20, no.20, pp.21946-21952, 2012.

10. <u>M. S. Ferreira</u>, L. C. Coelho, K. Schuster, J. Kobelke, J. L. Santos, O. Frazão, *Fabry-Pérot cavity based on a diaphragm free hollow core silica tube*, Opt. Letters, vol.36, no.20, pp.4029-4031, 2011.

1.5.2 *Communications in National/International Conferences*

1. <u>M. S. Ferreira</u>, P. Roriz, J. Bierlich, J. Kobelke, K. Wondraczek, C. Aichele, K. Schuster, J. L. Santos, O. Frazão, *Measuring strain at extreme temperatures with a Fabry-Perot optical fiber sensor*, OFS24, Curitiba, Brazil, 2015.

2. <u>M. S. Ferreira</u>, G. Lee, J. L. Santos, K. Sugden, O. Frazão, *Phase-shifted fiber Bragg grating for strain measurement at extreme conditions*, OSA Meeting 2014, Barcelona, Spain, 2014.

3. <u>M. S. Ferreira</u>, J. L. Santos, O. Frazão, *New silica microspheres array sensor*, OFS23, Santander, Spain, 2014.

4. <u>M. S. Ferreira</u>, J. Bierlich, J. Kobelke, K. Wondraczek, C. Aichele, K. Schuster, J. L. Santos, and O. Frazão, *Fabry-Pérot microcavity strains sensor based on advanced silica tube*, AOP2014 - II International Conference on Applications of Optics and Photonics, Aveiro, Portugal, 2014.

5. <u>M. S. Ferreira</u>, J. L. Santos, P. Mergo and O. Frazão, *Figure-of-eight cavity fiber laser based torsion sensor*, RIAO/OPTILAS 2013, Porto, Portugal.

6. <u>M. S. Ferreira</u>, J. Bierlich, S. Unger, K. Schuster, J. L. Santos, O. Frazão, *Post-Processed Fabry-Pérot microcavity tip sensors for temperature measurement*, WSOF-2013 - workshop on specialty optical fibers , Sigtuna, Sweden, 2013.

7. <u>M. S. Ferreira</u>, J. Bierlich, K. Schuster, J. L. Santos, O. Frazão, *Fabry-Pérot microcavity tip temperature sensor based on post-processing*, EWOFS 2013 - 5th European Workshop on Optical Fibre Sensors, Kraków, Poland, 2013.

8. <u>M. S. Ferreira</u>, K. Schuster, J. Kobelke, J. L. Santos, O. Frazão, *Fabry-Pérot cavity based on large hollow core photonic crystal fiber for nitrogen pressure measurements*, SEON 2012 – VIII Symposium on Enabling Optical Networks and Sensors, Aveiro, Portugal, 2012.

CHAPTER TWO

Historical Overview of Fiber Sensors Based on Fabry-Perot Interferometry

2.1 Introduction

Fiber optic sensors based on interferometry have been widely explored over the last five decades. From the most basic configurations, the Mach-Zehnder, the Michelson, the Sagnac and the low-finesse Fabry-Perot (FP) interferometers stand out [2]. Regarding the FP interferometer, it is usually composed by two parallel reflecting surfaces with a small separation between them. Light reaching the cavity with near normal incidence, will suffer several internal reflections at the interfaces, resulting in a multiple beam interferometer. This translates in a higher interaction of the measurand with the guided light, and consequently, in a higher sensitivity. Besides, this interferometer offers unique advantages, such as the compactness, reliability and the fact that it does not require the presence of an extra fiber to serve as a reference arm, since the interference occurs within a single fiber [3].

In this Chapter, the most common fiber optic configurations based on Fabry-Perot interferometry are described, followed by an historical overview of the development of these structures since the first papers were published, in the 1980s.

2.2 Fabry-Perot Based Sensors: the Basic Characteristics

Since the first fiber optic FP-based sensor proof of concept, that took place in the early 1980s, there has been a great evolution in this field. In the 1980s two different categories of optical fiber sensors based on FP interferometry arose, the extrinsic and the intrinsic configurations. In the former, the cavity, which acts as the sensing element, is located outside the fiber and the two mirrors required to form the cavity can be two fiber tips placed close enough to ensure interference (Fig. 2.1 (a)) or one fiber tip and a reflective element (Fig. 2.1 (b)). In order to keep the structure stable, it can be placed inside a capillary tube, as represented in the example in Fig. 2.1 (a).

When the FP cavity is contained within the optical fiber, the configuration is considered to be intrinsic. One way to produce this type of configuration can be by

splicing a hollow core fiber between two single mode fibers, as represented in Fig. 2.1 (c), or by creating two in-line partial mirrors, as in Fig. 2.1 (d).
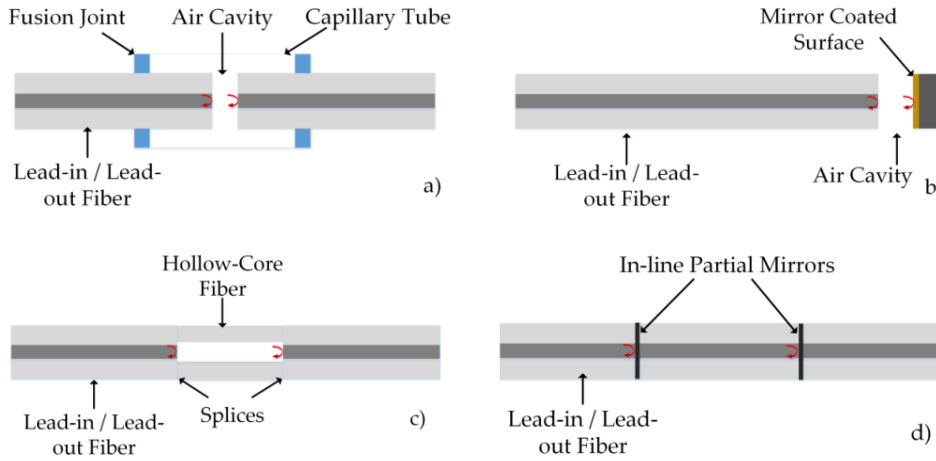
Figure 2.1 – Schematic examples of fiber optic FP interferometers: a) and b) extrinsic configurations, c) and d) intrinsic configurations.

From 1990 to 2005, the focus of research was mainly on the signal acquisition systems and on the interrogation techniques. In that period, a major evolution of extrinsic FP-based sensors occurred. However, with the arising of sensors based on fiber Bragg gratings (FBGs) in 1990 [4] and the photonic crystal fibers (PCFs) in 1996 [5], the number of papers about intrinsic FP sensors slowly began to rise.

From the year 2005 until 2015, the majority of works are on intrinsic FP interferometers and the focus of research turned into the cavity designs. New configurations based on the fusion splicing of special optical fibers [6], the chemical etching [7], femtosecond laser micromachining [8], excimer laser micromachining [9] and, more recently, on the focused ion beam (FIB) micromachining [10] have been investigated. These new sensor devices, besides being easy to produce and reproducible, are reliable and have low dimensions, which can be of the order of a few micrometers.

In order to provide an overview of the evolution in optical fiber FP cavity sensors, a thorough description is performed next. The focus was both on the cavities design evolution that occurred throughout the years and on the sensing measurands. A Table is presented at the end of this overview, with some of the most important configurations reported from 2009 to 2015. Besides the configuration, the measurands and respective sensitivities are considered.

2.3   The First Fabry-Perot Interferometer

The Fabry-Perot (FP) interferometer was firstly published in 1897 by Charles Fabry and Alfred Perot, in the *Annales de Chimie et de Physique* [11]. Figure 2.2 presents the first page of one of the most important papers published by the two researchers, entitled *Sur les franges des lames minces argentées et leur application à la measure de petites épaisseurs d'air.*
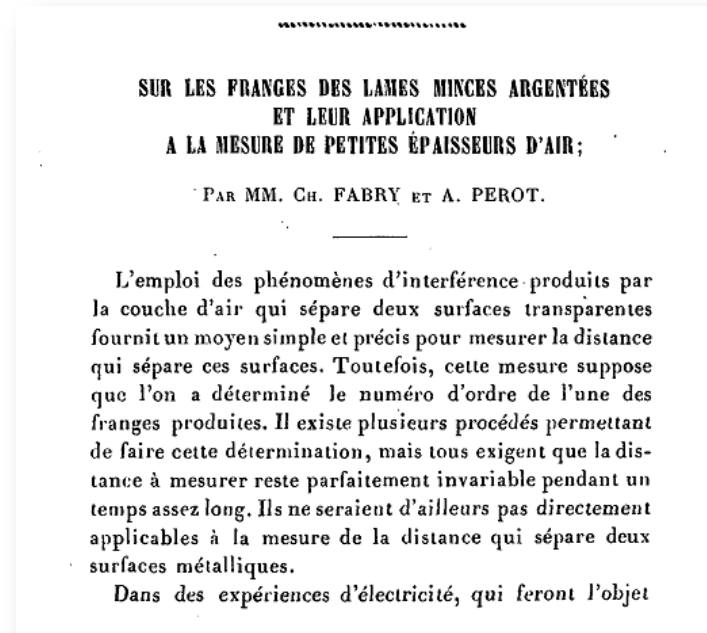
Figure 2.2 – First page of the paper published by Fabry and Perot in 1897 [11].

The simple configuration, depicted in Fig. 2.3, set the basis of one of the interferometers most widely used currently in optics and photonics. Light from the electric arc optical source (*A*) propagates through a system of lenses (*L*, L') and will suffer multiple interferences at the silvered glass (*B*). At the third lens (*L''*), the transmitted light will be focused and the interference pattern will appear on the display *E*.
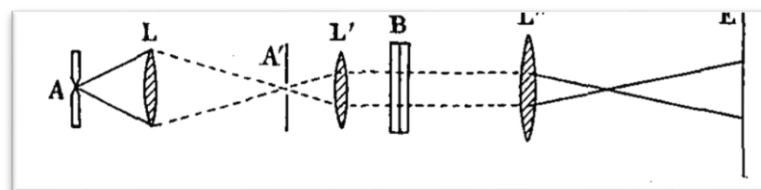
Figure 2.3 – Fabry-Perot interferometer experimental setup. *A* stands for the optical source (electric arc in the original), *L*, *L'* and *L''* are lenses, *A'* is a slit, *E* is the display and *B* corresponds to the silvered glass [11].

2.4 Historical Perspective on Fabry-Perot based Optical Fiber Sensors

In 1979, a double-cavity single-fiber configuration was proposed as a hydrophone element by Cielo [12]. The reference cavity was situated on the surface, close to the electronics apparatus, whereas the sensing element was placed under water. Each cavity was formed by bounding the fiber ends with a reflector and coiling it around a cylinder, as can be seen of Fig. 2.4 (a), where the proposed configuration is depicted. The spectral response of a single cavity is shown in Fig. 2.4 (b).
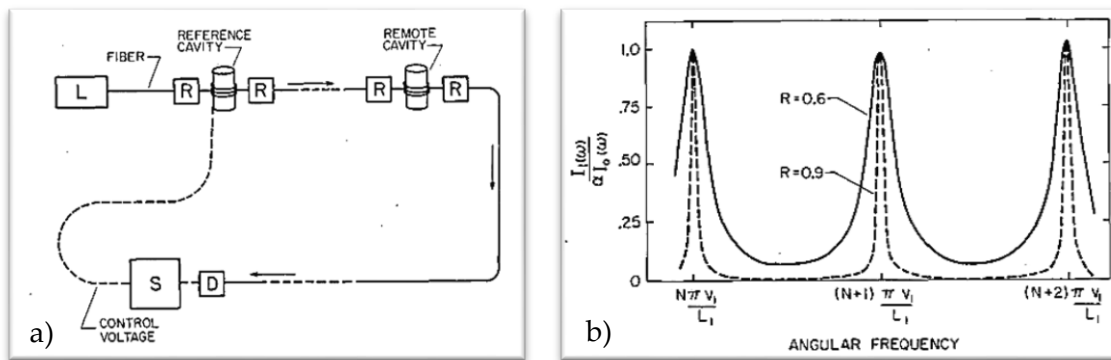
Figure 2.4 – (a) Configuration proposed in 1979 by Cielo [12]. L is the light source coupled to the fiber, R corresponds to the reflectors, D is the photodetector, and S stands for the servo-control electronics. (b) Spectral response of a single cavity [12].

In 1981, Yoshino *et al.* presented a FP-based fiber temperature sensor on the Third International Conference on Integrated Optics and Optical Fiber Communications [13]. In the same year, Petuchowski *et al.* proposed a high-finesse and highly sensitive to phase-shifts fiber optic FP interferometer [14]. A single mode fiber (SMF) with the ends coated with dielectric partial mirrors constituted the FP cavity. In the same year, Franzen *et al.* used a long section of a fiber FP to perform metrology of single frequency laser sources [15]. They took advantage from the fact that the free spectral range of a FP cavity is inversely proportional to the cavity length and that using a cavity with high finesse there is an increase in the frequency resolution of the sensor.

In 1982, Yoshino *et al.* studied the basic properties of a fiber optic FP interferometer, namely the finesse, polarization and thermal responses. Besides, the devices were also characterized in temperature, mechanical vibration, acoustic wave detection, *ac* voltage, as well as *ac* and *dc* magnetic fields [16]. On the same year, Otsuka performed a

theoretical study on the temporal effects of a light-source on a fiber optic FP interferometer [17].

The use of uncoated cleaved fiber ends as FP cavity mirrors was proposed in 1983 by Kersey *et al.* [3]. The sensor was used in an accelerometer configuration, where it exhibited high sensitivity and good linearity. In the same year, Kist *et al.* proposed the use of FP resonators as temperature-tuned optical spectrum analyzers for the first time [18].

In 1984, Leilabady *et al.* used a SMF in a FP configuration to measure the flow velocity. The operating principle relied on the fiber oscillations induced by the vortex shedding. In this case, the FP cavity mirrors were formed by one normally cleaved input and one silvered end. The readings were done in reflection and a linear response was attained [19].

In 1985, a remote displacement sensor based on an extrinsic FP interferometer was proposed [20]. Using a two interferometer system, the sensing cavity modulated the spectrum of the light emitting diode (LED) as a function of the cavity length. Even though there was a breakthrough with this work, where they used a broadband optical source and a novel signal processing scheme, the optical fiber was only used to launch light and collect the interference pattern that resulted from the bulk FP cavity. Following this sensing concept, a couple of works have been published later to measure pressure variations [21, 22].

In 1986, the precise measurement of the optical length using a FP interferometer was proposed [23]. The two mirrors of the FP cavity were formed by the polished, uncoated ends of a SMF section. The sensor was subjected to temperature measurements, where it exhibited high sensitivity.

In February 1988, Tseng *et al.* proposed a temperature sensor that was able to discern temperature rise from temperature drop [24]. The FP cavity mirrors were created by the deposition of aluminum mirrors on the fiber ends. In the same month, a major breakthrough occurred in the field. The ability to produce the dielectric mirrors inside the optical fiber, by means of splicing, was achieved by Lee *et al.* [25]. The configuration,

shown in Fig. 2.5, allowed the multiplexing of several sensors. The devices were tested to temperature in a range between 20 °C and 600 °C. This work opened up a new category of FP based sensors, the intrinsic FP cavities. In a different approach, the use of a short coherence optical source (LED) to illuminate a multiplexed system with two FP interferometers was proposed by Farahi *et al.* in March 1988 [26]. Even though the LED had had already been used as an optical source in a FP sensor cavity [20], this was the first time it was employed in a fiber optic extrinsic FP sensing system. The sensor was tested to temperature. Gerges *et al.* proposed a miniature hemispherical air cavity FP interferometer [2]. One of the mirrors was formed by the end face of the optical fiber, whereas the other mirror was composed by hemispherical reflecting surface. The sensor was subjected to a small range of temperature variations (40 – 55 °C), where a sensitivity of 2.155 rad/K was attained. Finally, in that same year and using a configuration similar to the one previously described [25], Lee *et al.* proposed a temperature sensor that was subjected to a temperature variation from -200 °C to 1050 °C, the widest range that had been reported until that time [27]. Besides, the FP cavity length was very small, of only 1.5 mm. The sensor could be thus considered a point sensor in several applications.
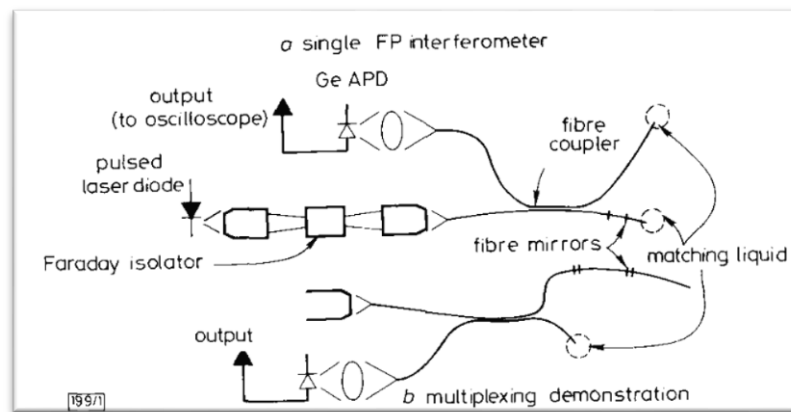
Figure 2.5 – Experimental setup for the evaluation of multiplexed FP sensors [25].

In 1989, Kersey *et al.* proposed a different way to produce the mirrors of in-line FP sensors. Fiber ring reflectors were used as low-reflectivity elements [28]. The cross-talk in an array of four sensors was investigated. In the same year, the application of a FP cavity shaped as a single-turn helix was proposed as a magneto-optic current sensor [29]. Lee *et al.* embedded an intrinsic FP sensor in a graphite-epoxy composite material for the first time [30]. The sensor was tested to temperature variations from 20 °C to 200 °C.

In 1990, a short length all-fiber FP cavity was tested to strain [31]. The sensors were adhered to the surface of a cantilever beam. Farahi *et al.* demonstrated an interferometric technique that allowed the simultaneous measurement of strain and temperature in a cavity formed in highly birefringent fiber [32]. This was the first work regarding the simultaneous discrimination of two physical parameters using a FP cavity sensor. In the same year, Alcoz *et al.* proposed an ultrasound fiber sensor embedded in plastic and graphite composite materials [33]. The FP cavity was formed between two dielectric internal mirrors. Each mirror was fabricated by splicing a fiber coated with a TiO_2 film at one end to an uncoated fiber.

In 1991, Lee *et al.* proposed an interferometric fiber optic temperature sensor illuminated with a LED [34]. Two FP intrinsic interferometers with similar cavity lengths were disposed in series, where one acted as sensor whilst the other was used as a reference. Still in 1991, a quadrature phase-shifted, extrinsic FP sensor was proposed to perform dynamic strain measurements [35].

In 1992, the same group proposed an extrinsic FP sensor for the measurement of strain and crack opening displacement in ceramic materials [36]. The device operated as strain sensor in a temperature between -200 °C of 900 °C. Santos *et al.* compared both theoretically and experimentally the transfer function of low-finesse extrinsic FP sensors with the typical two-wave interferometer [37]. Also in 1992, Wang *et al.* proposed a sapphire optical fiber intrinsic FP sensor for the measurement of high temperature [38]. The FP cavity was formed by splicing a section of sapphire multimode optical fiber to silica SMF.

In 1993, an extrinsic FP strain sensor based on white-light interferometry was proposed by Belleville *et al.* [39]. In the same year, a FP cavity was used as a wavelength filter for detecting the wavelength shift of a FBG [40]. Finally, Sirkis *et al.* developed a new FP-based configuration to be used as strain sensor [41]. A hollow core fiber was manufactured with the same outer diameter as the SMF. A short section of this fiber was spliced between two sections of SMF, forming an in-line fiber etalon, as can be seen in Fig. 2.6.
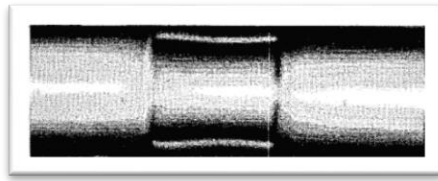
Figure 2.6 - Photograph of the 112 μm long in-line fiber etalon proposed by Sirkis *et al.* in 1993 [41].

In 1994, the design of a FP pressure sensor was proposed for internal combustion engines [42]. Also in that year, a microlaser based on Er:Yb phosphate-glass fiber within an extrinsic FP cavity was reported [43]. The cavity was only 100 μm long and presented a continuous wavelength tuning range over 4.52 nm. By using a three-mirror cavity configuration, single mode operation was achieved.

In 1995, a temperature sensor array was described using low-coherence reflectometry [44]. The sensor array was composed by several standard FC-PC connectors. Dorighi *et al.* proposed a new configuration to stabilize an intrinsic fiber optic FP interferometer [45]. The sensor was embedded in a solid material in order to detect ultrasound. In the same year, a new digital signal processing scheme was proposed for the measurement of pressure in an internal combustion engine [46].

In 1996, a four-wavelength technique was employed to interrogate a low-finesse fiber optic extrinsic FP interferometer [47]. The device was characterized in vibration and temperature. The detection of ultrasound using a polymer thin film as a low finesse FP was proposed by Beard *et al.* [48]. The ultrasound propagated in a water filled cavity, which was located between the end face of a multimode fiber (MMF) and the transparent polymeric film. In the same year, an intrinsic FP pressure sensor was suggested by Kao *et al.* [49]. In this configuration, the motion of an epoxy-based diaphragm produced strain in the FP sensor. Still in 1996, a load sensor based on an extrinsic FP interferometer was also suggested [50].

In 1997, a low-finesse FP sensor was embedded both in water and epoxy to detect ultrasound [51]. Chang *et al.* proposed the employment of a low-finesse readout FP interferometer to scan a high-finesse FP sensor cavity length [52]. In this case, the sensor was subjected to static strain measurements. In the same year, an extrinsic FP interferometer was developed to measure magnetic fields [53]. The cavity was formed

between the end face of a SMF section and a Metglas ($Fe_{77.5}B_{15}Si_{7.5}$) wire-based magnetostrictive transducer.

In 1998, a high precision displacement sensor was proposed by Wang *et al.* [54]. The extrinsic FP cavity was formed between the SMF end and the front surface of a reflective film, which was glued to a piezoelectric transducer (PZT). The displacement resolution of the sensor was of 0.005 nm. An intrinsic FP sensor was used to measure the liquid flow velocity in a pipe [55]. Later that year, an extrinsic FP interferometer was employed to determine the residual stresses in fiber-reinforced composite materials [56].

In 1999, Du *et al.* presented for the first time a FP cavity whose mirrors were FBGs, with the configuration similar to the one presented Fig. 2.7 [57]. The sensor was glued to an aluminum tube and tested to strain and temperature, where sensitivities of 1.19 pm/με and 14.35 pm/°C were respectively obtained. Also in that year, a three-wave extrinsic FP interferometer was developed to measure strain and vibration, using digital phase demodulation [58]. Arregui *et al.* proposed a humidity sensor based on a nano-FP cavity [59]. The structure was formed by ionic self-assembly method.
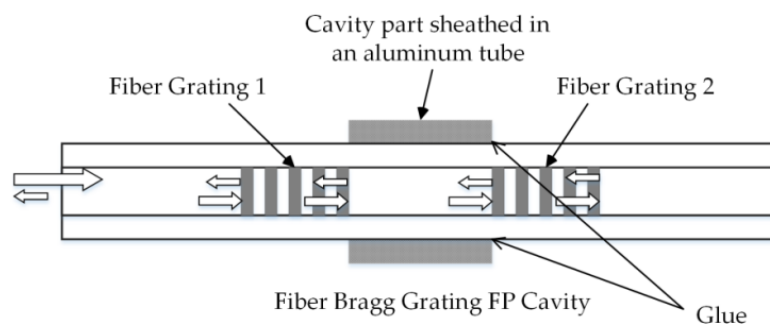
Figure 2.7 – Structure of the fiber Bragg grating FP cavity proposed by Du *et al.* (adapted from [57]).

In 2000, a new frequency multiplexing method was developed for addressing low finesse FP sensors using a white light source and a charge-coupled device (CCD) based monochromator [60]. Three extrinsic FP sensors were multiplexed and tested to strain and displacement, with accuracy better than 0.01 μm. In the same year, Katsumata *et al.* reported a FP pressure sensor with a diameter of 125 μm for catheter [61]. The silicon-based sensing element was fabricated through micromachining and attached to the end of an optical fiber.

In 2001, a new extrinsic FP configuration was proposed by Jiang *et al.* [62]. The end section of an optical fiber was polished at 45° and placed close to a polymer film on a steel plate. The sensor was tested to strain and temperature. In the same year, a new concept of FP interferometer-based temperature sensors was presented by Tsai *et al.* [63]. The structure, depicted in Fig. 2.8, was obtained by fusion splicing two fibers with different core diameters. One of the reflective mirrors was produced at the interface between the fibers, whilst the other was obtained at the fiber/air interface. Finally, Dahlem *et al.* proposed the use of FBGs to interrogate low-finesse extrinsic FP cavities, when subjected to displacement and temperature variations [64].
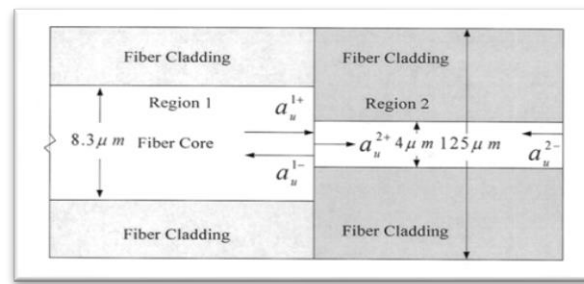
Figure 2.8 – Structure of the FP temperature sensor proposed by Tsai *et al.* [63].

In 2002, Chen *et al.* proposed the use of a white-light interferometry system based on a scanned Michelson interferometer to interrogate intrinsic FP temperature sensors [65]. The rather complex scheme yielded a resolution of 0.013 °C.

In 2003, a pressure sensor based on an extrinsic FP interferometer was reported [66]. The cavity was formed between a copper diaphragm and the end face of a SMF. The sensor was embedded in epoxy and applied in the aerodynamic field. The detection of weak acoustic waves was a subject of study by Yu *et al.* [67]. Using an extrinsic FP configuration, these sensors became an alternative to conventional acoustic sensors for the detection of partial discharges in power transformers.

In 2004, the use of extrinsic FP interferometers to measure nano-displacement, with a minimum displacement of 10 nm was reported [68]. Other parameters were also analyzed in similar configurations, such as pressure and temperature [69, 70]. In the same year, Shen *et al.* fabricated an intrinsic FP cavity by exposing the photosensitive fiber to UV radiation [71]. Using a metallic mask, they locally produced the Fresnel

reflectors, using the point-by-point technique. The device was subjected to temperature, strain and pressure variations.

In 2005, Xiao *et al.* developed an extrinsic FP device for gas sensing [72]. The cavity, formed between two ferrules, was able to measure the N_2 refractive index variation with a resolution greater than 10^{-5}. A different extrinsic FP cavity was proposed by Xu *et al.*, to measure pressure and acoustic waves [73]. On the same year, Cibula *et al.* developed a new type of miniature intrinsic FP sensors [7, 74]. A hollow structure with ~125 μm was obtained by wet chemical etching a MMF. In a first approach, a thin polymer diaphragm was positioned inside the hollow structure [74]. Later that year, the same group developed an all-silica FP cavity [7]. Both devices were tested in pressure of liquids. The combination of different structures was also a matter of study in 2005, being further developed since then. For example, Huang *et al.* proposed the splicing of a MMF section between two sections of SMF [6]. The sensor was tested to temperatures up to 600 °C and to strain up to 400 με. The simultaneous measurement of the refractive index of liquids and of temperature was proposed by Kim *et al.* [75]. In this case, a long period grating (LPG) was spliced in series to an intrinsic FP cavity whose mirrors were created by chemically etching a SMF.

In 2006, Zhu *et al.* proposed a N_2 pressure sensor for high temperature [76]. The sensor was obtained by chemically etching a MMF and using a fused silica diaphragm. Wang *et al.* also reported a pressure and temperature sensor based on a SMF/hollow fiber/SMF diaphragm structure [77]. In this case, pressure measurements were done with the sensor submerged in water and the device was subjected to temperatures below 600 °C. Watson *et al.* fabricated the FP cavities using ArF excimer laser ablation [9]. An aluminized membrane was used as diaphragm and dynamic N_2 pressure measurements were performed. Dynamic strain/bend measurements were done by Cranch *et al.*, using a multicore fiber FP with FBGs as mirrors [78]. Other strain sensors have been proposed, whose cavities were created by etching the fibers [79, 80].

In 2007, the etching of optical fibers to produce FP cavities attracted a lot of attention. Machavaram *et al.* reported the etching of two SMF sections that formed the intrinsic FP

interferometer when spliced together [81]. The sensors were tested in strain and a cavity length variation of 0.5 nm/με was attained. On the other hand, Cibula *et al.* produced a strain sensor by splicing an etched MMF section between two sections of SMF [82]. Zhang *et al.* proposed a microgap cavity formed by wet etching and splicing SMFs [83]. The multiplexing of two FP cavities enabled the temperature compensation of a biosensor. The micromachining of cavities in PCFs using a 157 nm excimer laser [84] or femtosecond laser [8] for strain and temperature measurement were also reported. In both cases the devices presented low sensitivity to temperature but high sensitivity to strain. In a different approach, Rao *et al.* presented, for the first time, a FP cavity based on a hollow-core PCF section spliced between two SMFs, whose configuration is shown in Fig. 2.9 [85]. In order to increase the reflectivity, a Ti_2O_3 film was coated on the lead-out SMF before splicing. The cavity length was a couple millimeters long and it was tested to strain. The multiplexing of up to fifty FP cavity sensors was demonstrated by Wang *et al.* [86]. Two FBGs constituted the FP cavity interfaces and the devices were tested to strain and temperature.
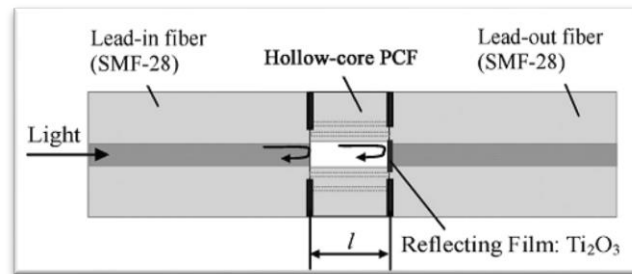
Figure 2.9 – Configuration of an in-line hollow-core PCF etalon, proposed by Rao *et al.* [85].

In 2008, the post-processing of optical fibers by means of laser micromachining continued to be developed [87-89]. On the one hand, the micromachining exposes the fiber core region and the FP cavities produced in this way are very sensitive to the external medium. On the other hand, the sensors are temperature independent. A different structure was proposed by Rao *et al.* for refractive index measurements [90]. In this case, the FP cavity was formed by fusion splicing a section of endlessly single mode PCF between two sections of SMF. The use of different fiber geometries spliced in series with SMF and/or PCF enabled high temperature [91] as well as strain [92] sensing. An humidity sensor was presented by Corres *et al.* [93]. The device consisted of a tip of SMF

coated with a SiO$_2$ super hydrophilic nanofilm. An extrinsic FP temperature and strain sensors was developed by Jiang *et al.*, by curing epoxy droplets at the end of SMF sections in order to produce micro-lenses [94].

In 2009, Liu *et al.* proposed a gas sensor based on a silver layer and a vapor sensitive polymer layer that were sequentially deposited at the cleaved end tip of a SMF [95]. The device was able to detect methanol vapor with a sensitivity of 3.5 pm/ppm. A pressure sensor was described by Cibula *et al.*, whose cavity was obtained by fusion splicing a SMF to an etched Ge-doped fiber [96]. Morris *et al.* presented a temperature and acoustic pressure sensor, constituted by a polymer deposited at the end tip of an optical fiber [97]. Higher fringe visibility was attained through the deposition of two gold mirrors at the polymer interfaces. Two different configurations were proposed to measure refractive index variations. The first configuration was a microcavity formed near the fiber end tip by 157 nm laser micromachining [98]. Two thin films were deposited in the cavity mirrors and a microchannel was created on the fiber end, enabling the interaction between the external medium and the microcavity. A sensitivity of 1130 nm/RIU was attained with this thermal-insensitive device. The second configuration was a suspended-core fiber spliced between two sections of SMF [99], whose response was characterized in the spatial frequency domain. The same authors proposed the splice in series of a suspended core fiber (with three or four holes) and a hollow-core PCF to SMF [100]. A novel strain and temperature sensor was fabricated and characterized by Villatoro *et al.* [101]. An air bubble was created by fusion splicing a PCF and a SMF, as can be seen in Fig. 2.10. Strain and temperature sensitivities of 2.7 pm/με and 0.95 pm/°C were respectively achieved. In the same year, Gong *et al.* proposed a different FP based interferometer [102]. The device, obtained by splicing an etched Er-doped fiber with SMF, translated in a sensor with low thermal sensitivity (~0.65 pm/°C) but with good response to strain, of 3.15 pm/με . A hollow-core photonic bandgap fiber spliced between two sections of SMF was reported by Rao *et al.* for measurement of temperature below 600 °C [103].
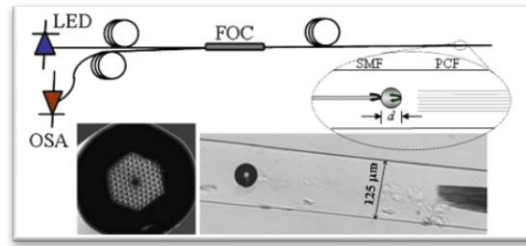
Figure 2.10 – Diagram of the configuration proposed by Villatoro *et al.* [101]. FOC stands for fiber optic circulator, LED is the light emitting diode and OSA corresponds to the optical spectrum analyzer.

In 2010, several works were related to the measurement of refractive index and temperature. The use of a dual cavity based on a small section of hollow core fiber between a MMF and a SMF [104], an etched graded index fiber (GIF) spliced to SMF [105, 106], or even a hybrid Michelson/FP structure were proposed to measure these parameters simultaneously [107]. Kou *et al.* reported for the first time the direct fabrication of a FP cavity in a fiber taper [10, 108]. The device, shown in Fig. 2.11, was created using a focused ion beam (FIB) and subjected to liquid refractive index [108] and high temperature [10] variations. Still in that year, two other configurations were proposed to measure refractive index. On the one hand, Deng *et al.* were able to measure the N_2 refractive index using a SMF/hollow core fiber/PCF structure, with sensitivity of 1639 nm/RIU [109]. On the other hand, by coating a SMF tip with an epoxy-based polymer, Zhao *et al.* were able to measure the water refractive index variation, with a sensitivity of ~205 dB/RIU [110]. A temperature sensor based on a short section of all-silica PCF spliced to SMF was demonstrated [111]. Also to measure temperature, a dual wavelength Raman fiber laser was employed to interrogate a suspended core fiber based cavity [112]. An accelerometer based on a hollow-core PCF cantilever structure was presented by Ke *et al.* [113]. Finally, a pressure sensor based on an etched optical fiber with a silica diaphragm was also proposed [114].
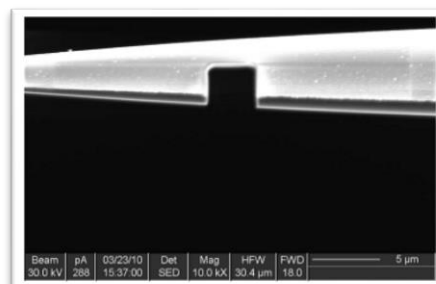
Figure 2.11 – Scanning electron microscope image of the FP cavity created using FIB [108] .

In 2011, a temperature sensor based on a hollow core fiber spliced to a SMF with lateral offset was proposed [115]. The post-processing of optical fibers using FIB for temperature and water salinity sensing [116] or chemical etching for strain [117] and refractive index [118] measurements were developed. In the last work, the cladding was removed from a SMF and the core became in direct contact with the external medium. The cavity was formed splicing the etched fiber in between two fibers containing in-fiber mirrors. A refractometer was proposed by Zhou *et al.* where the FP cavities were formed by UV-written FBGs and microchannels produced by femtosecond laser and chemical etching [119]. An extrinsic FP interferometer was proposed to measure displacement over a dynamic range of 3 mm [120]. A strain sensor that could operate at high temperatures was reported by Deng *et al.* [121]. In this case, an air-bubble cavity was produced by fusion splicing a multimode PCF to SMF. Ferreira *et al.* proposed a FP cavity based on a hollow core silica tube for gas pressure measurements [122]. With this configuration, presented in Fig. 2.12, no diaphragm was used and a sensitivity of 2.61 nm/MPa was attained.
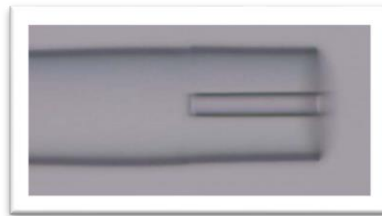
Figure 2.12 – Microscope photograph of the first diaphragm-free FP cavity for gas pressure sensing [122].

In 2012, Gouveia *et al.* proposed the simultaneous measurement of liquid refractive index and temperature by using a FBG written in a PANDA fiber [123]. A FP cavity was formed between the FBG and the PANDA fiber cleaved end. On the other hand, Wang *et al.* proposed an ellipsoidal cavity formed by splicing a SMF and a PCF [124]. In this case, the external RI was measured through the fast Fourier transform (FFT) analysis, and the temperature was measured tracking the wavelength shift. A different gas refractometer was proposed by Silva *et al.*, by splicing a fiber with an outer diameter of 50 μm with a strong misalignment between two SMFs [125]. Also in that year, other configurations were proposed to measure refractive index. The FP cavities were made by femtosecond laser micromachining [126], by splicing a SMF with a large lateral offset between two

SMFs [127], by splicing an etched GIF with a SMF [128], or even using a hollow core fiber ended with a hollow core silica sphere tip [129]. In the same year, several configurations were developed to measure strain. For example, spheroidal cavities were formed by splicing a PCF and a SMF [130, 131], or by splicing one section of cleaved flat tip SMF and an arc fusion induced hemispherical tip [132]. The splice of a hollow-core ring PCF fiber between two SMFs was also proposed to measure strain and temperature [133]. Tafulo *et al.* proposed the use of FP cavities based on chemical etching of multimode GIFs to produce sensors for high temperature and strain [134, 135]. Zhang *et al.* proposed a FP cavity based on a polarization maintaining PCF to measure temperatures up to 600 °C [136]. A FP device based on an endlessly single mode PCF was also characterized in extreme temperatures, as high as 1100 °C [137]. In order to perform simultaneous measurement of gas pressure and temperature, Pevec *et al.* proposed two low finesse FP resonators created at the tip of an optical fiber [138]. Ferreira *et al.* used a short section of hollow core ring PCF spliced to a SMF to measure methane pressure variations. Two different applications were also considered in 2012. Using an extrinsic FP interferometer, Lai *et al.* proposed a liquid level and specific gravity sensor [139]. Wang *et al.* measured high intensity focused ultrasound fields by using a silica capillary tube spliced between two sections of SMF [140].

In 2013, the main focus of research was on refractive index FP sensors. For instance, by splicing a simplified hollow-core PCF between two SMFs and drilling microchannels with femtosecond laser, Wang *et al.* obtained a sensor with a sensitivity of ~851.3 nm/RIU that was insensitive to temperature [141]. On the other hand, Sun *et al.* proposed a hybrid FP/Michelson interferometer to simultaneously measure refractive index and temperature [142]. Zhang *et al.* fabricated a cavity by taper-drawing a microfiber at the center of a uniform FBG [143]. A FP sensor based on an ultra-thin film of gold embedded in a SMF end face was investigated for refractive index and high temperature measurements [144]. A couple of structures were also developed for temperature sensing, such as cavities based on the post-processing of a double cladding optical fiber [145] and extrinsic FP interferometers [146]. Finally, the splicing of different structures like the hollow-core microstructured fiber in between two SMFs [147], or an etched MMF

between a SMF and a silicon dioxide diaphragm were proposed for pressure sensing [148].

In 2014, the fabrication of air cavities, or micro-bubbles, inside the optical fiber was subject of extensive study [149-151]. These FP cavities were mainly applied in strain and temperature sensing, and astonishing sensitivities were achieved, as can be seen in Table 2.1. The post-processing of optical fibers, by means of chemical etching [152, 153], FIB micromachining [154], or tapering [155], also translated in new sensing FP configurations with good responses. A high speed interrogation scheme was developed for high temperature measurements [156]. A miniature configuration based on a double-core PCF spliced to SMF was subjected to temperatures below 900 °C [157]. Liao *et al.* presented a sub-micron silica diaphragm based fiber tip FP interferometer that presented a response of ~1036 pm/MPa to gas pressure changes [158]. Also in this year, a novel type of sensor based on an extrinsic FP interferometer and a magnetic fluid was reported. It was observed that the refractive index of the magnetic fluid changes with the increase of the magnetic field, enabling a magnetic field sensitivity of 0.0431 nm/Gs.

Until June 2015, several works were published concerning FP-based fiber sensors. Eom *et al.* proposed an extrinsic FP configuration constituted by a lensed fiber and a polymeric diaphragm [159]. The sensor was tested in low pressure range and was proposed for the medical field. Lee *et al.* reported on the measurement of the thermo-optic coefficient of liquids using a structure composed by two hollow core fibers with different diameters [160]. Besides, Sun *et al.* designed a FP interferometer for the simultaneous measurement of pressure and temperature [161]. The sensor head was based on a polymer capped on the end face of a SMF. The simultaneous measurement of refractive index and temperature was studied by Wu *et al.*, by using a cavity based on a multimode PCF with collapsed ends to create thin films [162]. A FP cavity based on the deposition of a magnetostrictive material in the fiber, between two FBGs, was proposed as a magnetic sensor by Li *et al.* [163]. The measurement of dynamic displacement was addressed by Pullteap *et al.* [164]. An extrinsic FP interferometer was used, where a birefringent element was introduced between the fiber and the vibration target. Also in 2015, a strain sensor based on a rectangular air bubble was proposed by Liu *et al.* [165].

The bubble was created by splicing two sections of SMF and tapering the splicing joint. For an air bubble of ~61 μm, a sensitivity to strain of 43 pm/με was achieved. Chen *et al*. proposed an ultraweak intrinsic FP cavity array for distributed temperature sensing [166]. An high-resolution and fast-response temperature sensor based on a silicon FP cavity was also described [167]. A FP temperature sensor based on differential pressure resulting from thermal expansion of sealed air was developed by Liu *et al*. [168]. A salinity sensor was obtained by using a FP cavity with a polyimide diaphragm. With such configuration, a maximum sensitivity of 0.45 nm/(mol/L) was achieved [169].

The main characteristics of the different intrinsic FP sensors reported since 2009 until 2015 are gathered in Table 2.1. Multiple configurations have been explored in these years. The reduced dimensions of the cavities stand out, since most of them are in the order of a few hundred micrometers. Notice also the different measurands and the ranges over which the sensors were tested. The most popular ones seem to be strain and temperature, and the highest measurement range achieved was of 5000 με for the former and ~950 °C for the last. Depending on the configuration, it is possible to obtain sensor with very good sensitivity to temperature (for example, -6.71 nm/°C [149]) or with extremely low sensitivity to this parameter, thus enabling the measurement of different parameters with low cross-sensitivity (as in the case of [142], for example, where the sensitivity to temperature is only 0.27 pm/°C). The wide variety of possible configurations and the high versatility of these kinds of structures are an indication that there is still room for research and development in this field, even though the first steps were taken 36 years ago.

Table 2.1 - Different fiber optic intrinsic FP sensors, with the respective characteristics, from 2009-2015.

Year	Configuration	Length (μm)	Measurand	Range	Sensitivity	Ref.
2009	Air bubble between PCF and SMF	58	Strain	0-5000 με	2.7 pm/με	[101]
		22	Temp.	23-500 °C	0.95 pm/°C	
2009	SMF + 3 holes suspended core + hollow core PCF	~840	Strain	0-1000 με	1.32 pm/με	[100]
			Temp.	23-90 °C	7.65 pm/°C	
	SMF + 4 holes suspended core + hollow core PCF	~1000	Strain	0-1000 με	1.16 pm/με	
			Temp.	23-90 °C	8.89 pm/°C	
2009	SMF + etched Er-doped fiber	27	Strain	0-800 με	~3.15 pm/με	[102]
			Temp.	23-80 °C	~0.65 pm/°C	

2009	157 nm laser micromachining cavity + microchannel + mirrors coated with thin film	25	Liquid RI Temp.	1.33-1.405 RIU 0-70 °C	~1130 nm/RIU ~0.8 pm/°C	[98]
2010	SMF + etched GIF (hybrid structure)	505	Liquid RI Temp.	1.32-1.45 RIU 15-90 °C	~160 dB/RIU ~10.4 pm/°C	[106]
2010	SMF + etched GIF (hybrid structure)	25 515	Liquid RI Temp.	1.32-1.47 RIU 15-90 °C	~45.05 dB/RIU ~11.5 pm/°C	[105]
2010	Fiber taper + FIB micromachining	4.4	Temp.	19-520 °C	~20 pm/°C	[10]
2010	Fiber taper + FIB micromachining	3.5	Liquid RI	1.355-1.375 RIU	110 nm/RIU	[108]
2010	SMF + microstructured fiber with dual core (hybrid structure)	~11500	Strain Temp.	0-1000 µε 0-60 °C	0.89 pm/µε 14.22 pm/°C	[107]
2010	SMF tip coated with polymer thin film	29.9	Liquid RI	1.314-1.365 RIU	~250 dB/RIU	[110]
2011	Two UV-written FBGs + microchannels inscribed by fs-laser	1000	Liquid RI	1.43-1.49 RIU	9 nm/RIU	[119]
2011	Air bubble between SMF + MM PCF	44.9	Strain Temp.	0-1850 µε 23-750 °C	2.78 pm/µε 0.981 pm/°C	[121]
2011	SMF + hollow core silica tube	141	Gas Pressure Temp.	0-1.0 MPa 23-950 °C	2.61 nm/MPa 8.11 pm/°C	[122]
2012	Spheroidal cavity between SMF and PCF	10	Strain	0-1000 µε	10.3 pm/µε	[130]
2012	Microbubble between flat tip SMF + hemispherical tip SMF	~100	Strain Temp.	0-1000 µε 100-1000 °C	4 pm/µε 0.9 pm/°C	[132]
2012	SMF + hollow core ring PCF	508	CH$_4$ Pressure Temp.	0-0.8 MPa 23-500 °C	0.82 nm/MPa 3.77 pm/°C	[170]
2012	SMF + PM-PCF with lateral offset	~100	Temp.	33-600 °C	13.8 pm/°C	[136]
2012	SMF + large lateral offset SMF + SMF	416	Gas RI	1.0002-1.0025 RIU	1540 nm/RIU	[127]
2012	Ellipsoidal cavity between SMF + PCF	~14	Liquid RI Temp.	1.332-1.45 RIU 24-95 °C	~61.74 dB/RIU 15 pm/°C	[124]
2012	SMF + hollow core ring PCF + SMF	~13	Strain	0-1000 µε	15.4 pm/µε	[133]
2012	SMF + 50 µm diameter fiber + SMF	2000	Gas RI Temp.	1.000-1.003 RIU 0-300 °C	-1375 nm/RIU 25.6 pm/°C	[125]
2012	SMF + etched GIF625	105	Strain Temp.	100-1200 µε 23-400 °C	6.99 pm/µε 0.95 pm/°C	[134]
	SMF + etched GIF50	43	Strain Temp.	100-1200 µε 23-400 °C	4.06 pm/µε -0.84 pm/°C	
2013	SMF + hollow core PC+SMF + fs laser drilled µchannels	48	Liquid RI Temp.	1.322-1.334 RIU 100-900 °C	851.3 nm/RIU 0.27 pm/°C	[141]

2013	SMF + gold ultra-thin film + SMF	55	Liquid RI Temp.	1.3-1.46 RIU 23-800 °C	-19.8 dB/RIU 13 pm/°C	[144]
2013	SMF + etched double clad optical fiber	~130	Temp.	150-900 °C	14.6 pm/°C	[145]
2014	Air cavity between 2 SMFs	46	Strain Temp.	0-1100 µε 100-600 °C	6.0 pm/µε 1.1 pm/°C	[150]
2014	Air bubble and liquid in hollow core fiber, with taper plug	31	Temp.	25-39 °C	-6.71 nm/°C	[149]
2014	SMF + etched P-doped fiber + coreless all silica MMF and FIB post-processing	172	Temp.	100-300 °C	11.5 pm/K	[154]
2014	SMF + microfiber + SMF	21	Strain Liquid RI	0.05-0.35 N 1.326-1.336 RIU	~200 pm/µε 1330.8nm/RIU	[155]
2014	Silica cavity & spheroidal cavity, both formed in a hollow annular core fiber	392	Strain Temp.	0-1500 µε 23-500 °C	1.1 pm/µε 13 pm/°C	[151]
		50	Strain Temp.	0-1500 µε 23-500 °C	5.2 pm/µε 1.3 pm/°C	
2014	SMF + double-core PCF	~72.3	Temp.	30-900 °C	13.9 pm/°C	[157]
2014	Air bubble in SMF with sub-micron silica diaphragm	~0.5 (diaph.)	Gas pressure	0-2.0 MPa	~1036pm/MPa	[158]
2014	SMF + etched double clad optical fiber + SMF-based diaphragm	~80	Temp. air Temp. water	23-85 °C	13.5 pm/°C 9.4 pm/°C	[152]
2015	SMF + dual hollow core fibers	33.84	Temp. in liquids	20-60 °C	-0.4810 nm/°C	[160]
2015	Polymer capped on the end face of SMF	35.1	Pressure Temp.	0-2.8 MPa 40-90 °C	1.13 nm/MPa 0.249 nm/°C	[161]
2015	Rectangular air bubble between SMFs	~61	Strain Temp.	0-500 µε 25-100 °C	43 pm/µε 2.0 pm/°C	[165]
2015	SMF + silicon pillar	200	Temp.	20-100 °C	84.6 pm/°C	[167]
2015	MMF + Pyrex glass + silicon diaphragm	~32	Temp.	-50-100 °C	6.07 nm/°C	[168]
2015	SMF + hollow core fiber + polyimide diaphragm	170	Salinity	0-5.47 nm/(mol/L)	0.45 nm/(mol/L)	[169]

Fabry-Perot Cavities Based on Hollow Core

Interferometric Tips
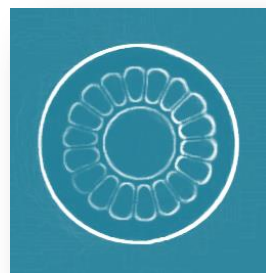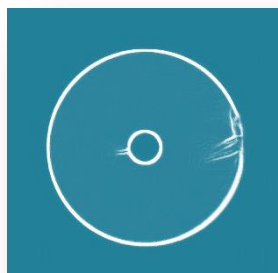
3.1 Introduction

Hollow core structures, such as the silica tube or the hollow core photonic crystal fiber (PCF), have been widely explored by the scientific community over the last two decades. The first sensor based on a hollow core silica tube was proposed in 1993 by Sirkis *et al.* [41] and it was used for strain sensing. Since then, this simple structure was applied in a wide variety of configurations and found different applications such as in humidity sensing [171], microfluidic refractive index sensing [172], in the measurement of the thermo-optic coefficient of liquids [160], temperature [91, 149, 173], refractive index [104] and pressure sensing [77]. A hollow core silica tube was also used as a spatial optical filter and it was characterized in strain, temperature and refractive index [174].

On the other hand, the hollow core PCF is extremely attractive for biological [175] and chemical applications. Considering the latter case, the detection of molecules in liquid media [176-180] or gas sensing [181-183] have been proposed. The structure is highly suitable for such applications due to the strong interaction of light with the analyte, provided by the large hollow area where light propagates. Zhao *et al.* proposed the filling of a hollow core PCF with magnetic fluid for the measurement of magnetic fields [184]. Strain and temperature measurements were also addressed by incorporating the hollow core PCF in a Fabry-Perot (FP) configuration [85], in a modal interferometer [185] and in a Sagnac interferometer [186].

The measurement of pressure in liquid or gas media using optical fiber sensors has been the subject of extensive research. There are many possible direct applications in industry, namely in hazardous environments, where high resolution gas pressure sensors are required. On the other hand, given the biocompatibility of silica, and the reduced dimensions of these sensors, they become attractive solutions for liquid low-pressure measurements, in the range of physiological activity pressures. Many different types of gas sensors have been proposed over the last years. For instance, Kao *et al.* reported the use of a FP cavity with internal mirrors bonded at one end to a stainless-steel diaphragm that was subjected to air pressure variations [49]. In 2004, the use of an

extrinsic FP interferometer was proposed to measure nitrogen (N_2) pressure [69, 72]. From the relationship between pressure and refractive index of N_2, it was possible to monitor the changes in the gas refractive index.

The development of gas pressure sensing structures at the tip of the optical fiber usually comprises the use of a hollow core section and a thin diaphragm. The hollow section can be obtained by using, for example, a hollow core silica tube [77, 109, 187], etched multimode fibers [138, 188, 189] or even UV-molded polymers [190]. Regarding the diaphragm, it can be made of a polymeric material [74], of a polymer-metal composite [190, 191], or it can be constituted of fused silica [7, 114]. A FP cavity based on a polymer droplet at the tip of a fiber has also been proposed [161]. Long period gratings written in PCFs were also tested for the measurement of argon (Ar) pressure [192]. Duan *et al.* spliced a short section of single mode fiber (SMF) in between two sections of SMF with a large lateral offset and tested it under air pressure variations [127]. Silva *et al.* spliced a 50 μm diameter optical fiber between two sections of SMF and tested it in a N_2 atmosphere with variable pressure [125]. Table 3.1 collects sensitivities attained by several groups for the measurement of gas pressure.

Table 3.1 - Different fiber optic gas pressure sensors based on FP configurations, with the respective characteristics.

Year	Configuration	Gas	Sensitivity	Comments	Ref.
2005	Air gap between two SMFs in ferrule	N_2	4.17 nm/MPa	Extrinsic configuration	[72]
2005	SMF + step index + etched GIF + step index	N_2	-39.21 nm/MPa	Air gap variation	[188]
2011	SMF + hollow core silica tube	N_2	2.61 nm/MPa	Diaphragm-free	[122]
2012	FBG + UV molding polymer FP cavity	air	1537.4 nm/MPa	Cavity length variation	[190]
2012	SMF + etched GIF + hollow core silica tube	O_2 CO_2	3.6 nm/MPa 6.4 nm/MPa	Two different cavities; maximum sensitivities	[189]
2012	SMF + hollow core ring PCF	N_2	3.04 nm/MPa	Diaphragm-free	[170]
2014	SMF + air bubble with thin diaphragm	air	~1.036 nm/MPa	All-silica, ultra-thin diaphragm	[158]
2015	SMF + pendant polymer droplet	air	1.130 nm/MPa	Polymer cavity	[161]

In this Chapter, two different configurations are proposed for the measurement of pressure in a gas atmosphere. The first device is a diaphragm-free FP interferometer based on a hollow-core silica tube, whereas the second device is based on a diaphragm-free hollow core ring PCF. Both sensors are also characterized in temperature. The simplicity of fabrication and the reproducibility of the results make the former device a good alternative to other optical fiber pressure sensors. The second configuration, on the other hand, due to its physical characteristics, translates into a robust, reliable and easy to produce device, which presents higher sensitivity to N_2 pressure than the one based on the hollow core silica tube. Finally, a different application of the hollow core ring PCF is addressed. In this case, the FP cavity has a polymeric diaphragm, which is tested in a liquid environment where it is possible to monitor pressure changes in the range of the intravascular pressure variations.

3.2   Theoretical Considerations

The measurement of the refractive index of gases has been a challenge for the scientific community. The behavior of a gas in a sealed container is highly complex due to the extremely large amount of particles involved and the degrees of freedom they can show. The treatment of such system is, therefore, of a statistical nature. Instead of looking at the movement of a single particle, it is more suitable to study the macroscopic quantities that come as a result of the interactions of all particles contained in the closed system, such as energy, pressure or temperature [193]. Statistical physics indicates that in a sealed chamber the refractive index of a gas, related to its density, depends on three different parameters, as will be shown later: wavelength of operation, pressure and temperature.

The sensors described in this Chapter were subjected to N_2 and methane (CH_4) gas pressure changes, starting from low vacuum (~10^{-3} MPa) up to 1 MPa. Considering, for simplicity, a FP cavity with low reflectivity mirrors, it can be approximated by a two-wave interferometer. In such case, the reflection spectrum is essentially determined by the phase difference, $\Delta\phi$, between the waves generated in the two reflections [147]:

$$\Delta\phi = \frac{4\pi n_{eff} L_{FP}}{\lambda}, \tag{3.1}$$

where n_{eff} is the effective refractive index of light travelling within the cavity, L_{FP} is the cavity length and λ corresponds to the operation wavelength. When $\Delta\phi = 2m\pi$, where m is an integer, the reflection spectrum reaches a maximum, which happens for the wavelengths:

$$\lambda = \frac{2n_{eff} L_{FP}}{m}. \tag{3.2}$$

If there is an external perturbation to the cavity, both n_{eff} and L_{FP} can be affected, translating into a phase change which affects the cavity channeled spectrum. When the external perturbation is caused by pressure changes (p), the sensitivity of the cavity can be determined by differentiating Eq. 3.2:

$$\frac{d\lambda}{dp} = \frac{\partial\lambda}{\partial n_{eff}}\frac{\partial n_{eff}}{\partial p} + \frac{\partial\lambda}{\partial L_{FP}}\frac{\partial L_{FP}}{\partial p}. \tag{3.3}$$

Since

$$\frac{\partial\lambda}{\partial n_{eff}} = \frac{2L_{FP}}{m} \wedge \frac{\partial\lambda}{\partial L_{FP}} = \frac{2n_{eff}}{m}, \tag{3.4}$$

by substituting Eqs. 3.4 into Eq. 3.3, it comes that

$$\frac{d\lambda}{dp} = \frac{2L_{FP}}{m}\frac{\partial n_{eff}}{\partial p} + \frac{2n_{eff}}{m}\frac{\partial L_{FP}}{\partial p}. \tag{3.5}$$

Dividing orderly Eq. 3.5 by Eq. 3.2, the wavelength dependence on the applied pressure is given by

$$\frac{d\lambda}{dp} = \lambda\left(\frac{1}{n_{eff}}\frac{\partial n_{eff}}{\partial p} + \frac{1}{L_{FP}}\frac{\partial L_{FP}}{\partial p}\right). \tag{3.6}$$

Thus, the sensor interferometric spectral response to the applied pressure, which corresponds to a phase variation, is the result of two contributions: the dependence of the effective refractive index on pressure and the change of the FP cavity length with this

parameter. However, for the silica based sensors presented in this Chapter, the variation of the cavity length with pressure is extremely small and can be ignored. Thus, the dominant effect here is the change of the n_{eff} with the applied pressure.

On the other hand, the refractive index of a gas is dependent on three different parameters: wavelength, temperature and pressure, as previously mentioned. There are several equations in the literature for the calculation of the gas refractive index [194-198]. However, the ranges of validity are extremely limited. Regarding the measurement of N_2 with optical fiber sensors, several authors used the updated Édlen's equation for air as a first approximation [194]. Besides the fact that this equation is only valid for wavelengths between 350 nm and 650 nm, and for low pressure (close to atmospheric pressure), air is constituted by several components: 78.09% N_2, 20.95% O_2, 0.93% Ar, 0.03% CO_2 [194, 199].

Recently, Zhang *et al.* reported precision measurements for the refractive index of N_2, among other gases [200]. A Mach-Zehnder interferometer setup was used, where the light source was a frequency comb. The derived equations were based on the works of Édlen [194], Birch *et al.* [199, 201], and Bönsch *et al.* [202], and were compared with the results of Peck *et al.* [203]. Here are summarized the main results, which set the basis for the conversion of pressure into refractive index variations for N_2. According to Édlen, the refractive index of a gas can be determined by

$$(n-1)_{Tp} = (n-1)_s \frac{D_{Tp}}{D_S},$$

(3.7)

where $(n-1)_{Tp}$ depends on temperature, T (in °C), and pressure, p (in Pa), and $(n-1)_s$ is obtained for the refractive index under standard conditions (101325 Pa and 15 °C), and only depends on the wavelength (in μm). D_{Tp} is the density factor and D_S is the density factor for standard gas conditions. In order to determine D_{Tp}, it is necessary to estimate first the compressibility factor, Z. Using the equation of state as defined by Édlen [194] ,

$$\frac{pV}{RT} = Z,$$

(3.8)

the dependence of Z on temperature at 101325 Pa (1 atm) can be obtained from the tables reported in the literature. In this Eq. Zhang and co-workers used the ones from NIST [204]. There is also an older publication [205] where these values can be found. Anyway, according to Zhang *et al.*,

$$Z = 1 - 101325\left(0.449805 - 0.01177T + 0.00006T^2\right) \times 10^{-8}. \tag{3.9}$$

Édlen also stated that Z is a function of pressure and temperature, according to $Z = 1 - \varepsilon_T p$, where ε_T is a parameter that depends linearly on temperature. Combining this relation with Eq. 3.8, $\varepsilon_T p$ can be estimated and substituted in Eq. 3.10 for the density factor, which is then given by [202]

$$D_{Tp} = p\frac{1 + \varepsilon_T p + (n-1)/6}{1 + \alpha T}, \tag{3.10}$$

where $\alpha = 1/273.15\ K^{-1}$, and $(n-1) \approx K_\lambda\, p/(1 + \alpha T)$ is a correction factor, given by the mean values of temperature and pressure considered. K_λ is determined through the refractive index of N_2 at standard conditions. The density factor is then

$$D_{Tp} = p\frac{1 + p\left(0.498526 - 0.0119484T + 0.00006T^2\right) \times 10^{-8}}{1 + 0.0036610T}. \tag{3.11}$$

Thus, the relationship between the refractive index term dependent on the temperature and pressure and the refractive index term dependent on the wavelength is given by

$$(n-1)_{Tp} = \frac{D_{Tp}}{94439.27}(n-1)_S, \tag{3.12}$$

where

$$(n-1)_S \times 10^8 = 6497.378 + \frac{3073864.9}{144 - 1/\lambda^2} \tag{3.13}$$

is the dispersion curve given by Peck *et al.* for a temperature of 15 °C [203]. The reason why this equation has been adopted is because it is valid from ~470 nm to ~2060 nm, being in better agreement with our experimental conditions than the one proposed by Zhang and co-workers. Fig. 3.1 (a) shows the numerical curve obtained for the variation

of $(n\text{-}1)_S$ with wavelength. Figure 3.1 (b) shows the value of $(n\text{-}1)_{Tp}$ at a constant temperature of 20 °C and a constant wavelength of 1550 nm, as a function of pressure.
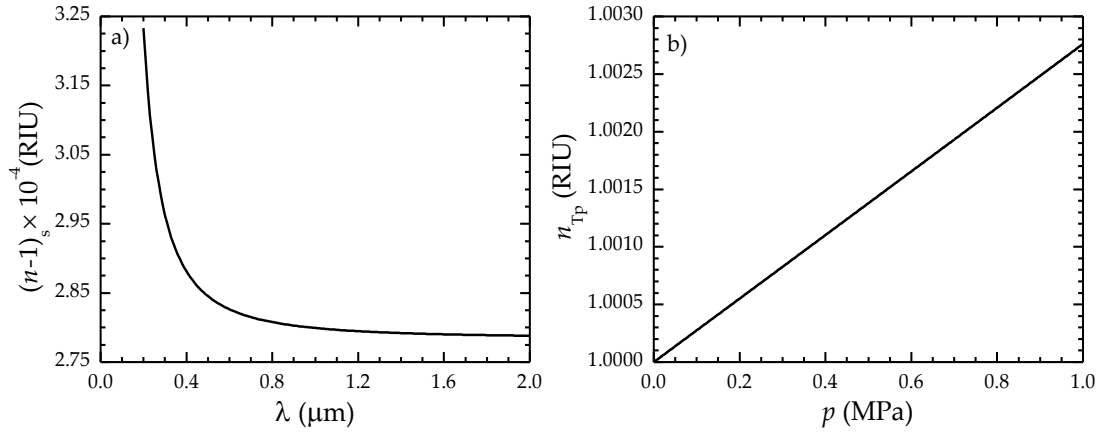
Figure 3.1 – Numerical curves obtained for the refractive index of N_2 considering (a) the dependence on wavelength, and (b) the dependence on pressure, at a temperature of 20 °C and a constant wavelength of 1550 nm. RIU stands for refractive index units.

The refractive index dependence on the wavelength is nonlinear, decreasing as this parameter increases. However, over the operation wavelength range used in this work, the variation is very small, of the order of 10^{-7} RIU, and can thus be considered constant. Regarding the variation with pressure, the behavior is linear and the change is more significant, as shown in Fig. 3.1 (b).

In this Section, a method to infer the variation of the refractive index of a gas with the applied pressure was described. Using the previous equations, it is possible to determine indirectly the response of a sensor to this parameter. This matter will be discussed in Section 3.3.3.

3.3 Fabry-Perot Cavity Based on a Silica Tube

The Fabry-Perot (FP) cavity developed in this work was based on a hollow-core silica tube, which was produced at the Leibniz Institute of Photonic Technology (IPHT – Jena). The silica tube was made of pure silica and presented an outer diameter of (125 ± 5) µm and an inner diameter of (20 ± 5) µm. The cross-section photograph of this structure is shown in Fig. 3.2.
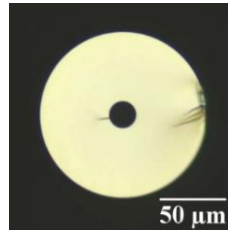
Figure 3.2 – Microscope photograph of the silica tube cross-section.

3.3.1 Sensor Design and Spectral Characteristics

The sensing cavity was produced by fusion splicing a section of silica tube to single mode fiber (SMF). The fiber and the silica tube were placed in the splicing machine with a lateral offset, as shown in Fig. 3.3 (a) [206]. This procedure ensured that the arc discharge was mainly applied in the SMF region, preventing the collapsing of the silica tube in the splice region (see Fig. 3.3 (b)). The silica tube was then cleaved with the desired length, under a 5× magnifying lens (Fig. 3.3 (c)). Several devices were fabricated, with cavity lengths that ranged from ~140 µm up to ~1100 µm. The microscope photograph of one of the cavities produced is shown in Fig. 3.3 (d).
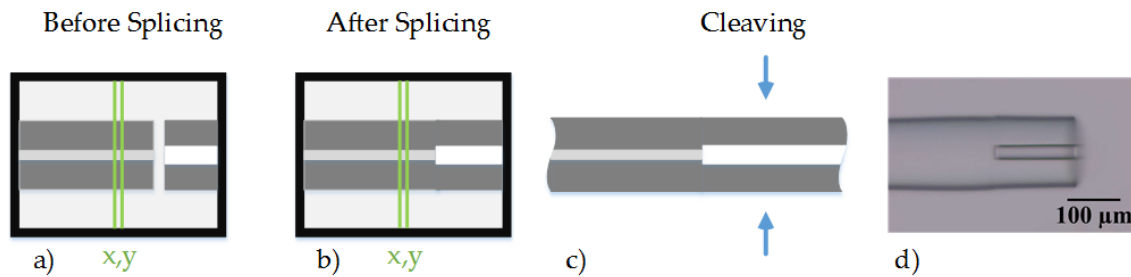
Figure 3.3 – Schematic of the procedures used to fabricate the FP cavity: (a) image from the splicing machine display, evidencing the lateral offset, prior to splicing (SMF on the left and silica tube on the right), (b) image after splicing, (c) device prior to cleaving, the arrows indicate where the cleave should be done and (d) microscope image of a FP cavity produced with this method.

The spectral response of this sensing structure was observed by connecting it to an optical circulator. A broadband optical source and an optical spectrum analyzer (OSA) were connected to the other two ports of this optical component, in a typical reflection scheme, as shown in Fig. 3.4. The optical source had a bandwidth of 100 nm, centered at 1570 nm. The readings were done with a resolution of 0.2 nm.
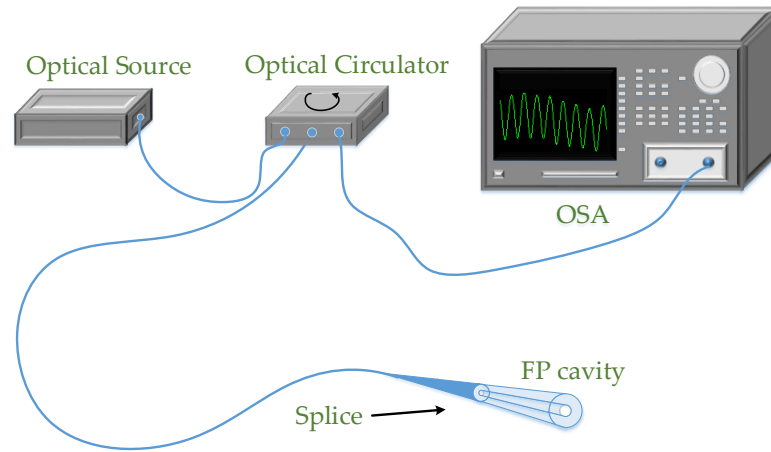
Figure 3.4 – Scheme of the experimental setup.

When the broadband optical source is used in such a reflection scheme, light travelling in the SMF will be reflected at the SMF/silica tube interface. However, a fraction of light is also transmitted onto the walls of the hollow core silica tube. When the light reaches the end face of the silica tube, Fresnel reflection takes place and a fraction of this light is recoupled once again into the SMF (see Fig. 3.5). Also shown in Fig. 3.5 is the photograph of one sample with a large length of silica tube (of the order of centimeters), when illuminated with a He-Ne laser. The reason why such a cavity length was used was to diminish the intensity of light that would travel in the hollow core region, thus enabling the clear observation of light propagating in the silica tube wall.
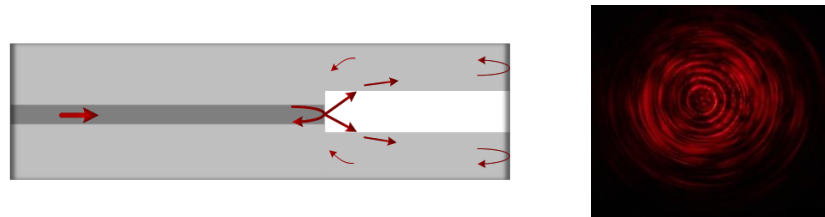
Figure 3.5 – Left: Scheme of the sensing head, highlighting the reflections occurring in the cavity. Right: cross section photograph of one sample when illuminated with a He-Ne laser.

The spectral behavior of four different samples is shown in Fig. 3.6. The spectrum of Fig. 3.6 (a), which corresponds to a cavity length of (141 ± 5) µm, can be approximated to a two-wave interferometer. The increase of the cavity length translates into an excitation of more cladding modes, giving rise to one beat (Fig. 3.6 (b)) or even two different beats, as evidenced in Figs. 3.6 (c - d).
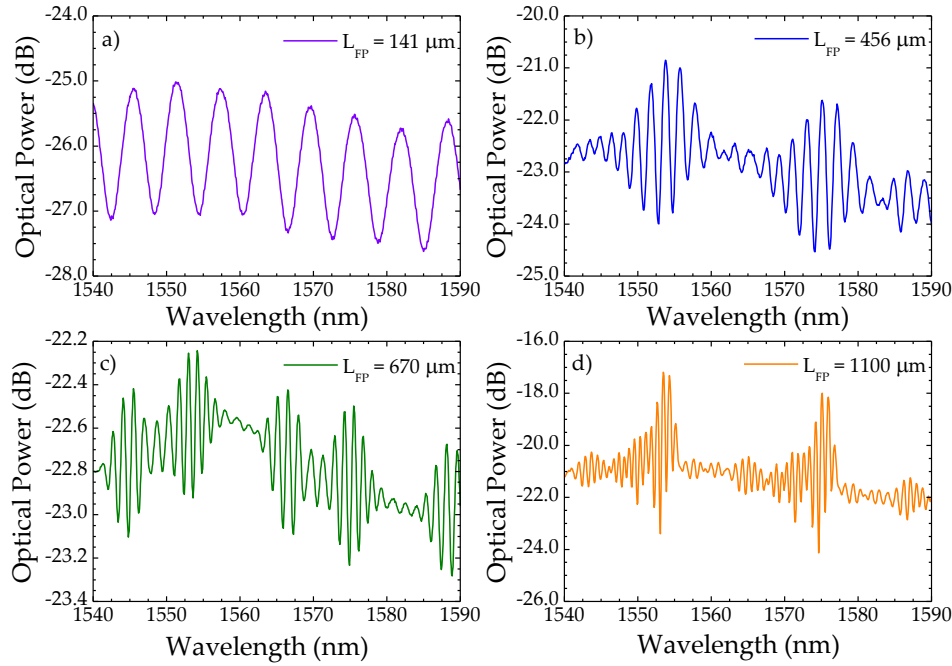
Figure 3.6 – Spectra of four sensing heads with different FP cavity lengths.

This effect can also be observed in the spatial frequency spectra presented in Fig. 3.7. In the case of the shorter cavity, although several modes are excited in the silica tube, only one is recoupled in the SMF, translating into the strong mode observed in Fig. 3.7 (a). For the other samples strong cladding modes, as well as weak ones are excited and involved in the interference. The interference peak with lowest spatial frequency, present in all cases, is related to the optical source.
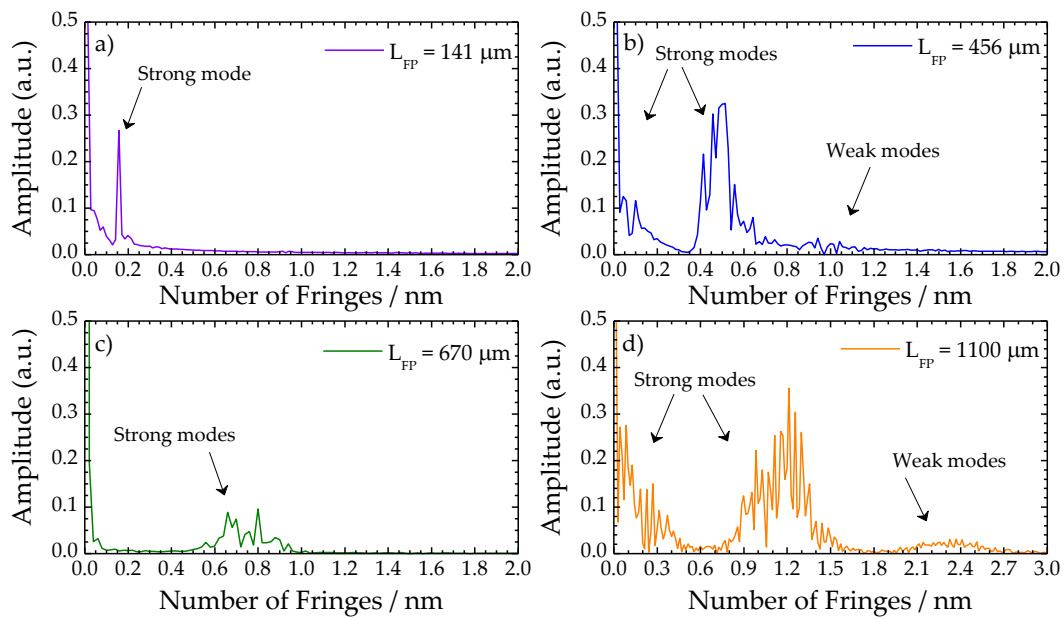
Figure 3.7 – Spatial frequency spectra for four different cavity lengths.

The spectral behavior of the cavity, and consequently, the spatial frequency spectra, are intimately related to the quality of the splices and the end face cleave. Sensors with poor quality present lower spectral visibility and the number of modes that propagate in the cavity can be reduced, as in the case of the sensor with a length of (670 ± 5) μm (Figs. 3.6 (c) and 3.7 (c)).

The subtraction of the wavelengths of two adjacent peaks, $\Delta\lambda = \lambda_2 - \lambda_1$, corresponds to the free spectral range (FSR). This parameter is related to the length of the cavity, L_{FP}, by the equation

$$\Delta\lambda = \frac{\lambda_1 \lambda_2}{2 n_{eff} L_{FP}}. \tag{3.14}$$

where it was considered that $\lambda_1 \simeq \lambda_2$, so that the effective refractive index, $n_{eff}(\lambda)$, was constant. Thus, from this relationship it is possible to estimate the n_{eff} within the cavity. The length of each sensing device was measured through the microscope photographs, whereas the two adjacent peak wavelengths were obtained from the sensing heads spectral response. The relationship between $\Delta\lambda$ and L_{FP} is shown in Fig. 3.8. From the fitting tendency curve, the n_{eff} was estimated to be (1.32 ± 0.03) RIU. The value obtained is closer to the refractive index of silica than the refractive index of air, which indicates that a significant fraction of light propagates inside the silica tube walls.
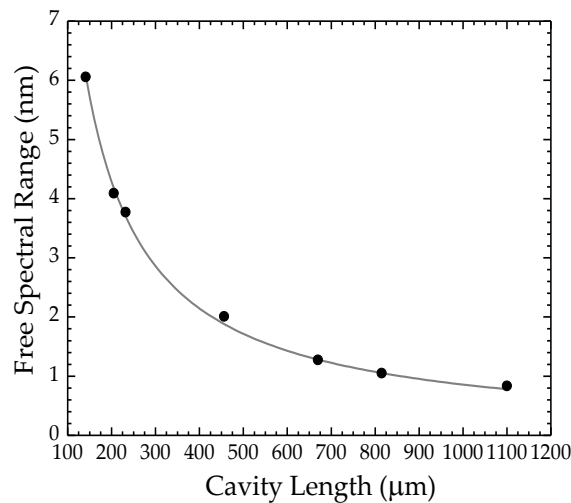
Figure 3.8 – Free spectral range dependence on the cavity length, considering two adjacent peaks with wavelengths close to 1550 nm.

3.3.2 Temperature Measurement

The 141 µm long sensing device was placed inside a tubular oven, in a centered position. The temperature was increased in steps of 50 °C, with an equipment resolution of 0.1 °C. The range of temperatures was between room temperature (~23 °C) and 950 °C. The wavelength shift with the applied temperature was determined by tracking the 1556.6 nm peak, and it is shown in Fig. 3.9. The experimental results were well adjusted by the second order polynomial

$$\lambda = \left(1.2 \pm 0.2\right) \times 10^{-6} T^2 + \left(6.5 \pm 0.3\right) \times 10^{-3} T + \left(1556.3 \pm 0.1\right), \tag{3.15}$$

where λ is the wavelength, in nm, and T corresponds to the temperature, in °C. It is reasonable to divide the temperature range into two different regions: low temperatures, between room temperature and 500 °C, and high temperatures, between 550 °C and 950 °C. According to the insets in Fig. 3.9, a linear behavior is observed in both cases. The sensitivities obtained were (7.1 ± 0.2) pm/°C and (8.1 ± 0.2) pm/°C, respectively.
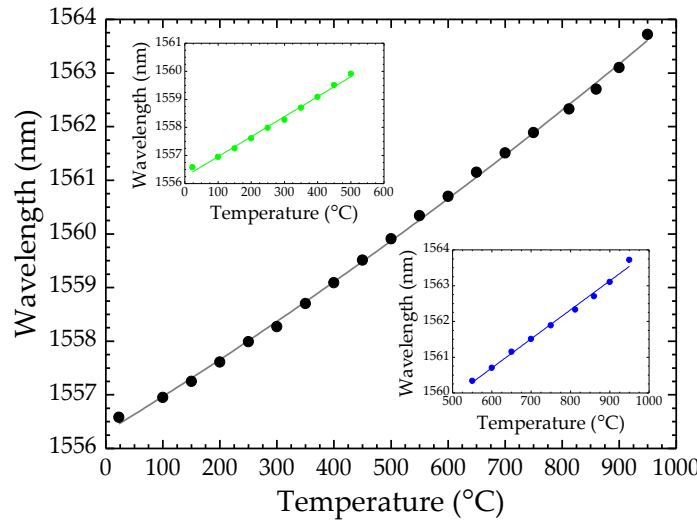
Figure 3.9 – Temperature response of the 141 µm long sensing head. Inset 1 (top left): low temperatures response; inset 2 (bottom right) high temperatures response.

3.3.3 Pressure Measurements

Pressure measurements were carried out on four different samples, one with (170 ± 5) µm cavity length, which still presented the two wave interferometer behavior, and the remaining three were the ones presented in Fig. 3.6 (b-d). The sensors were placed inside a sealed chamber, with a gas input and a low-vacuum purge output

($p \sim 10^{-3}$ MPa). The gas under test was N_2 and all experiments were done at room temperature (~20 °C). The wavelength shift dependence on pressure, for all samples, is shown in Fig. 3.10. The shift was determined by following the peak near 1550 nm. The behavior is approximately linear in all cases, and the sensitivities are reunited in Table 3.2.
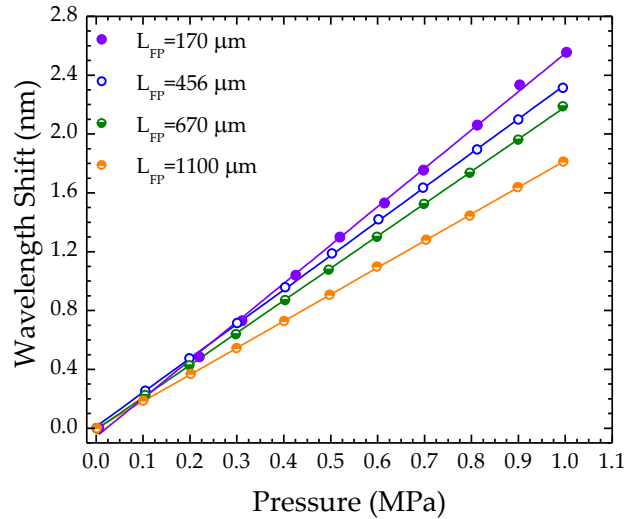
Figure 3.10 – Sensing heads response to the applied pressure.

Besides the relatively high sensitivity to pressure obtained with this simple diaphragm-free structure, the decrease of the sensitivity with the increase of the cavity length was somehow surprising. From the analysis of Eq. 3.6 this behavior seems explained, however, the influence of the cavity length change with pressure was considered to be very small, in agreement with [187]. Therefore, the effect of the second term in Eq. 3.6 is negligible. Thus, the sensitivity to pressure had its origin on the dependence of the gas refractive index on pressure. When pressure increases, there is a higher density of gas inside the sealed chamber, translating into a higher refractive index. Thus, there will be higher interaction between the evanescent field of light travelling in the FP cavity and the gas, which means an increase of the pressure sensitivity with the cavity length, contrary to what is observed. This points out the presence of more complex effects, a matter that will be discussed in the next Section, where a FP structure based on a photonic crystal fiber is subjected to different gases.

By converting the pressure shifts to refractive index variations, according to the Eq. 3.12, the four sensors response regarding this parameter was determined. The

results, shown in Fig. 3.11, also exhibit linear behavior, whose sensitivities are presented in Table 3.2.
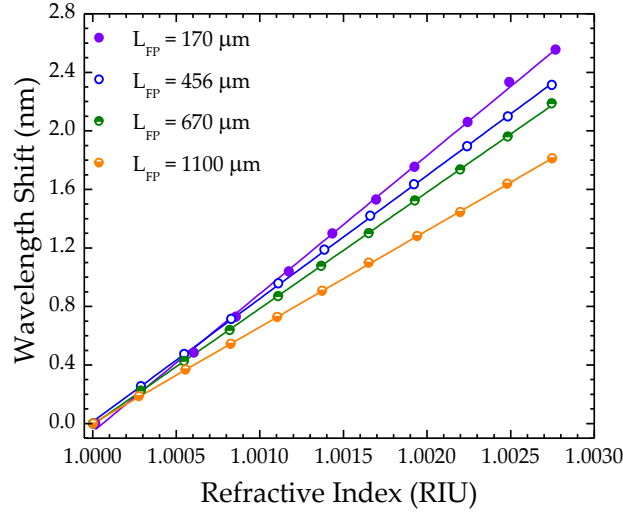
Figure 3.11 – Sensing heads response to the N_2 refractive index change. All measurements were done at room temperature (~20 °C), and the monitored wavelength was around 1550 nm.

Table 3.2 – Sensitivity of the different sensing heads to N_2 pressure and to refractive index.

Hollow core diameter (μm)	FP cavity length (μm)	Pressure sensitivity (nm/MPa)	Refractive index sensitivity (nm/RIU)
20 ± 5	170 ± 5	2.61 ± 0.02	943.8 ± 8.3
	456 ± 5	2.32 ± 0.01	841.7 ± 3.2
	670 ± 5	2.19 ± 0.01	794.7 ± 2.1
	1100 ± 10	1.82 ± 0.01	659.2 ± 1.4
60 ± 5	187 ± 5	2.97 ± 0.01	1074.3 ± 4.8
	680 ± 5	2.26 ± 0.04	818.8 ± 3.4

The influence of the hollow core diameter was studied by using a second hollow-core silica tube with an inner diameter of (60 ± 2) μm. Two sensors were fabricated following the procedures described in Section 3.3.1 and tested to pressure, using the same experimental setup and experimental conditions as previously described. The shorter sensing device had a length of (187 ± 5) μm and the effective refractive index, determined through Eq. 3.14, was of (1.13 ± 0.02) RIU. The longer sensing head presented a length of (680 ± 5) μm and an effective refractive index of (1.25 ± 0.02) RIU. In both cases the effective refractive index is lower than in the sensors previously studied. This difference arises from the higher interaction of light with the external medium when it exits the SMF, prior to being recoupled to the silica wall. Besides, the distance between

these two regions increases significantly for the larger hollow core, meaning that the path where light travels inside the silica tube wall is reduced, when compared with the silica tube with an inner diameter of 20 µm. The decrease in the effective refractive index of light translates into a higher sensitivity to pressure, and consequently, to the refractive index variation, as it is observed in the sensors response shown in Fig. 3.12. The sensitivities of the two samples are shown in Table 2.2, for an easier comparison with the previous results.
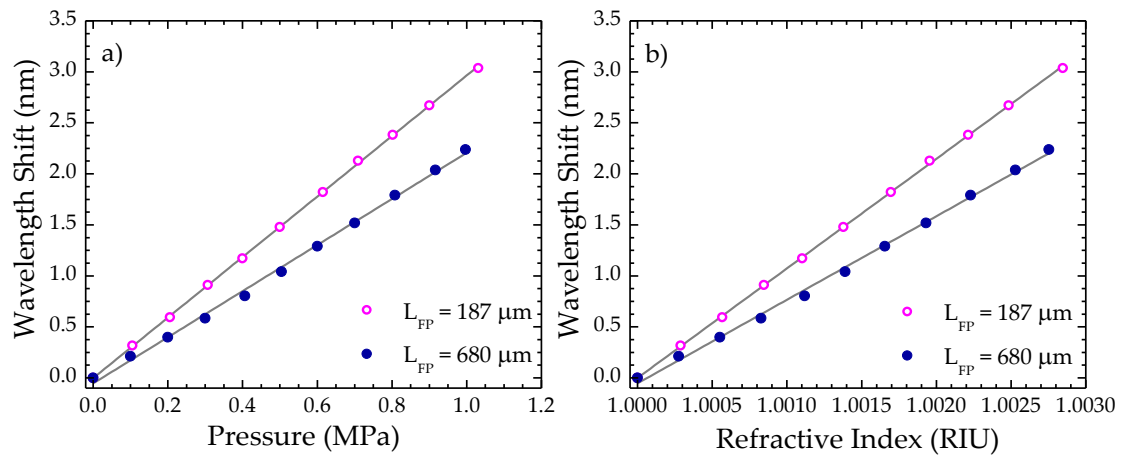
Figure 3.12 - Sensing heads response to the N_2 (a) pressure and (b) refractive index change. All measurements were done at room temperature (~20 °C), and the monitored wavelength was around 1550 nm. The hollow core silica tube presented an inner diameter of ~60 µm.

Even though the variation of the cavity length with the applied pressure is reduced, its physical dimensions (length and the cross section area) are of the utmost importance for the performance of this sensing device. A compromise must be assumed in order to achieve the highest sensitivity possible: a large hollow-core area, but not so large that the silica tube becomes easily damaged when handled; and a small cavity length, although long enough to guarantee that light is coupled to the silica walls and is reflected at the end face, creating the FP cavity.

3.4 Fabry-Perot Cavity Based on Hollow-Core Photonic Crystal Fiber

The FP cavity tested in this work was based on a hollow-core ring photonic crystal fiber (HCR-PCF) produced at the IPHT–Jena. Figure 3.13 (a) shows the cross-section image of the HCR-PCF when observed with a scanning electron microscope (SEM). This fiber presented a large hollow-core, with a diameter of (44.4 ± 0.2) µm, and 18 petal

shaped holes with an azimuthal diameter of (24.4 ± 0.2) μm. In between these two hollow structures there was a silica ring with a thickness of (3.1 ± 0.2) μm.
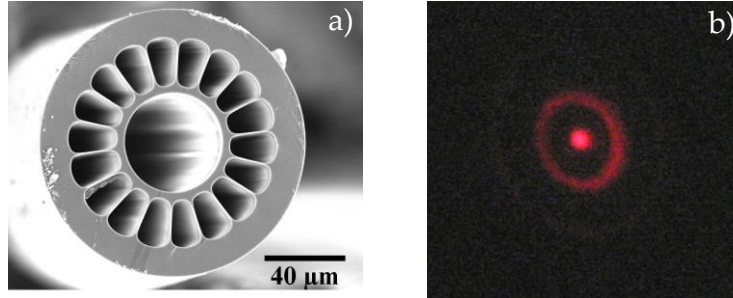
Figure 3.13 – Photographs of the hollow core ring fiber cross-section (a) at the scanning electron microscope (SEM) and (b) when illuminated with a He-Ne laser.

3.4.1   Sensor Design and Spectral Characteristics

The FP cavities were obtained by fusion splicing the HCR-PCF to the SMF, using the same method presented in Section 3.3.1. Several samples were fabricated with different cavity lengths. The light travelling from the SMF end face excites the HCR-PCF ring. Afterwards, it is reflected at the cleaved end face of the HCR-PCF and recoupled once again to the SMF. Figure 3.13 (b) shows the cleaved end face of a HCR-PCF section when illuminated with a He-Ne laser, where it is possible to clearly see the illuminated ring. If the length of the FP cavity is lower than ~160 μm, the optical path is very small and the ring is not excited. In such case, the numerical aperture (0.14 for SMF) is out of the cavity length. However, when the length of the FP cavity is larger than 160 μm, the ring is excited and interference is generated.

The experimental setup used in the experiments was similar to the one described in Section 3.3.1. All measurements, of pressure and temperature, were carried out with an OSA resolution of 0.1 nm.

The spectral behavior of three different FP cavities is shown in Fig. 3.14. The smaller sensing device, with a cavity length of (360 ± 3) μm, presented a spectral response that can be approximated to that of a two-wave interferometer. In this case, the FSR was of (5.7 ± 0.1) nm. The FSR calculated for the (506 ± 3) μm and (1070 ± 5) μm long sensing

heads was of (2.2 ± 0.1) nm and (0.9 ± 0.1) nm, respectively. The operation wavelength considered was ~1555 nm.

For the longer sensing heads, the interferometric patterns show some beating, suggesting that the interference of more than two waves is occurring. This means that the guidance in the silica ring is multimode. However, the small beating effect together with the reduced thickness of the ring indicate that few modes are guided by the structure.
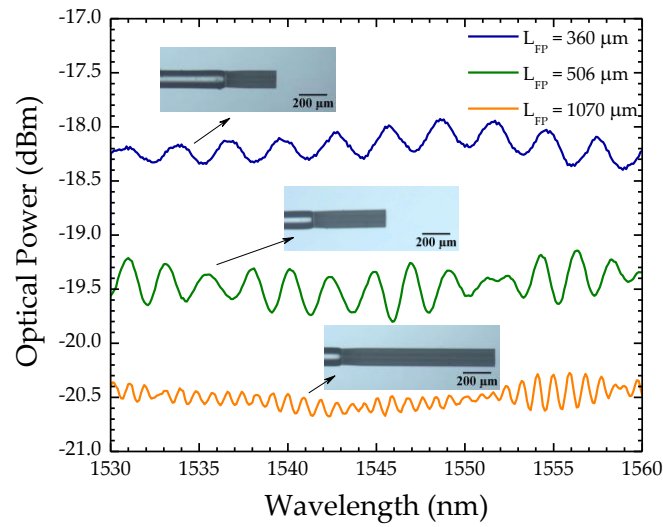
Figure 3.14 – Spectra of three sensing heads based on the HCR-PCF FP cavity.

The group effective refractive index associated with the light propagation can be determined by Eq. 3.14. The values of (1.13 ± 0.01) RIU, (1.17 ± 0.01) RIU and (1.28 ± 0.02) RIU were respectively obtained for the 360 μm, 506 μm and 1070 μm long samples. These values come from the combination of three contributions: the propagation of light in the air, when it exits the SMF core up to the silica ring; the propagation in the silica ring and the evanescent field in air of the light that propagates in this region. The first contribution is more significant for smaller devices, translating into a lower effective group refractive index.

3.4.2 Temperature Measurements

The 360 μm long FP cavity was placed inside a tubular oven and subjected to temperature variations between room temperature (~23 °C) and 500 °C with a resolution of 0.1 °C. A highly non-linear behavior was observed, as can be seen in Fig. 3.15.
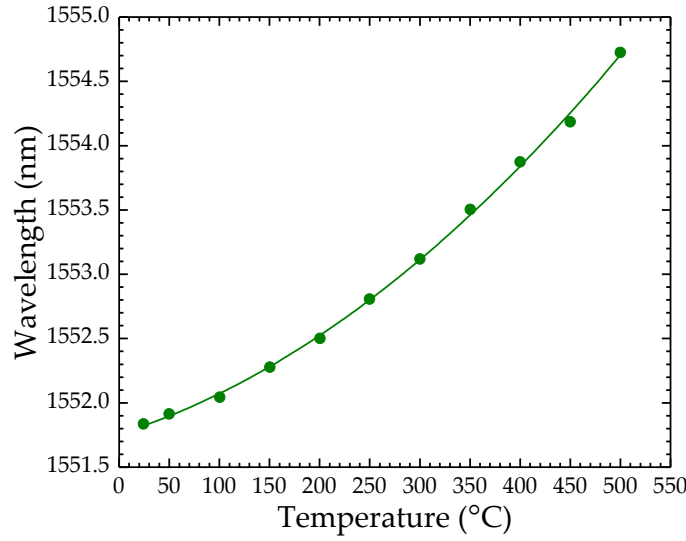
Figure 3.15 – Temperature response of the 360 μm long sensing head.

The experimental data was well adjusted to the second order polynomial

$$\lambda = \left(6.9 \pm 0.5\right) \times 10^{-6} T^2 + \left(2.5 \pm 0.3\right) \times 10^{-3} T + \left(1551.8 \pm 0.1\right), \tag{3.16}$$

where the wavelength comes in nm and the temperature in °C. The range of temperatures can be divided into two different linear regions, for lower and higher temperatures. Below 200 °C the sensitivity was (3.8 ± 0.3) pm/°C, whereas for temperatures above 200 °C, the sensitivity was (7.5 ± 0.3) pm/°C. The values arise from a combination between the thermal expansion and the thermo-optic effects. Similarly to the variation of pressure, when the temperature changes the interferometric spectrum also shifts. In this case, the variation is given by Eq. 3.17, which can be obtained using the same line of thought as for Eq. 3.6:

$$\frac{d\lambda}{dT} = \lambda \left(\frac{1}{n_{eff}} \frac{\partial n_{eff}}{\partial T} + \frac{1}{L_{FP}} \frac{\partial L_{FP}}{\partial T} \right). \tag{3.17}$$

In this equation, $\partial n_{eff} / \partial T$ is the thermo-optic coefficient, which depends on the effective refractive index, and has a value of ~8.6×10^{-6} /°C [207]; and $\partial L_{FP} / \partial T$ corresponds to the thermal expansion coefficient of the fiber material, ~0.55×10^{-6} /°C [126]. Dividing the sensitivity obtained for the high temperatures region by the wavelength (1552.8 nm at 250 °C), we obtain 4.84×10^{-6} /°C, a value relatively close to the thermo-optic

coefficient. This result indicates that this parameter is dominant over the thermal expansion coefficient for this sensing device.

3.4.3   *Pressure Measurements*

The physical characteristics of this HCR-PCF, namely the very thin silica ring surrounded by the petal shaped holes and the large hollow core, make this structure a good candidate to perform gas pressure sensing. To test this hypothesis, two devices were placed in the same sealed chamber as the one described in Section 3.3.3 and were subjected to the variation of pressure in an atmosphere of N_2. The experimental results, shown in Fig. 3.16 (a), were adjusted to a linear function and sensitivities of (3.07 ± 0.03) nm/MPa and (2.46 ± 0.02) nm/MPa were respectively obtained for the 380 μm and 510 μm long FP cavities. There is a clear improvement on the sensitivity for smaller sensing devices, as observed in the previous silica tube configuration.
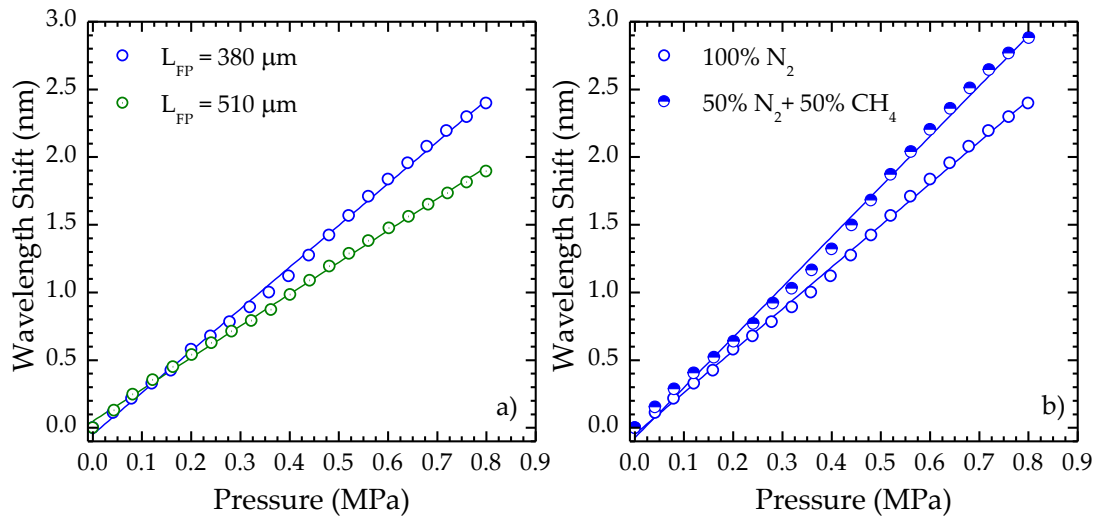
Figure 3.16 – Sensing head response to the applied pressure, (a) atmosphere of N_2, different FP cavity lengths and (b) different gas atmospheres for a cavity length of 360 μm.

The smaller sensing head was also subjected to pressure variations in an atmosphere of 50% N_2 and 50% methane (CH_4). The results are shown in Fig. 3.16 (b), along with the ones obtained for an atmosphere of 100% N_2. By introducing a gas with a different refractive index (higher than the refractive index of N_2), the sensitivity of the device increased from (3.07 ± 0.03) nm/MPa to (3.69 ± 0.05) nm/MPa. This behavior indicates that with a proper calibration, this sensing head can be used to identify the gas present

in the interferometric cavity, by analyzing the response of the sensor to pressure changes.

The results presented here and in the previous Section indicate, for the fiber structures studied, that the sensitivity to pressure decreased with the increase of the sensing head length. At this stage it is not clear what the reasons behind such behavior are, which requires further studies.

3.4.4   *Prototype for Biomedical Applications*

The FP cavity based on the HCR-PCF was further investigated by our group for application in low pressure measurements, creating a prototype suitable to be used in the medical or biomechanical field [208]. This Section describes briefly the sensor and the main results obtained.

A sample with a cavity length of ~125 μm was fabricated using the same procedures as the ones described in Section 3.3.1. At the end face of the HCR-PCF a silicone diaphragm was deposited, by repeatedly placing the tip of the sample in direct contact with a small portion of silicone. After multiple controlled steps, the silicone was cured at room temperature for 72 h. The silicone polymer used was a biocompatible commercial one, Silastic® medical adhesive silicone, type A, from Dow Corning. With the deposition method used to create the sensing device, it was not possible to control the diaphragm geometry, which can have influence on the spectral response. A scheme of the sensor design is shown in Fig. 3.17.
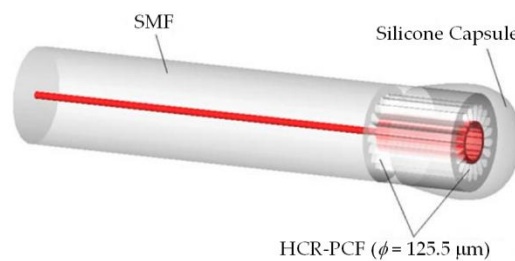
Figure 3.17 – Schematic drawing of the sensor proposed for low-pressure measurements [208].

When illuminated with a broadband optical source, with the same reflection setup as shown in Fig. 3.4, light travelling from the SMF will be reflected at the interface between the HCR-PCF and the silicone capsule, creating a two-wave FP interferometer. In this

case, light will travel in the hollow core, and the effective refractive index is ~1.00 RIU. The spectral behavior of this interferometer is shown in Fig. 3.18. The use of a diaphragm, which will act as one of the FP cavity mirrors, translates into a higher spectrum visibility, when compared to the diaphragm free configuration (whose FP mirror is the 3.1 μm thick silica ring).
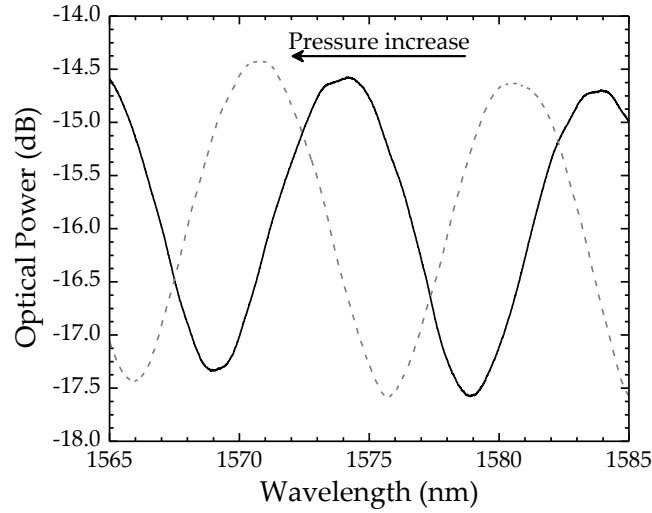
Figure 3.18 – Spectral response of the sensing head. Also shown the spectral shift when hydrostatic pressure is applied (step of 37.5 mmHg).

The visibility of an interferometric cavity can be determined by Eq. 3.18 [209]:

$$V = \frac{P_{max} - P_{min}}{P_{max} + P_{min}},$$ (3.18)

where P_{max} and P_{min} are the optical powers of two adjacent maximum and minimum of the interference signal, respectively. The diaphragm free configuration presented a visibility of ~3 %, whereas in this case its value was ~33 %.

The sensor was then placed inside a hydrostatic pressure device, and pressure measurements in a range between 0 mmHg and 337.5 mmHg were carried out, with a pressure step of ~37.5 mmHg. The spectrum shifted towards shorter wavelengths (blue shift) as pressure increased (see Fig. 3.18). The sensor response was approximately linear, as shown in Fig. 3.19, and a sensitivity of (-87.0 ± 0.4) pm/mmHg was achieved, which corresponds to a sensitivity of (-652.2 ± 3.3) nm/MPa in SI pressure units. This negative response was due to the change in the cavity length, caused by the silicone diaphragm compression with the applied pressure.
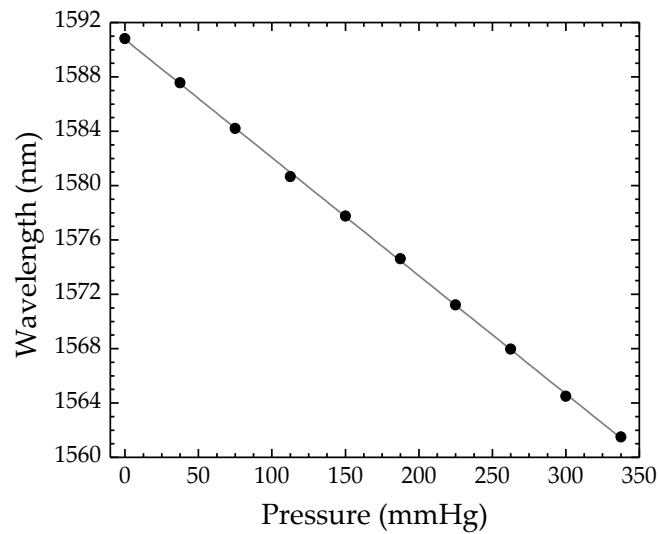
Figure 3.19 – Sensor response to hydrostatic pressure variation.

This sensor proved to be suitable for low pressure applications, exhibiting high sensitivity and good reproducibility. There are several physiological pressures in this range, such as blood pressure, intracranial and intra-articular pressures [208]. However, the use of the silicone capsule brings also higher thermal sensitivity, due to the high thermal expansion coefficient of this material. The typical value of this parameter is $342.0 \times 10^{-6}\,/°C$ [208], which is more than 600 times largerr than that of silica ($\sim 0.55 \times 10^{-6}\,/°C$ [126]). Thus, in practical applications, the sensor should be used in a controlled environment or a reference sensor should be used, to reduce the cross-sensitivity effects.

3.5 Final Remarks

In this Chapter, two different gas pressure sensors based on the Fabry-Perot (FP) configuration were proposed. The sensor based on a hollow core silica tube was the first reported in the literature to measure gas pressure without the use of a diaphragm. Its simplicity and the somehow surprising good response to the measurand translated into a different approach for gas sensing using micro-cavities. Different samples were analyzed, with different FP cavity lengths and also with two different hollow core diameters. In order to take the best advantage of this configuration, a compromise must be accepted: on the one hand, small cavities ensure higher sensitivity, although they

should be long enough to ensure the coupling of light in the hollow core structure; on the other hand, larger hollow core diameters are preferred. However, large enough so they remain easy to handle and mechanically robust.

Regarding the sensor based on the hollow core ring photonic crystal fiber described in the second part of this Chapter, it proved to be more sensitive than the first configuration. This occurs due to the thin thickness of the silica ring, where light travels after it exits the single mode fiber. Thus, the evanescent field in this cavity is stronger, and its interaction with the external medium is larger, translating into improved sensitivity to gas measurements. The cavity was subjected not only to nitrogen pressure variations, but also to those of a mixture of nitrogen and methane, exhibiting different sensitivities. Using a model reported in the literature, the pressure measurements were converted to the gas refractive index variations, and the analysis was also done regarding this parameter. Finally, both cavities presented a non-linear behavior when subjected to temperature.

The sensor based on the hollow core photonic crystal fiber was further investigated by depositing a capsule of a biocompatible silicone at the end of the sensing tip. When subjected to hydrostatic pressure, in the range of physiological activity, the diaphragm deflected, causing a phase shift in the interferometric spectrum. This new prototype can be further explored to be used in low-pressure applications, such as in biomechanics or medicine.

Fabry-Perot Cavities Based on Post-Processed Interferometric Tips
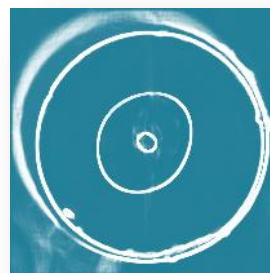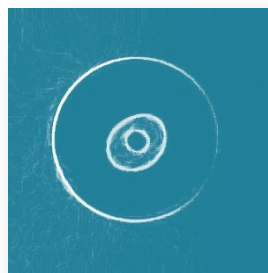
4.1 Introduction

In 1974, Kawakami *et al.* developed a new type of fiber, with one core and two claddings [210, 211]. This fiber was called double clad fiber (DCF)[1] and in the first work, the inner cladding presented the lowest index, followed by the index of the outer cladding. The core presented the highest refractive index. This fiber was proposed to compensate the glass dispersion, since it presented an anomalous waveguide dispersion. In this case, the parameter $d^2\beta/d\omega^2$, related to the signal distortion, is negative, whilst for the standard single mode fiber (SMF), this parameter is positive. Figure 4.1 (a) shows the cross-section scheme of this new type of fiber. In 1978, a new geometry was proposed for the inner cladding [212]. The fiber, birefringent and polarization maintaining, included an elliptical cladding, shown in Fig. 4.1 (c). Until the 1990s, these fibers were mainly applied for dispersion compensation.
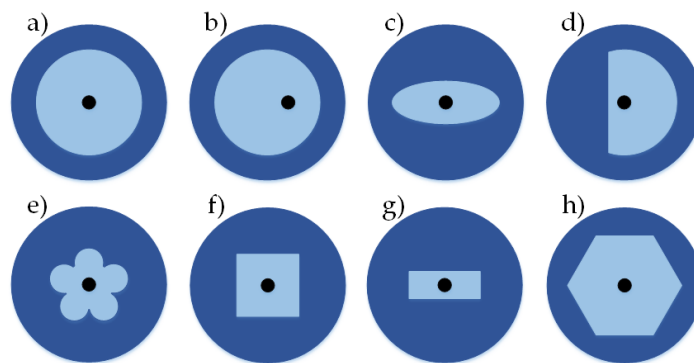
Figure 4.1 – Schematic designs of some of the double clad optical fibers reported in the literature.

In 1988, the use of this kind of fibers in fiber laser configurations was proposed for the first time. For this application, the refractive index of the inner cladding needs to be higher than the one of the outer cladding, ensuring that the pump light is confined in this region. Snitzer *et al.* used a double clad fiber with an offset core doped with neodymium (Nd) [213]. The scheme of the fiber used is shown in Fig. 4.1 (b). Light was focused onto the inner cladding and absorbed by the Nd doped core as it proceeded

---

[1] The acronym DCF is usually attributed, in the literature, to the dispersion compensating fiber. However, several authors also used it to designate the double clad fiber. In the works described in this thesis the dispersion compensensing fiber was not used, and thus the DCF acronym is only relative to the double clad fiber.

along the fiber. By exploiting different geometries for the inner cladding, especially when the circular geometry was broken, high power lasers with outstanding efficiencies were obtained. For instance, Jeong *et al.* proposed the use of a D-shaped fiber, as the one presented in Fig. 4.1 (d), to obtain a 1.36 kW continuous wave output power with a launch power just over 1.6 kW [214]. In this case, a slope efficiency of 83 % and a quantum efficiency of 95 % were attained[2]. Figs. 4.1 (e-h) present several popular configurations, like the "flower"-type [216], the squared [217], rectangular [218], and hexagonal shaped [219]. The difference between the refractive indices of the layers was often attained by doping the core with lanthanide ions, thus increasing the refractive index, and using a low refractive index polymer as the outer cladding [217-219].

The employment of this kind of fibers for sensing has been recently proposed, in different configurations, and for diverse applications. For instance, in 2006, Fu *et al.* proposed the use of a double clad photonic crystal fiber (PCF) in a scheme to perform nonlinear optical endoscopy measurements [220]. Han *et al.* spliced a DCF section to SMF and wrote a long period grating (LPG) in both fibers [221]. The sensor was able to simultaneously measure refractive index and temperature. A band rejection filter was obtained by Pang *et al.* by splicing a DCF section between two SMFs [222]. The sensor was applied in refractive index measurements of liquids. The concatenation of two sensing structures was proposed by Liu *et al.* [223]. The sensor was constituted by two different DCFs. One presented an inner cladding doped with fluorine, whereas the other was doped with boron. The device was employed in temperature and refractive index measurements. Baiad *et al.* proposed the use of a double clad fiber coupler to capture cladding modes which were generated by a gold-coated fiber with a tilted fiber Bragg grating (FBG) [224] or by an etched FBG [225]. All these structures presented an inner cladding with a refractive index lower than the core and the outer cladding indices.

It is possible to obtain an inner cladding with higher refractive index by doping it with elements such as germanium or phosphorous. In such case, the fiber needs to be

---

[2]The slope efficiency of a fiber laser is obtained through the relationship between the absorbed pump power and the emitted laser output power, above threshold. Regarding the quantum efficiency, it is the ratio between the pump and laser photon energies [215].

post-processed, for example by means of chemical etching, in order to guide light in its core. In 2011, Pevec *et al.* proposed the chemical etching of a phosphorous doped DCF to obtain a FP cavity [117]. The sensor was used to measure strain and temperature. Three years later, André *et al.* developed a temperature and vibration sensor based on post-processing of a P_2O_5 doped DCF [154]. Besides wet chemical etching, the structure was post-processed using the focused ion beam (FIB) technique.

In this Chapter, a phosphorus doped DCF subjected to chemical etching is described. Two different configurations are considered, one for measurement of extreme temperatures, and the other to be used as an optical phase refractometer. Some fabrication characteristics are pointed out, as well as the development of the sensing structures. Finally, some theoretical considerations are given and the experimental results are discussed.

4.2   *Design of the Double Clad Optical Fiber*

The phosphorus-doped double clad optical fiber (P-doped DCF) was fabricated at the Leibniz Institute of Photonic Technology (IPHT Jena), in Germany, during a short mission in the framework of COST Action TD1001. The fabrication details are provided in Appendix I. The fiber cross-section is shown in Fig. 4.2 (a). The doped region has an elliptical shape instead of being circular. This unexpected feature was a consequence of the preform fabrication (see Appendix I). The pure silica core and the outer cladding have mean diameter dimensions of (18 ± 3) μm and (122 ± 3) μm, respectively. In between these two regions, the layer of P-doped glass presents a thickness of (15 ± 3) μm, considering the major axis of the ellipse, and (10 ± 3) μm in the minor axis. This region presents a refractive index variation, $\Delta n \sim 1.1 \times 10^{-2}$ RIU, when compared to the undoped ones, as shown in Fig. 4.2 (b). Notice that the experimental value of the refractive index is slightly different from the expected (theoretical) one. This is mostly due to the fact that the inner cladding is not perfectly circular.

Even though the inner cladding shape influences the results, as will be seen later, the fiber was successfully used in two different applications: as a sensor for extreme

temperatures and as an optical phase refractometer. All the details of these two works will be fully given in the next Sections.
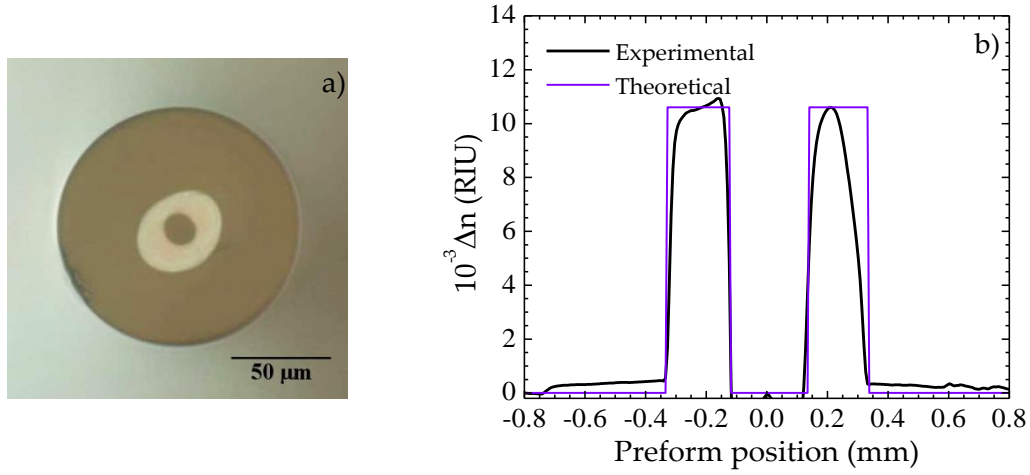
Figure 4.2 – (a) Cross section of the P-doped double clad optical fiber. (b) Refractive index profile measured using a short section of the preform.

4.3 Optical Fiber Tips Design

The optical fiber tips were created by fusion splicing of a section of P-doped DCF with a SMF, using the automatic program of the splicing machine. Afterwards, the P-doped DCF region was cleaved under a 5× magnifying lens. In this way it was possible to obtain cavities with the desired length of a few hundred micrometers. As discussed earlier, the presence of phosphorus in the inner cladding increases the refractive index of this layer when compared to the undoped regions. Thus, light that is guided by the SMF will be deviated from the core and will travel in the doped region of the DCF. Therefore, no interference pattern was initially observed. To overcome this issue, and ensure that the light travels in the fiber core, the samples were subjected to wet chemical etching using a 48 % hydrofluoric acid (HF) solution. Due to the presence of the dopant, the inner cladding was expected to be removed faster than the undoped regions. A preliminary study was then carried out to observe the etching behavior and the formation of the cavities. In order to increase the etching rate, and thus obtain a structure with a nearly constant core diameter over its length, the HF solution was placed inside an ultrasound bath at room temperature. The chemical reactions involved in this liquid phase etching process are [81, 226]:

$$P_2O_5 + 6HF \rightarrow 2POF_3 + 3H_2O, \tag{4.1}$$

$$SiO_2 + 6HF \rightarrow H_2SiF_6 + 2H_2O. \tag{4.2}$$

The formation of the cavity was observed by submerging the sample in liquid HF for a few seconds, quickly removing it from the solution and cleaning it thoroughly with ethanol. A microscope photo was taken, as shown in Fig. 4.3 (a). The sample was once again placed in the etching solution for a few additional seconds and the process was repeated. Figures 4.3 (a-d) show the sample at different processing times.
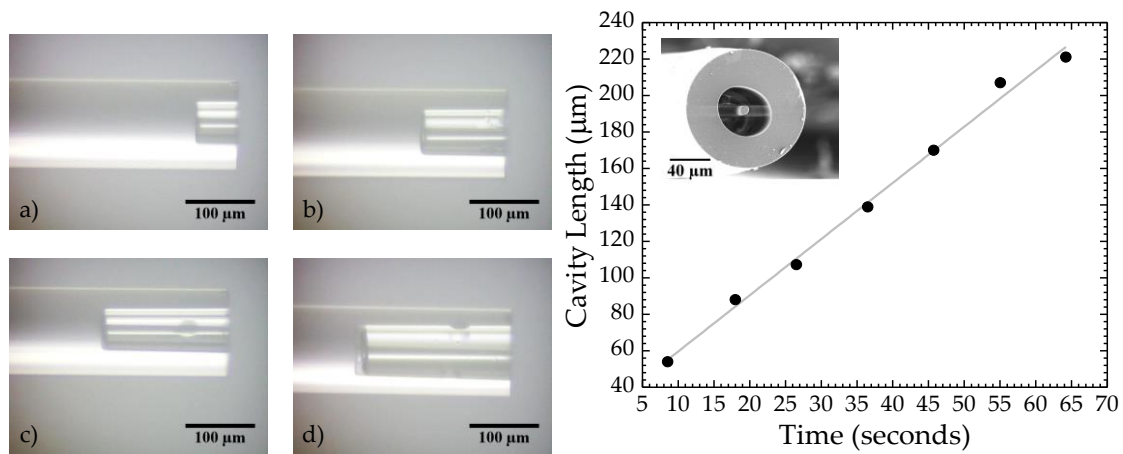
Figure 4.3 – Left: Microscope photos of fiber tip formation after an etching time of a) ~9 s, b) ~27 s, c) ~46 s and d) ~65 s. Right: Cavity length formation vs. time. Inset: SEM image of the etched cavity cross-section.

By measuring the length of the cavity at each time, a linear etching behavior was observed, as depicted in Fig. 4.3 (on the right). From the linear fitting, an etching rate of (3.1 ± 0.1) µm/s was estimated. Thus, in less than one minute it is possible to attain a cavity with a length of ~200 µm. On the inset of Fig. 4.3 the scanning electron microscope (SEM) photograph of the etched cavity top is shown.

Two different sensing structures were created using a short section of this fiber. The steps performed to produce each type of sensor are shown in Fig. 4.4. Following the red arrows, the diaphragm-free configuration, tested for extreme temperatures, is obtained. On the other hand, the blue arrows indicate the procedure used to obtain the cavity with diaphragm, tested as an optical phase refractometer. The first step is to splice a section of DCF with a SMF. Afterwards, the DCF section is cleaved under a magnifying lens, as explained earlier. The third step (and the final one for the first configuration) is to perform wet chemical etching for ~1 min. The fourth and fifth steps are only relative to

the second configuration, and consist of splicing the etched fiber with SMF. In this case, the splice is done in the manual program of the splicing machine and the fibers are positioned with a lateral offset. Thus, as the electric arc discharge is mainly applied to the SMF region, it will prevent the collapse of the etched structure. Finally, the SMF region is cleaved once again, this time with a thickness on the order of ten to twenty micrometers. The thickness of the diaphragm will have a strong influence on the sensors behavior, as discussed later.
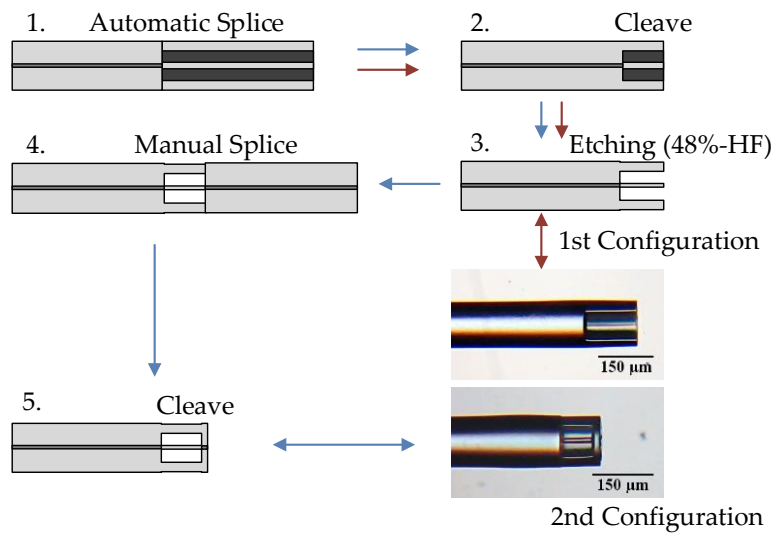
Figure 4.4 – Scheme of the optical fiber tip design fabrication steps. The red arrows indicate the steps to produce the diaphragm-free configuration and the blue ones are related to the configuration with diaphragm.

All measurements done with this configuration were performed in a reflection scheme (see Fig. 4.5). A broadband optical source, the sensing device and an optical spectrum analyzer (OSA) were connected to an optical circulator. The optical source had a bandwidth of 100 nm, centered at 1570 nm. The readings were done with a resolution of 0.1 nm.
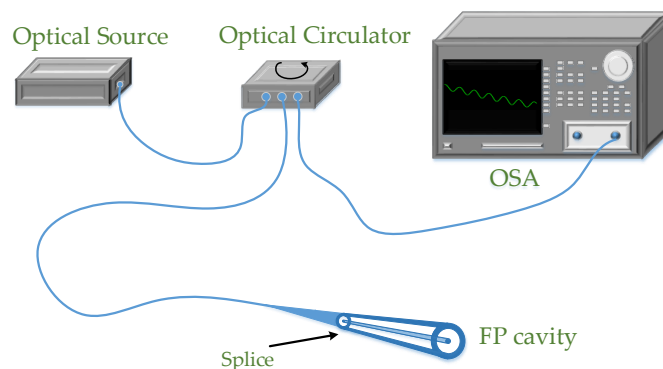
Figure 4.5 – Scheme of the experimental setup.

4.4 High Temperature Sensing Using a Diaphragm-Free Configuration

The sensing head used in this work had a length of (143 ± 5) μm and the core diameter, after etching, was (6.0 ± 0.2) μm. The scheme of the proposed sensor is shown in Fig. 4.6 (a). The first reflection (R_1) occurs at the SMF/DCF interface, whilst the second one (R_2) is originated at the DCF/air interface. The parameters α_1 and α_2 are the intensity attenuation factors at each interface, being equal to 1 if there is no transmission loss, and it is 0 if no light is transmitted. Besides, these factors should, in principle, depend on the operation wavelength. Since most of the transmission occurs essentially from the SMF section to the DCF fiber, the parameter α_2 is considered to be negligible. A sample, shown in Fig. 4.6 (b), was illuminated with a He-Ne laser and the two reflection interfaces of this FP cavity can be distinguished.
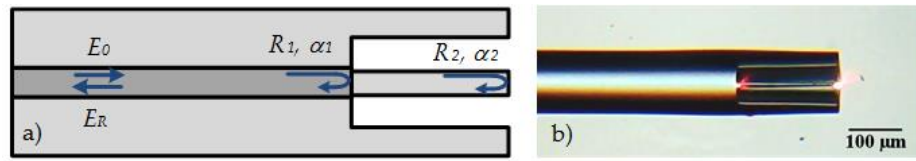
Figure 4.6 – (a) Scheme of the FP cavity for high temperature measurement and (b) photograph of the sensing head when illuminated with a He-Ne laser.

The response of this two-wave interferometer was simulated using a simple model based on [138], taking into consideration that there are only two reflective interfaces. The reflection coefficients of this cavity are given by

$$R_1 = \left(\frac{n_{SMF} - n_{DCF}}{n_{SMF} + n_{DCF}} \right)^2 \quad , \quad R_2 = \left(\frac{n_{DCF} - n_{air}}{n_{DCF} + n_{air}} \right)^2 , \tag{4.3}$$

where n_{SMF}, n_{DCF} and n_{air} are the refractive indices associated with the propagating waves on each medium. The refractive index of SMF was considered to be 1.4504 at 1550 nm. The refractive index of the DCF, estimated to be 1.3259, was determined through the experimental spectrum, according to

$$n_{DCF} = \frac{\lambda_1 \lambda_2}{2 L_{FP} \left(\lambda_2 - \lambda_1 \right)} . \tag{4.4}$$

In this equation, λ_1 and λ_2 are the wavelengths of two adjacent spectral maxima and L_{FP} is the cavity length. The round-trip propagation phase shift is given by

$$\Phi = \frac{4\pi n_{DCF} L_{FP}}{\lambda}.$$ (4.5)

Considering that there is a high transmission loss due to the mode mismatch between the two fibers, which translates into an estimated transmission coefficient $\alpha_1 = 0.01$, the total reflected electric field, resulting from the superposition of the reflected fields from the two interfaces, can be determined by

$$E_r = E_0 \left(\sqrt{R_1} + \alpha_1 \left(1 - R_1\right) \sqrt{R_2} e^{-j\Phi} \right).$$ (4.6)

The normalized total reflective intensity, I_{Rtotal}, is given by Eq. 4.7:

$$I_{Rtotal} = \left| \frac{E_r}{E_0} \right|^2 = \left(\sqrt{R_1} + \alpha_1 \left(1 - R_1\right) \sqrt{R_2} e^{-j\Phi} \right) \left(\sqrt{R_1} + \alpha_1 \left(1 - R_1\right) \sqrt{R_2} e^{-j\Phi} \right)^*.$$ (4.7)

After some straightforward algebraic manipulation, the following expression is attained:

$$I_{Rtotal} = R_1 + \alpha_1^2 \left(1 - R_1\right)^2 R_2 + 2\sqrt{R_1 R_2} \, \alpha_1 \left(1 - R_1\right) \cos(\Phi).$$ (4.8)

The total optical power calculated through this theoretical model is shown in Fig. 4.7. (green dashed line) along with the experimental spectrum (black line). Notice that an exponential term was introduced in the simulations to take into account the losses of the cavity with the wavelength. The values considered for R_1, R_2 and α_1 were, respectively, 0.002, 0.020 and 0.01. The difference observed in the visibility of the spectra is related to the fact that the coherence effects were not taken into account in the simulation. In this case, the geometric path imbalance of the cavity is 2 × 143 µm, which is higher than the coherence length of the optical source.

The sensing head was placed inside a tubular oven which can operate at temperatures up to 1000 °C, with a resolution of 0.1 °C. Starting from 150 °C until 900 °C, the temperature was slowly increased in steps of 50 °C. The wavelength shift of the FP cavity was measured at each temperature step. Figure 4.8 shows the sensor response to this parameter.
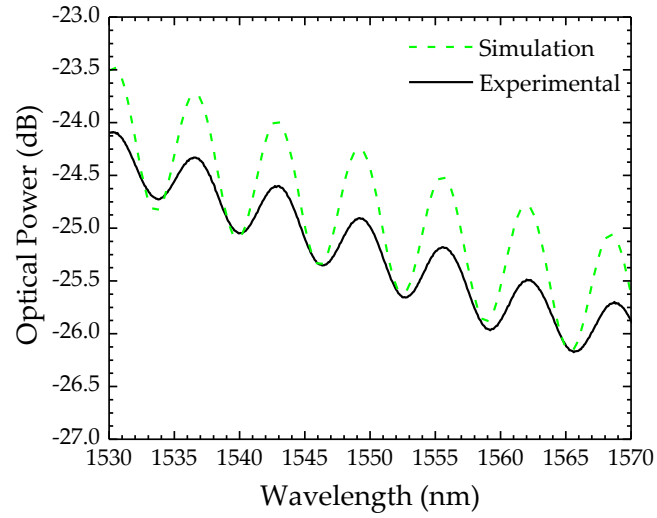
Figure 4.7 – Experimental (black line) and theoretical (green dashed line) spectra of the sensing head reflection response.

The behavior was successfully adjusted to the second order polynomial

$$\lambda = \left(2.9 \pm 0.1\right) \times 10^{-6} T^2 + \left(11.7 \pm 0.1\right) \times 10^{-3} T + \left(1550.5 \pm 0.1\right), \qquad (4.9)$$

where the wavelength, λ, comes in nm and the temperature, T, is in °C. Considering a linear function, the coefficient of determination decreases slightly (from 0.9999 to 0.9984) but it is still close to the unity. In such case, a linear sensitivity of (14.6 ± 0.2) pm/°C was estimated. The high sensitivity to temperature results from the combination between the variation of the FP cavity length, due to the silica thermal expansion, and the effective refractive index variation, due to the silica thermo-optic effect.
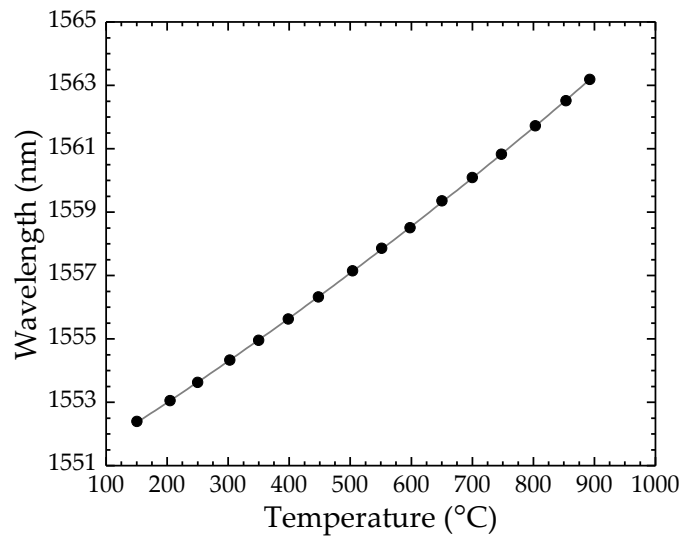
Figure 4.8 – Wavelength dependence on temperature.

4.5   Optical Phase Refractometer

Using the second configuration presented in Fig. 4.4, the core of the DCF is no longer directly exposed to the external medium, which translates into a more robust cavity. The reflections that can occur in the structure are shown in the scheme of Fig. 4.9. Thus, in this situation, the interferometric behavior will be associated with the interference of three waves: one at the SMF/DCF interface (E_1), due to the mismatch between the effective refractive indices on each side; the second one, caused by the same effect, will occur at the DCF/SMF interface (E_2); finally, E_3 corresponds to the reflection occurring at the SMF diaphragm/external medium interface. The first two waves do not change their amplitudes or their phases with the external medium index. However, E_3 presents an amplitude that depends on the refractive index of the external medium.
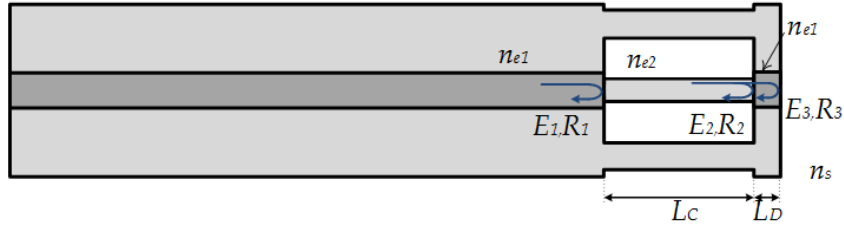
Figure 4.9 – FP microcavity evidencing the interface reflections.

Considering that E_1 has a phase ϕ_1 when generated at the interface, the phase difference with E_2 is

$$\phi_2 = \phi_1 + \frac{4\pi n_{e2} L_C}{\lambda},$$ (4.10)

where n_{e2} is the effective refractive index inside the DCF cavity, L_C corresponds to the cavity length and λ is the wavelength. Similarly, the phase difference between the waves E_3 and E_2 is

$$\phi_3 = \phi_2 + \frac{4\pi n_{e1} L_D}{\lambda},$$ (4.11)

where L_D is the diaphragm length and n_{e1} is the SMF effective refractive index. This reflection at the external interface, of ~4% when the surrounding medium is air, is substantially stronger than the second one, so the interferometric behavior in this case is

essentially determined by E_1 and E_3. However, when the sensing head is submerged in water, due to the smaller refractive index difference between the silica and the surrounding medium, there is a considerable reduction of the amplitude of E_3. Thus, both E_2 and E_3 contribute substantially to the interference, generating a superposition wave that depends on the relative phases of the two primary waves as well as on their relative amplitudes. This interference can be described through

$$E_2 + E_3 = E_{02} \sin\left(\omega t + \phi_2\right) + E_{03} \sin\left(\omega t + \phi_3\right) = E_{023} \sin\left(\omega t + \phi_{23}\right), \tag{4.12}$$

where E_{02} and E_{03} correspond to the amplitudes of the waves E_2 and E_3, respectively, and can be determined through the expressions:

$$E_{02} = E_0\left(1 - R_1\right)\sqrt{R_2}, \tag{4.13}$$

$$E_{03} = E_0\left(1 - R_1\right)\left(1 - R_2\right)\sqrt{R_3}. \tag{4.14}$$

For the simulation purposes, the transmission losses were not taken into account. The reflection coefficients at each interface, R_1, R_2 and R_3, are given by:

$$R_1 = R_2 = \left(\frac{n_{e1} - n_{e2}}{n_{e1} + n_{e2}}\right)^2 \;,\quad R_3 = \left(\frac{n_{e1} - n_S}{n_{e1} + n_S}\right)^2 , \tag{4.15}$$

where n_S is the refractive index of the surrounding medium. Using a complex notation, Eq. 4.12 comes

$$E_{23} = E_{02}\, e^{j(\omega t + \phi_2)} + E_{03}\, e^{j(\omega t + \phi_3)} = E_{023}\, e^{j(\omega t + \phi_{23})} \tag{4.16}$$

$$\Leftrightarrow E_{02}\, e^{j\phi_2} + E_{03}\, e^{j\phi_3} = E_{023}\, e^{j\phi_{23}}. \tag{4.17}$$

The amplitude E_{023} is obtained through

$$E_{023}^2 = \left(E_{023}\, e^{j\phi_{23}}\right)\left(E_{023}\, e^{j\phi_{23}}\right)^*. \tag{4.18}$$

Substituting Eq. 4.17 in the Eq. 4.18 and re-arranging, one gets:

$$E_{023}^2 = E_{02}^2 + E_{03}^2 + E_{02}\, E_{03}\left(e^{j(\phi_2 - \phi_3)} + e^{-j(\phi_2 - \phi_3)}\right). \tag{4.19}$$

Then:

$$E_{023} = \left[E_{02}^2 + E_{03}^2 + 2E_{02}\,E_{03}\cos\left(\phi_2 - \phi_3\right) \right]^{1/2}. \tag{4.20}$$

In order to determine the phase, ϕ_{23}, and using Eq. 4.17, E_{023} can be separated in the real and imaginary parts as follows:

$$E_{023}\cos\left(\phi_{23}\right) = E_{02}\cos\left(\phi_2\right) + E_{03}\cos\left(\phi_3\right),$$

$$E_{023}\sin\left(\phi_{23}\right) = E_{02}\sin\left(\phi_2\right) + E_{03}\sin\left(\phi_3\right). \tag{4.21}$$

Dividing the two equations, the following expression is achieved:

$$\phi_{23} = \arctan\left(\frac{E_{02}\sin\left(\phi_2\right) + E_{03}\sin\left(\phi_3\right)}{E_{02}\cos\left(\phi_2\right) + E_{03}\cos\left(\phi_3\right)} \right). \tag{4.22}$$

A schematic diagram is shown in Fig. 4.10 that illustrates the dependence of the phase of the resultant wave on the amplitude of each wave individually. In this diagram E_2 is kept constant both in phase and amplitude, whereas E_3 presents the same phase but different amplitudes. It is quite clear that there is a modification on the interferometric wave, both in amplitude and phase, when the amplitude of E_3 is reduced.
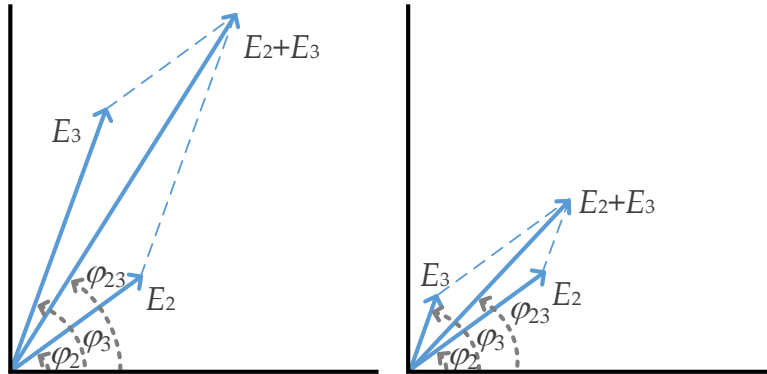
Figure 4.10 – Scheme of the resultant wave phase variation with the amplitude of E_3; E_2 remains constant.

The simulation of the interference between the waves E_2 and E_3 was further investigated taking the previous equations into account. The resultant interferometric data is shown in Fig. 4.11. In the simulations, a cavity length of 90 μm and a diaphragm thickness of 12 μm were considered. Besides, the effective refractive indices were set $n_{e1} \approx 1.45$, $n_{e2} \approx 1.41$ and $n_s = 1.00$ or $n_s = 1.32$, for air and water as the surrounding medium. Regarding the reflection coefficients, R_2 was considered to be 0.0020 and R_3 was 0.0338 or

0.0023, when the surrounding medium was air and water, respectively. In addition to the clear variation in amplitude, the inset in Fig. 4.11 shows the shift that occurs when the external medium changes from air to water.
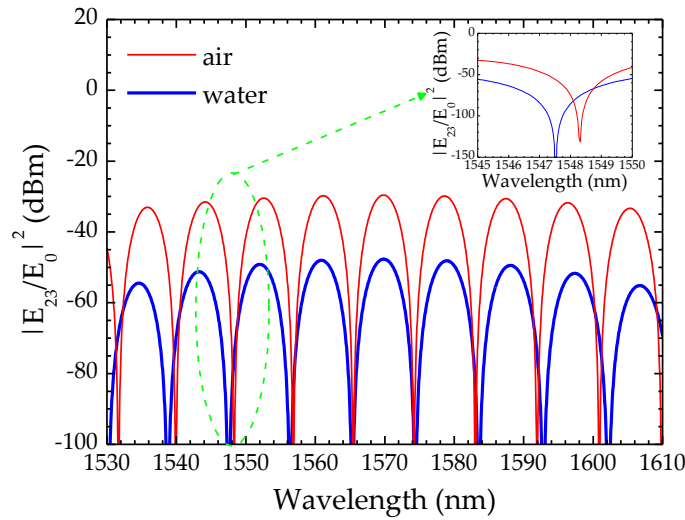
Figure 4.11 – Simulated spectra of the FP micro-cavity in different media. The inset shows the phase variation of the spectrum.

If the liquid medium is subjected to temperature variations, its refractive index will also change. This variation originates a change of the silica-water reflectivity coefficient and a shift in the E_{23} wave phase is to be expected. The phase of the resulting interference between this wave and E_1 will also be affected by the variation of the water refractive index. Therefore, with this configuration, the principle of the amplitude-phase conversion is achieved in the optical domain, *i.e.*, the phase of the net interferometric optical signal becomes a function of the amplitude of one of the interfering waves (E_3 in this case).

4.5.1   *Water Temperature and Refractive Index Relationship*

The relationship between the refractive index of water and its temperature has been described in several works [227-230]. However, the water refractive index depends not only on the temperature, but also on other parameters, such as the density and the operation wavelength [230]. Tables were found in the literature for three different wavelengths: 430, 600 and 660 nm. The wavelength dependence can be described by the Sellmeier equation,

$$n(\lambda) = A + \frac{B}{\lambda^2} + \frac{C}{\lambda^4} + ..., \tag{4.23}$$

where only the first three terms were taken into account. A tendency curve was adjusted for the three wavelengths, and the parameters A, B and C were estimated. Using these values, it is possible to determine the refractive index of water at 1550 nm. This procedure was done for temperatures ranging from 10 °C to 80 °C, in steps of 10 °C, considering the values presented in [230]. This information is gathered in Fig. 4.12 (a). Notice that there is a different tendency curve for each temperature.
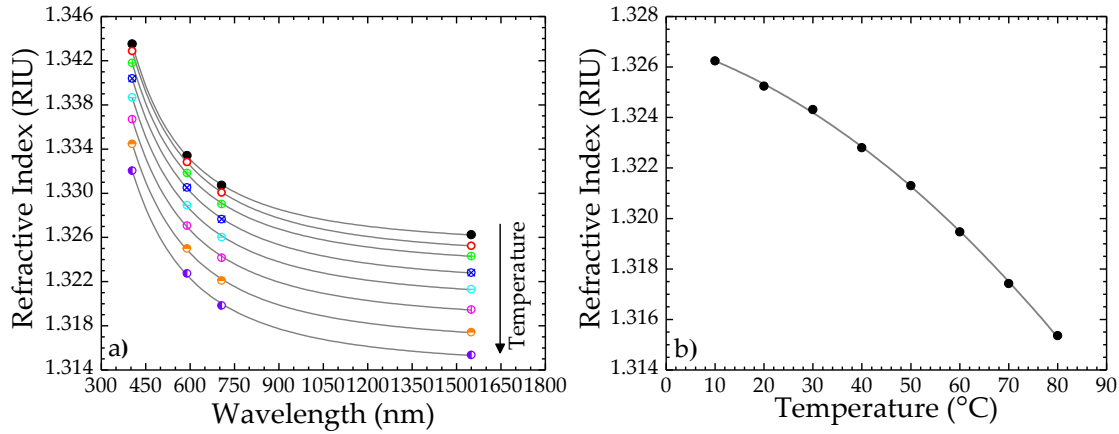
Figure 4.12 – (a) Dependence of the refractive index of water on the operation wavelength for different temperatures and (b) refractive index of water as a function of temperature, for a wavelength of 1550 nm.

Figure 4.12 (b) shows the relationship between the water refractive index and the temperature, for an operation wavelength of 1550 nm. The refractive index diminishes as temperature increases, and the data can be well adjusted to the second order polynomial:

$$n(T) = -1.073 \times 10^{-6} T^2 - 5.982 \times 10^{-5} T + 1.327. \tag{4.24}$$

By converting the water temperature change into its refractive index variation, it is possible to infer the sensing head response towards this parameter. This approach is only valid when the device under study exhibits a response where the different contributions to its sensitivity can be discriminated.

4.5.2 Experimental Results

The experimental reflection spectra of two different cavities are shown in Fig. 4.13, for two different external media. The first cavity had a length of (80 ± 3) μm and a

(13 ± 3) μm thick diaphragm. Regarding the second sensor, it presented a FP cavity length of (95 ± 3) μm and a diaphragm with a thickness of (43 ± 3) μm.   This data is in good agreement with the simulation results presented in Fig. 4.11. When the sensor is placed in water, there is an increase in the losses and the visibility diminishes. This behavior is highly dependent on the diaphragm thickness. If the thickness of the diaphragm is larger than 40 μm, there is an increase of the losses, but the visibility remains nearly the same, as can be seen in Fig. 4.13 (b).
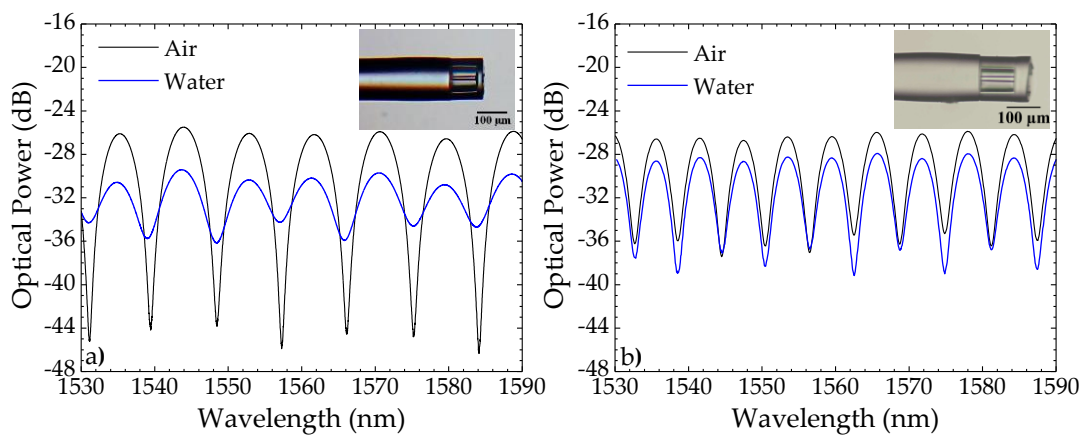
Figure 4.13 – Spectra of the FP micro-cavity when the external medium is air (black line) and water (blue line). (a) Sensor with a thin diaphragm. (b) Sensor with a thick diaphragm.

The sensing heads were subjected to temperature measurements in air and in water. In the first case, the sensor was placed inside a tubular oven and measurements were done in a range between room temperature (~23 °C) and 85 °C. Afterwards, the device was submerged in hot water (~85 °C), which was let to cool down until room temperature. In both cases, the temperature resolution was of 0.1 °C.

Regarding the response of the sensor with a thick diaphragm, shown in Fig. 4.14, it is independent of the external media. The linear sensitivities obtained were of (9.6 ± 0.1) pm/°C and (9.7 ± 0.1) pm/°C when the surrounding medium was air and water, respectively. This means independence of the sensitivity from the surrounding medium. Such result, which is also visible looking at Fig. 4.13 (b) where essentially the channeled spectrum does not depend of having either air or water outside, indicates that the amplitude of E_3 is residual in both situations. This points out to significant extra optical loss when the diaphragm thickness increases from ~13 μm to ~43 μm, probably

introduced due to a mismatch of the fabrication conditions from the established procedure.
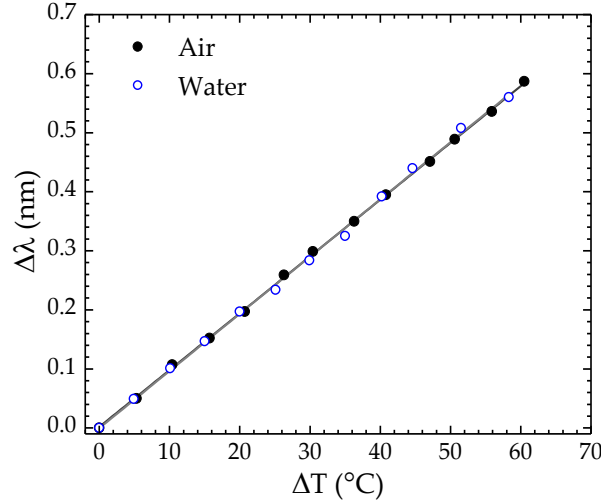
Figure 4.14 – Wavelength shift dependence of the sensor response with a diaphragm of 43 μm on the applied temperature, in two different media.

The sensing device with the thinner diaphragm (of ~13 μm) was subjected to the same external conditions, and the results are shown in Fig. 4.15 (a). The sensor response, in this case, is affected by the external medium, and its sensitivity is lower when submerged in water (blue hollow circles) than when in air (black solid circles). In the former situation, a sensitivity of (9.4 ± 0.1) pm/°C was obtained, whereas in the last one the sensitivity was of (13.5 ± 0.1) pm/°C. The difference between these values is an indication that the refractive index variation of water induced by the temperature has an impact on the sensor response.

Thus, considering that $\Delta\lambda_1$ corresponds to the wavelength shift of the cavity optical spectrum when the external medium is air, we can write

$$\Delta\lambda_1 = k_{T1}\Delta T, \tag{4.25}$$

where k_{T1} stands for the temperature sensitivity. If, on the other hand, the external medium is water, the wavelength shift can be separated into two different components: one related to the diaphragm silica thermal expansion (k_{T1}), which was previously measured in air, and the other attributed to the water refractive index variation (k_{T2}).

Therefore, the wavelength shift measured in this situation is related to temperature according to the expression

$$\Delta\lambda_2 = \left(k_{T1} + k_{T2}\right)\Delta T. \tag{4.26}$$

Subtracting Eq. 4.26 and Eq. 4.25, the following relationship is attained:

$$\Delta\lambda_2 - \Delta\lambda_1 = k_{T2}\Delta T. \tag{4.27}$$

The calculated wavelength shift due to the water contribution is shown in Fig. 4.15 (b). In this case the sensitivity is negative, with a value of (-5.8 ± 0.2) pm/°C.
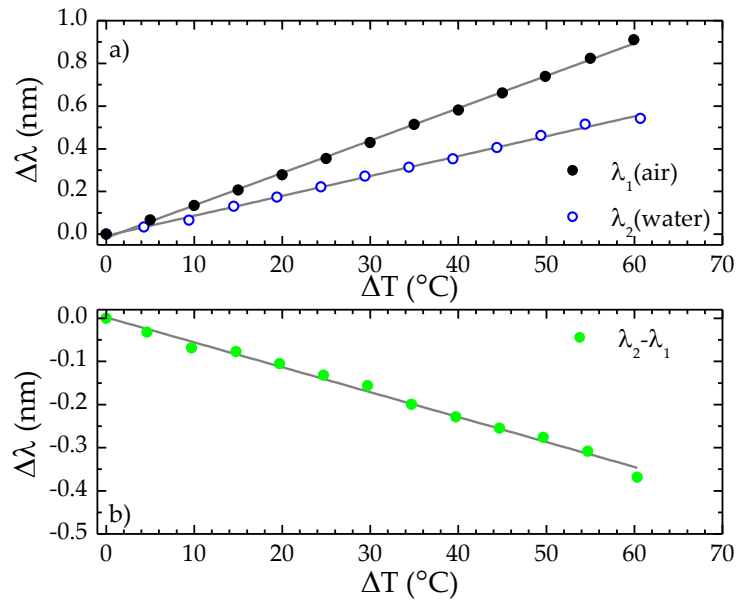
Figure 4.15 – Wavelength shift dependence on temperature: (a) sensing head exposed to air (black circles) and when immersed in water (blue circles) and (b) calculated water contribution.

The sensing head response to the variation of the external medium refractive index can be estimated by applying the relationship between the water refractive index and the temperature, which was described in Section 4.5.1. By diminishing temperature, the refractive index increases, and with it, there is a wavelength shift of the interferometric cavity towards red, as can be seen in Fig. 4.16. This variation was adjusted to the following second order polynomial,

$$\lambda(n) = \left(1758.7 \pm 560.7\right)n^2 - \left(4608.8 \pm 1484.1\right)n + \left(3018.9 \pm 982.0\right), \tag{4.28}$$

where the wavelength, λ, is in nm, and n corresponds to the refractive index, and comes in RIU. It is possible to extrapolate two different linear regions from Fig. 4.16, one for

lower refractive indices, between 1.319 RIU and 1.324 RIU, and another for higher refractive indices, from 1.325 RIU to 1.327 RIU. A sensitivity of (38.7 ± 2.5) nm/RIU was attained for the former, whilst a sensitivity of (56.7 ± 4.2) nm/RIU was obtained for the last region. Although the sensitivities obtained are lower than the ones reported in the literature, with this configuration there is no fiber core exposition to the external medium. It is only the interaction between the reflection of the third wave at the end of the fiber tip and the environment that ensures the spectrum variation.
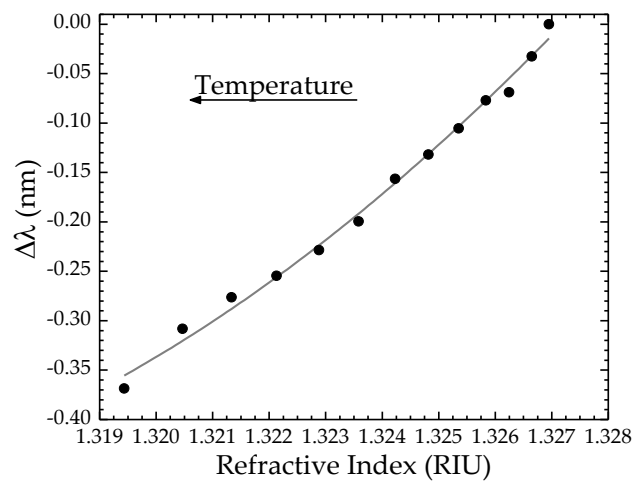
Figure 4.16 – Wavelength shift variation with the water refractive index.

Besides the variation in the spectrum with the water temperature, a change in the visibility of the spectrum was also noticed. This is also an effect of the variation of the refractive index of water, as already mentioned. Therefore, a different kind of analysis could also have been done with this sensing head, in complement to the approach described above.

4.6   Final Remarks

In this Chapter, two different sensing configurations were proposed based on post-processing of a double clad optical fiber. The fiber did not guide light in its core, due to the higher refractive index in the P-doped inner cladding. However, after applying wet chemical etching, this layer was removed and light started to propagate in the core. In the first configuration, the micro-cavity was only constituted by a short section of such

etched fiber spliced to a SMF. The device was successfully tested to extreme temperatures and revealed to be more sensitive than more conventional fiber structures, such as the fiber Bragg grating (FBG) [231] or the hollow core silica tube [122]. In the first case, the structure was ~1.1 times more sensitive than the FBG, whereas in the last, the sensitivity was ~2 times higher. However, when the structure is placed in a liquid medium, this liquid will surround the suspended core, causing instability in the spectral response. A different configuration was then developed. In this case, a thin diaphragm was applied to the first structure by fusion splicing. This translated into a more stable device that presented different responses to temperature when the external medium was air or water. This behavior was due to the fact that the sensing head was measuring, besides the silica thermal expansion, the water refractive index variation with temperature. Thus, this sensor is an interesting design to be used in aqueous environments, namely, in biochemistry. Furthermore, if used in a multiplexed configuration, it can allow temperature compensation or even measurement of different parameters.

CHAPTER FIVE

Sensing Structures Incorporated in Optical Fibers
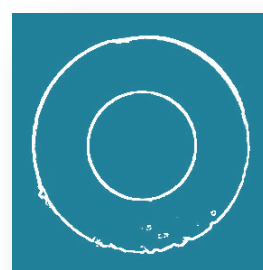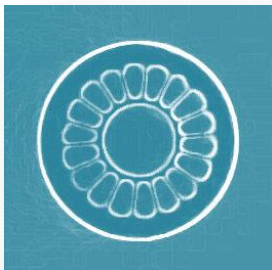
5.1 Introduction

The measurement of strain and temperature using fiber optic-based configurations has been a subject of extensive research since the first steps in the field were taken. With the rapid technological evolution occurring currently in our society, the industry seeks sensors easy to manufacture, to implement and to control. The lifespan must be high; the devices have to be reliable, stable and highly sensitive. There are already commercial solutions based on fiber optic sensors, such as the fiber Bragg grating (FBG). However, there is still room for research, exploiting different configurations or trying to achieve even better sensitivities and resolutions.

Intrinsic Fabry-Perot (FP) cavities formed between two sections of fiber present low sensitivity to temperature, being a good alternative for the measurement of strain without the need to compensate the temperature effects. The structures can be formed by splicing a short section of hollow core photonic crystal fiber (PCF) [85] or a chemically etched multimode fiber section [135] between two sections of single mode fiber (SMF). Another possibility is to form an air cavity, like a bubble or a spheroidal cavity, inside the fiber. There are different ways to fabricate the structures through splicing. For example, the splice of two sections of SMF [130, 150], SMF spliced to index guiding PCF [101] or splicing a flat and hemispherical tip of SMF [132]. The sensors proposed in these works were characterized to strain and temperature separately.

Even though there are several reported works concerning strain and temperature measurements, such as the ones previously mentioned, the measurement of strain at high temperatures has not been fully explored, in particular, when temperatures exceed 750 °C. Ran *et al.* proposed the use of a FP cavity to measure strain at temperatures as high as 800 °C [84]. The cavity was created using 157 nm laser micromachining. The fabrication of an air bubble cavity by splicing a multimode PCF to a SMF has also been proposed [121]. In this case, the FP cavity was subjected to strain measurements up to 1850 $\mu\varepsilon$, at temperatures between 100 °C and 750 °C. Rao *et al.* reported on the annealing behaviors of a long period grating fabricated in a PCF using a high-frequency CO_2 laser [232]. The sensor was tested in strain at temperatures as high as 650 °C.

In its turn, the FBG is probably one of the most popular structures for monitoring strain and/or temperature, both in academic research and in industrial applications. The most common fabrication technique is based on UV-laser irradiation and relies on the photosensitivity of the fiber to produce the periodic index modulation [233]. However, these devices present poor stability for temperatures above 500 °C, being completely erased at 700 °C [234]. In 2004, Martinez *et al.* reported a method for direct writing of FBGs, using a point-by-point femtosecond laser technique [235]. With this method the change in the refractive index is produced locally and there is no need for phase-masks or even photosensitive fibers. Besides, these structures exhibit an excellent stability above 1000 °C [234].

In this Chapter, the measurement of strain is addressed from two different perspectives. The first is relative to the control of the sensitivity of a FP sensor structure, simply by varying the cavity length. The second perspective is related to the measurement of strain at high temperatures, considering the response of a sensor based on a FP cavity and the response of a FBG. In this case, both are subjected to strain at different temperatures, which can be as high as 900 °C and the influence of thermal annealing is also addressed, to stabilize the sensor response and improve its performance at high temperatures. These types of measurements can be used in the monitoring of crack development or propagation in the civil engineering field, or in advanced turbine engines or even space plane engines, among other situations where high temperatures are involved and strain or stress needs to be monitored [233, 236].

5.2 Controlling the Sensitivity of a Fabry-Perot Strain Sensor

In this Section, a Fabry-Perot (FP) strain sensor is described. The sensing element is based on a small section of hollow core ring photonic crystal fiber (HCR-PCF). The ability to manufacture samples with short lengths enables the control of the strain sensitivity, which can be more than 15 times the strain sensitivity of a fiber Bragg grating (~1.2 pm/$\mu\varepsilon$ at 1550 nm [231]).

5.2.1 Sensor Design and Spectral Characteristics

The HCR-PCF used to create the FP cavity, and whose cross-section is shown in Fig. 5.1 (a), is the same as the one described in Section 3.4. The cavity was obtained by fusion splicing a section of this fiber between two single mode fibers (SMFs), following the procedures described in Section 3.3.1. The microscope photograph of one of the samples characterized in this work is shown in Fig. 5.1 (b).

a) 50 μm   b) 100 μm
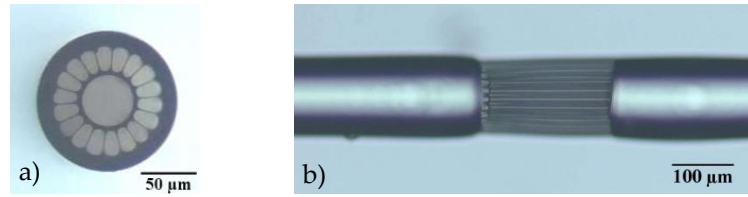
Figure 5.1 – Microscope images of (a) the HCR-PCF cross-section and (b) the 207 μm long sample.

The scheme of the experimental setup is shown in Fig. 5.2. It was constituted by a broadband optical source, with a bandwidth of 100 nm and centered at 1570 nm, an optical spectrum analyzer (OSA), with a resolution of 0.1 nm and an optical circulator.

Optical Source   Optical Circulator

OSA

FP cavity

Splices
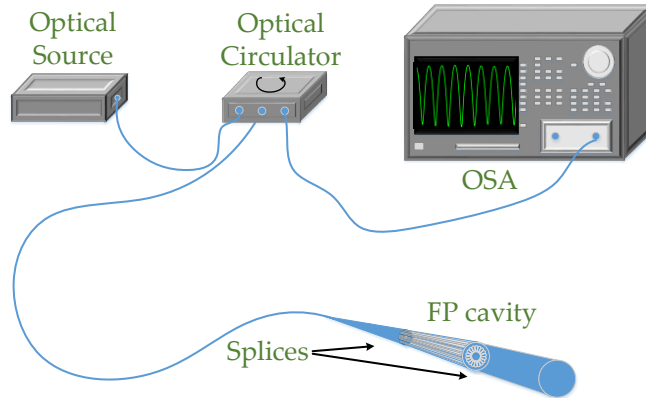
Figure 5.2 – Scheme of the experimental setup. OSA stands for optical spectrum analyzer and FP cavity corresponds to the Fabry-Perot cavity.

Four different devices, with different FP cavity lengths, were fabricated and characterized in strain. The spectral behavior of each sample, shown in Fig. 5.3, is similar to a two-wave interferometer. The period of the FP fringes, $\Delta\lambda$, depends on the FP cavity length (L_{FP}) according to $\Delta\lambda = \lambda_1\lambda_2/2n_{eff}L_{FP}$, where λ_1 and λ_2 are the wavelengths of two adjacent fringes and n_{eff} is the effective refractive index of the fundamental mode propagating in the HCR-PCF. The average refractive index was estimated to be (1.02 ± 0.01) RIU for an operation wavelength of 1550 nm, which means that most of light travels inside the hollow core. The interferometric period was estimated to be

(35.3 ± 0.1) nm, (6.0 ± 0.1) nm and (1.3 ± 0.1) nm for the (35 ± 2) μm, (207 ± 2) μm and (906 ± 5) μm long FP cavities, respectively. The smaller FP cavity, which had a length of (13 ± 2) μm, only presents one interference peak in the spectral range considered, thus it was not possible to estimate the interferometric period from the spectral response in Fig. 5.3.
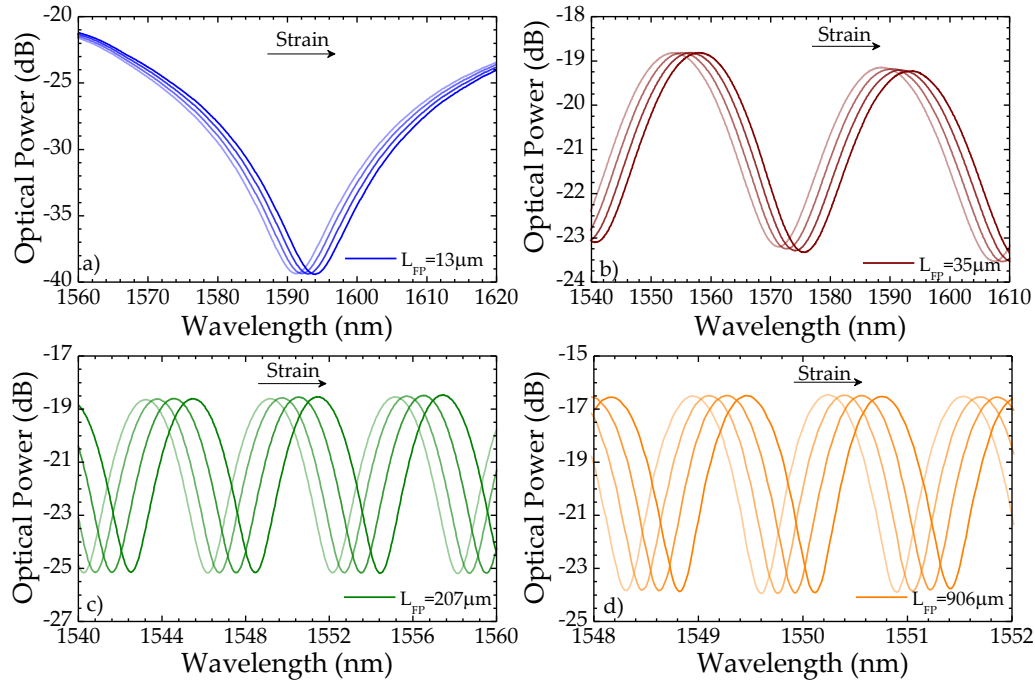
Figure 5.3 – Spectra of the four samples, with different FP cavity lengths. The spectrum shift with the applied strain is also shown for each sample.

5.2.2 Experimental Results

The devices were characterized in strain, at room temperature, being under the same test conditions. Thus, the fiber was attached to a translation stage with a resolution of 0.01 mm. The total length of fiber over which strain was applied, composed by the SMF sections and the HCR-PCF, was of (700 ± 5) mm. This length, defined as L_{T}, is identified in Fig. 5.4, along with the other dimensions considered in this work.
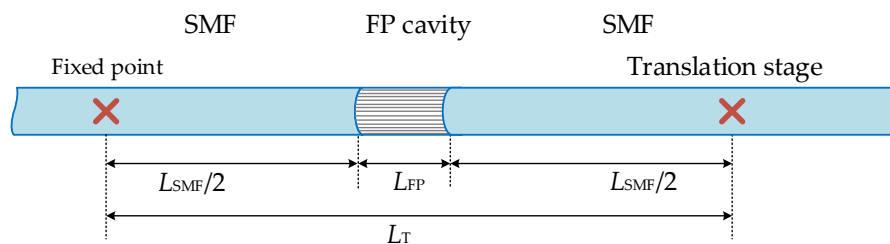
Figure 5.4 – Identification of the lengths considered in the strain analysis.

The interferometric spectrum shifts towards longer wavelengths (red shift) as strain is applied, which means that the optical path increased with strain (see Fig. 5.3). The wavelength shift dependence on strain of each sensor is shown in Fig. 5.5 (a). There is a clear influence of the FP cavity length in the sensitivity to strain. In fact, the smaller the sensing head, the higher the sensitivity. Furthermore, the response is linear in all cases. For the 906 μm long device, a sensitivity of (3.12 ± 0.01) pm/με was attained, whereas for the 207 μm long sample, the sensitivity was of (3.79 ± 0.01) pm/με. Decreasing the length to 35 μm translated into a sensor with a doubled sensitivity, of (6.16 ± 0.01) pm/με. Decreasing the length furthermore, to 13 μm, resulted in a sensitivity of (15.43 ± 0.01) pm/με. This means that by choosing the appropriate FP cavity length, it is possible to tailor the sensitivity most suitable for the desired application. Figure 5.5 (b) presents the estimated sensitivities as a function of the FP cavity length along with the tendency curve. The non-linear behavior shows the rapid increase of the sensitivity for smaller FP cavities, following the same tendency as observed in other configurations [237].
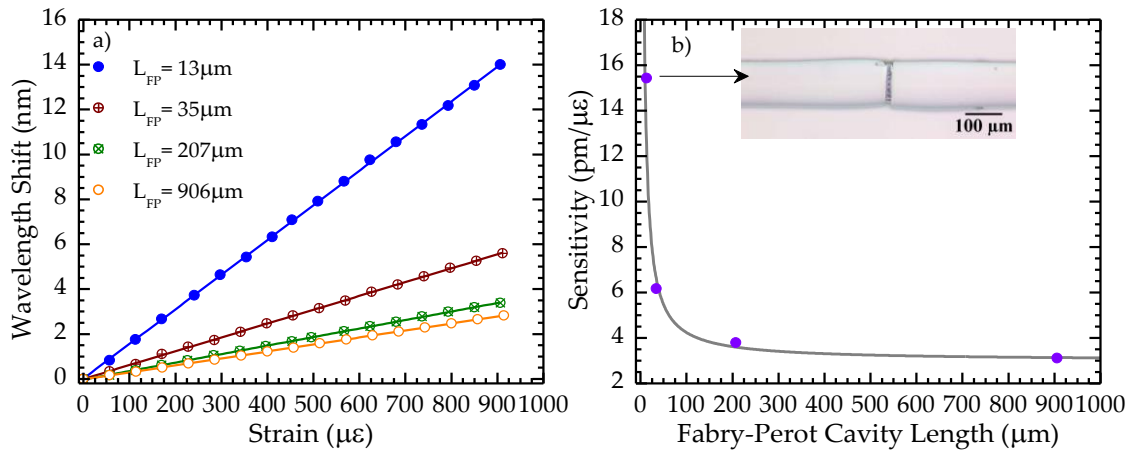
Figure 5.5 – (a) Sensors response to the applied strain. (b) Sensitivity dependence on the FP cavity length. Inset: microscope photograph of the 13 μm long sensing head.

Further investigations were carried out to understand the influence of the total length over which strain was applied (L_T). The FP cavity with a length of 207 μm was subjected to strain, considering three different total gauge lengths: of 706 mm, 342 mm and 170 mm. The behavior, shown in Fig. 5.6 (a), is linear in all situations and the sensitivities are quite close to each other: (3.79 ± 0.01) pm/με, (3.75 ± 0.01) pm/ με and (3.67 ± 0.01) pm/ με, for the gauge length of (706 ± 5) mm, (342 ± 5) mm and (170 ± 5) mm,

respectively. Figure 5.6 (b) shows the strain sensitivity as a function of the total gauge length, where it is explicit that as the total length increases, the sensitivity is enhanced. However, the variation is of only 0.12 pm/με for a total length increase of ~540 mm. Thus, even though there is an improvement in the sensitivity, this is not the dominant parameter for this matter.
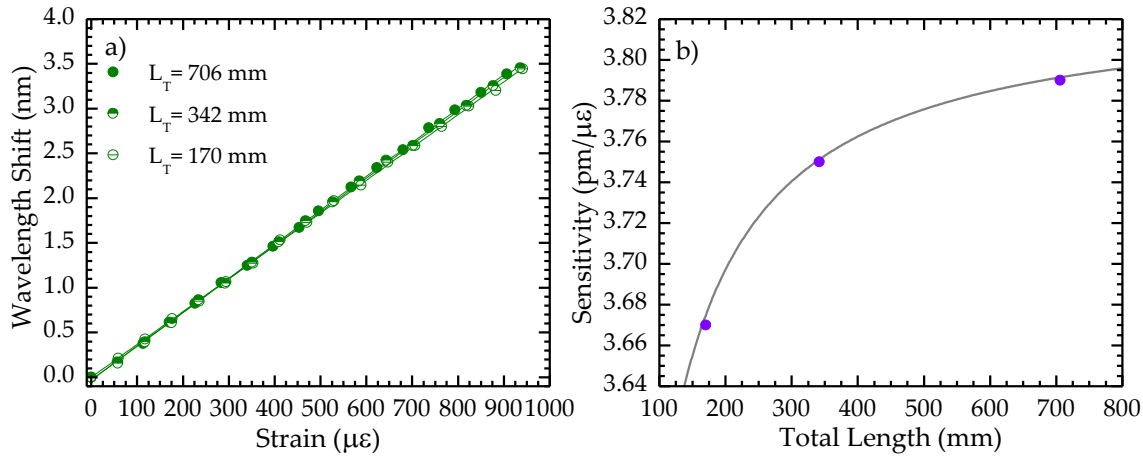
Figure 5.6 - (a) Response of the 207 μm long sensor cavity to strain, considering three different gauge lengths. (b) Sensitivity dependence on the gauge length (purple dots) and tendency curve (gray line).

The temperature response of the proposed sensor was analyzed by placing the same sample inside a tubular oven. The temperature was changed from room temperature to 85 °C, with a resolution of 0.1 °C. The wavelength dependence towards this parameter is shown in Fig. 5.7.
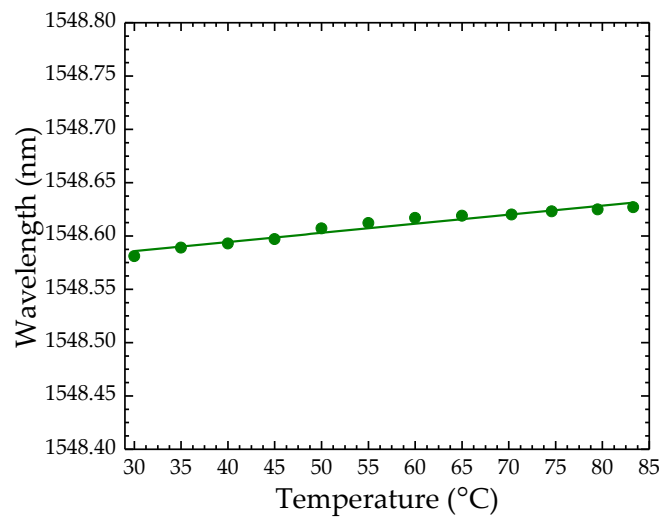
Figure 5.7 – Wavelength dependence on temperature for the 207 μm long sensing head.

The sensitivity attained was of only (0.85 ± 0.06) pm/°C. This indicates that, in most situations, the sensing device can be used to perform strain measurements without requiring temperature compensation, since the cross-sensitivity is of only 0.21 με/°C [32].

5.3 Measuring Strain at High Temperatures (Part I): Silica Tube

This Section describes the characterization of a Fabry-Perot cavity based on a silica tube with a special design. Strain measurements are performed at different temperatures, which can be as high as 900 °C. The annealing effects are also addressed.

5.3.1 Sensor Design and Spectral Characteristics

The silica tube used in this work was fabricated at the IPHT-Jena. All components of the silica tube were manufactured from high purity silica Heraeus Suprasil® F300. Four rods, with a diameter of 1.2 mm were placed inside the cladding tube, which had an inner diameter of 4 mm and an outer diameter of 6 mm, in exact orthogonal positions, and were sintered using the modified chemical vapor deposition (MCVD) method. The preform was drawn to the final fiber by pressurized drawing at constant temperature. The pressure inside the preform changed from 1000 Pa to 3000 Pa above atmospheric pressure. Higher pressure translated into larger silica tube hollow core area. This effect can be seen in Fig. 5.8. The final outer diameter was of 125 μm and the silica tube was coated with a single layer of ultraviolet cured acrylate.
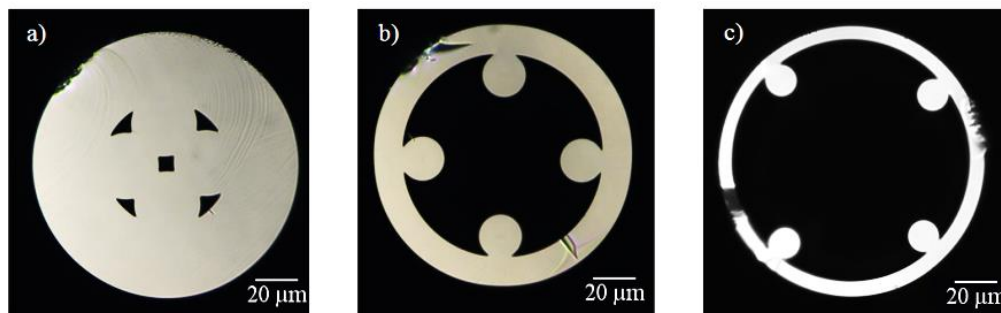
Figure 5.8 – Cross section images of the silica tube varying the pressure during fiber drawing: (a) p = 1000 Pa, (b) p = 2300 Pa and (c) p = 3000 Pa.

The silica tube shown in Fig. 5.8 (b) was selected to be used as a sensing element, in a FP configuration. It presented a cladding with a thickness of (14 ± 2) μm, a hollow core

and the four small rods presented a diameter of (20 ± 2) μm each. The presence of the four rods will have a reinforcement effect in the structure. This matter will be discussed further ahead.

The FP cavity, shown in Fig. 5.9, was obtained by fusion splicing a short section of silica tube between two sections of SMF, following the same procedures as described in Section 3.3.1. The sensor was interrogated in a reflection scheme similar to the one presented in Fig. 5.2. The OSA resolution was, in this case, of 0.02 nm.
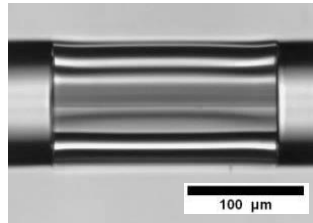
Figure 5.9 – Photograph of one FP cavity based on the new hollow core silica tube design.

Four different sensors were produced, with different cavity lengths. The spectrum of each sensor, presented in Fig. 5.10, is the result of a two wave interferometer. The mean effective refractive index was estimated to be ~1.00 RIU, meaning that almost all light travels inside the hollow core.
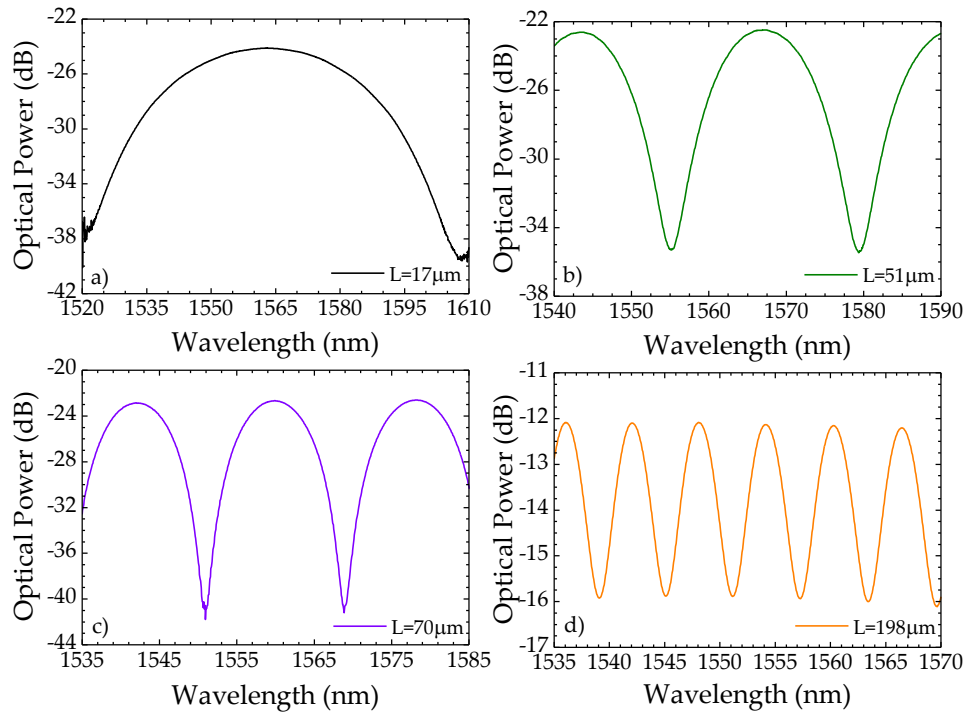
Figure 5.10 – Spectra of the four FP cavity sensors.

5.3.2   Experimental Results

In a first stage, the samples were attached to a translation stage with a resolution of 0.01 mm and strain measurements were carried out at room temperature. The total length over which strain was applied was kept constant throughout the experiments, with a value of (735 ± 5) mm. The FP cavities response towards the applied strain is linear, as shown in Fig. 5.11 (a). Besides, the sensitivity depends on the FP cavity length. Sensitivities of (13.9 ± 0.1) pm/μɛ, (6.0 ± 0.1) pm/μɛ, (4.6 ± 0.1) pm/μɛ and (3.5 ± 0.1) pm/μɛ were respectively attained for the 17 μm, 51 μm, 70 μm and 198 μm long samples, following the same trend as in the previous configuration. The cavity lengths were determined through the microscope images, with an associated uncertainty of ± 2 μm.
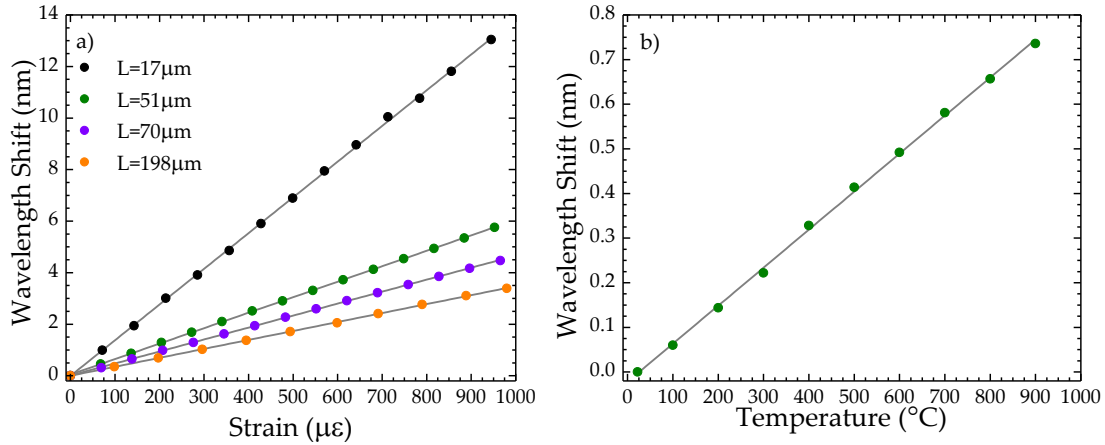
Figure 5.11 – (a) FP cavity sensors response to the applied strain. (b) Response of the 198 μm long sensor to temperature.

The 198 μm long sensor was placed inside a tubular oven, with the FP cavity placed at its center. The fiber was kept straight but loose, without any tension applied. The sensor was then subjected to a temperature variation of ~900 °C. The interferometric spectrum shifted towards longer wavelengths with the increase of temperature (red shift), as can be seen in Fig. 5.11 (b). The experimental data was well adjusted to a linear fitting and a sensitivity of (0.85 ± 0.01) pm/°C was attained, which indicates that this sensor presented a cross-sensitivity of ~0.24 μɛ/°C. Considering the round-trip propagation phase shift $\Delta\Phi = 2\pi m = 4\pi n_{eff} L_{FP}/\lambda$, where m is the interference peak order, after some straightforward algebraic manipulation, it is possible to re-write the equation as $d\lambda = 2n_{eff} dL_{FP}/m$. Combining the two equations, one gets for the thermal sensitivity of

this sensor the value of $\Delta L_{FP}\big/L_{FP} = 5.49 \times 10^{-7}\,/\,{}^{\circ}C$ (at the operation wavelength of 1547 nm), which is in good agreement with the silica thermal expansion coefficient presented in the literature, of $5.5 \times 10^{-7}\,/\,{}^{\circ}C$ [126].

Since this FP cavity presents low sensitivity to temperature, it is worthwhile to study its behavior when strain is applied under extreme temperature conditions. Thus, the 70 μm long FP cavity was placed inside the tubular oven, in a centered position, and on the outside it was fixed to a translation stage. The fiber was kept straight under a slight tension. The temperature was increased from 22 °C to 750 °C in steps of 150 °C. From 750 °C to 900 °C, the steps were of 50 °C. The resolution of the oven temperature controller was of 1 °C. At each temperature step, the setup was stable for about 30 minutes. Strain measurements were then carried out, by increasing the tension in the fiber up to 1000 με (up curves in Fig. 5.12) and decreasing it back to the initial state (down curves in Fig. 5.12).
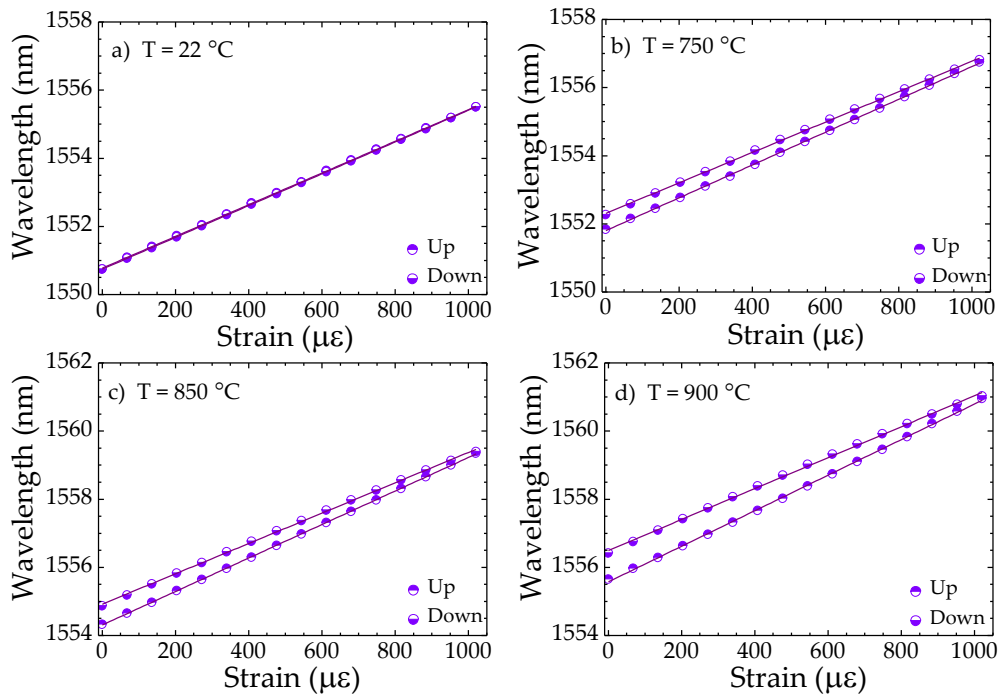
Figure 5.12 – Response of the 70 μm long FP cavity to the applied strain at different temperatures. Up and down stand for increasing and decreasing the applied strain, respectively.

Until 600 °C the behavior was nearly the same and the sensitivities obtained when increasing strain were similar as when decreasing it. However, from 750 °C on, the sensor exhibited higher sensitivity when increasing strain than when it decreased. This

fact indicates that at such high temperatures, the Young modulus of the silica tube is reduced, also associated with a certain level of induced plasticity, since the interferometric fringes did not return to the original wavelength values when strain was decreased. At 900 °C the reduction of the strain sensitivity translates into a red shift of ~1 nm.

The effects of annealing were addressed by subjecting the 51 μm long sensor to a temperature of 900 °C for 7 hours (see Fig. 5.13). In this case, the fiber was kept straight under a slight tension. The monitored fringe wavelength shifted 4.4 nm throughout this period of time. However, in the first 40 minutes the shift was more pronounced, with a shift rate of (0.10 ± 0.01) nm/min. After that time, the wavelength shift became slower and from 4 hours up to 7 hours, the change was of (3.0 ± 0.1) pm/min. The oven was then switched off and cooled down until it reached room temperature.
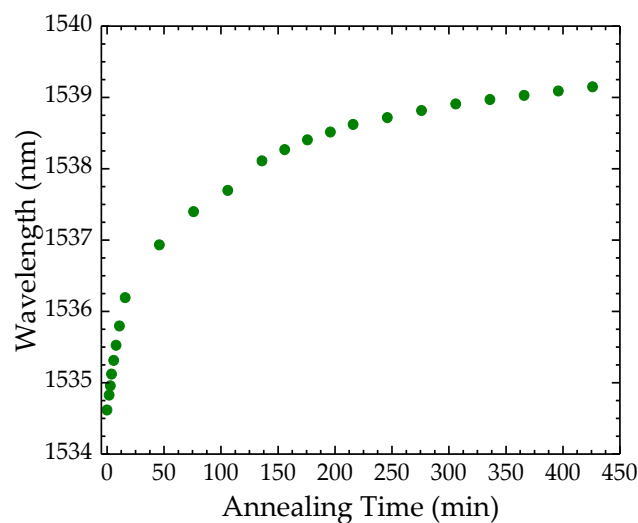
Figure 5.13 – Wavelength shift of the 51 μm long FP cavity for an annealing temperature of 900 °C.

After being subjected to the annealing at such high temperature, the sample was tested to strain at different temperatures, following the same procedure as for the 70 μm long sensor. The results, presented in Fig. 5.14, show that in this case, the difference attained in the sensitivity when increasing and decreasing strain was not as notorious as in the previous experiments. The small difference at 900 °C can be due to the fact that the annealing was not fully performed.
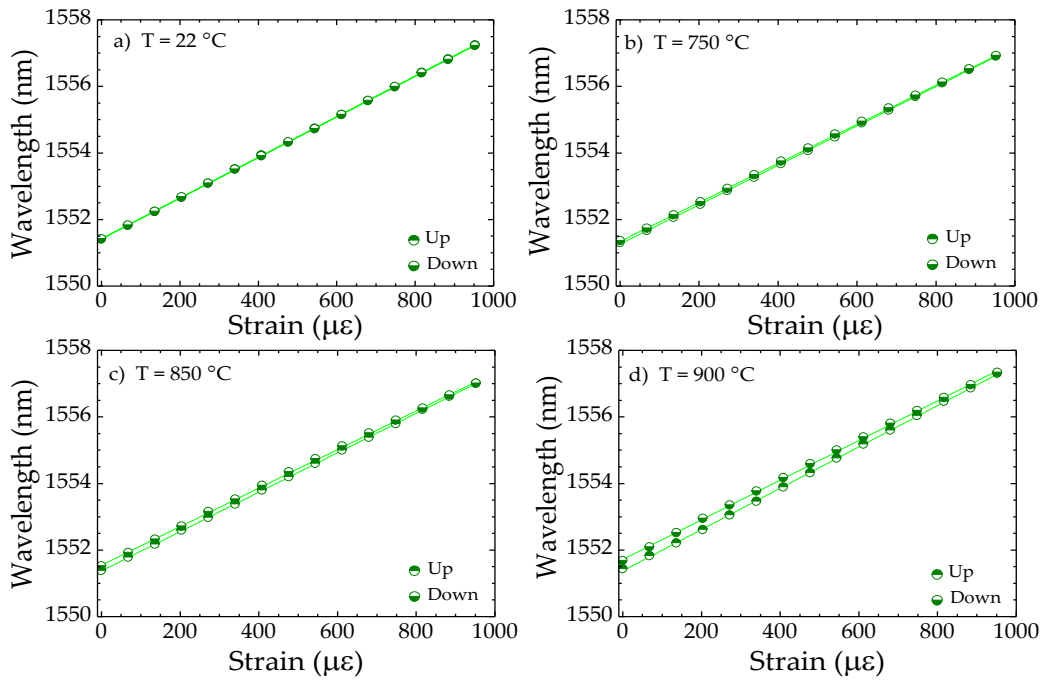
Figure 5.14 – Response of the 51 µm long FP cavity to strain at different temperatures, after 7 hours of annealing, at 900 °C. Up and down stand for increasing and decreasing the applied strain, respectively.

The sensitivities to strain at different temperatures are gathered in Fig. 5.15. In both sensors, regardless of having been annealed, the strain sensitivity decreased as temperature increased up to 600 °C, increasing once again afterwards. This effect can be attributed to two reasons: the non-linear variation of the silica thermal expansion as temperature arises [238], as well as the dependence of the photoelastic constant on temperature. The photoelastic constant is essentially determined by the Pockels coefficient, p_{12}, which exhibits a maximum at 600 °C [239], translating into a minimum in the strain sensitivity. Nevertheless, the difference between applying strain and reducing it is much more significant when no annealing occurred.
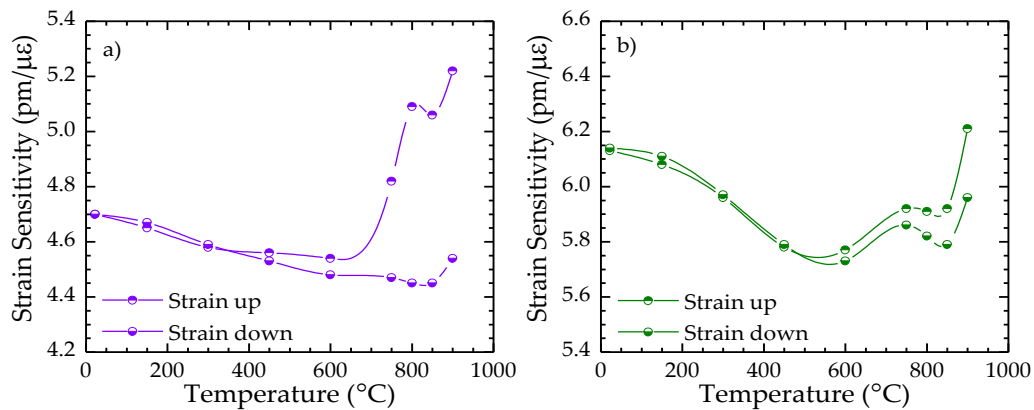
Figure 5.15 – Dependence of the strain sensitivity at different temperatures: (a) without annealing and (b) with annealing.

The mechanical stability of this new silica tube design was compared to the one of a conventional silica tube by applying strain until rupture. Both cavities were fabricated under the same conditions. The conventional silica tube, whose cross-section is shown on the inset of Fig. 5.16, had a hollow core diameter of (57 ± 2) μm, and a total cross-section area of ~2550 μm². Regarding the new design, with the four rods, its hollow cross-section area was of ~5980 μm². Two sensors were fabricated with a length of ~750 μm. The sensor based on the silica tube without rods was able to measure strain up to 1500 με, with a linear sensitivity of (1.95 ± 0.01) pm/με (see Fig. 5.16). Regarding the sensor with the new silica tube design, it was possible to measure strain up to ~2500 με, with a linear sensitivity of (3.39 ± 0.01) pm/με.
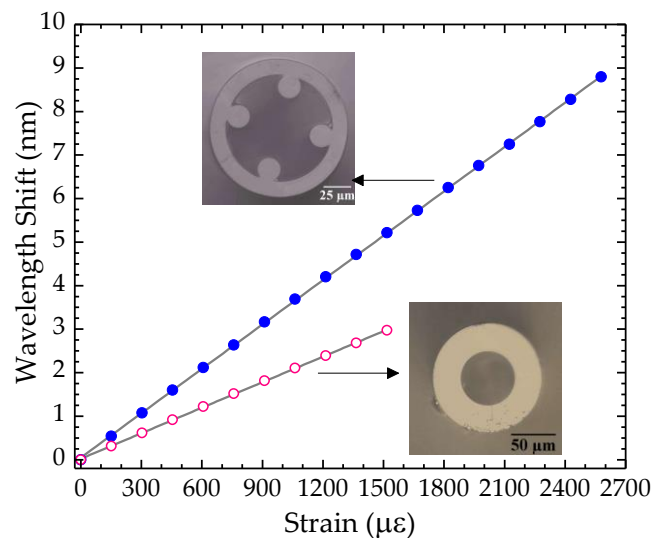
Figure 5.16 – Sensors response to the applied strain until rupture. The insets show the cross-section photographs of the silica tube used as sensing element in each case.

The size of the hollow core area plays an important role in the sensitivity, along with the FP cavity length. Large hollow core areas and short cavity lengths translate into an enhancement of the sensitivity. This occurs due to a much reduced effective Young modulus of the hollow core structure associated with the smaller fraction of silica material in its cross-section. Therefore, most of the deformation occurs in the tube region and with a spatial rate that increases with the reduction of the tube length, therefore increasing the strain sensitivity. Besides, the presence of the four rods constitute a reinforcement to the new structure, which shows favorable sensing properties both in

what concerns strain sensitivity and mechanical resilience, indicating its adequacy for application in harsh environments.

5.4   Measuring Strain at High Temperatures (Part II): Fiber Bragg Gratings

In this Section, a fiber Bragg grating (FBG) written in standard single mode fiber (SMF) is characterized in strain at different temperatures. The influence of the thermal annealing in the sensor response is also investigated.

5.4.1   Sensor Design and Spectral Characteristics

The FBGs used in this work were written in standard SMF using the point-by-point femtosecond laser technique. The devices were fabricated at the Aston Institute of Photonic Technology, in Birmingham, England. With such inscription technique, the laser beam is focused in the fiber core and due to its high power and very high repetition rate, as it moves along the fiber a local change in the core refractive index is induced (see Fig. 5.17). These structures are highly stable thermally, and can withstand temperatures above 1000 °C [234, 240]. The details regarding the inscription are included in the Appendix II.
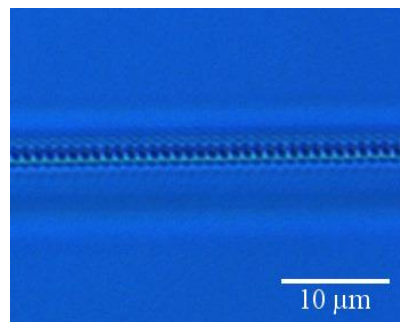
Figure 5.17 – Microscope photograph of a fiber Bragg grating written using the point-by-point femtosecond laser technique.

The experimental setup used to characterize the devices, shown in Fig. 5.18, was constituted by a broadband optical source (bandwidth of 100 nm, centered at 1570 nm) and an optical spectrum analyzer (OSA), with a resolution of 0.01 nm. All readings were performed in transmission.
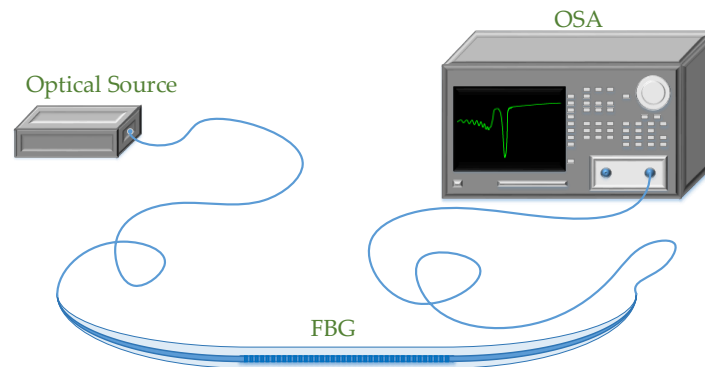
Figure 5.18 – Scheme of the experimental setup. OSA refers to the optical spectrum analyzer and FBG is the fiber Bragg grating (the scheme is not to scale).

The two FBGs characterized in this work had a length of 5.7 mm. The FBG1 presented a reflectivity of 94.23 %, a Bragg wavelength of 1550.42 nm and a full-width at half-maximum (FWHM) of ~0.33 nm. In its turn, the FBG2 had a reflectivity of 99.96%, the Bragg wavelength was of 1550.31 nm and the FWHM was of ~0.82 nm. The transmission spectra of both samples are shown in Fig. 5.19.
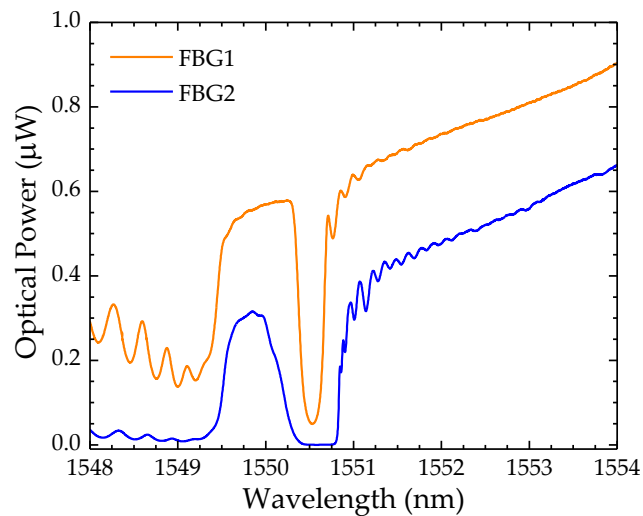
Figure 5.19 – Initial transmission spectra of the two fiber Bragg gratings (FBGs).

5.4.2   Experimental Results

The sensors were tested to strain at high temperatures as in the case of the FP cavity previously described. One sample, FBG1, was subjected to an annealing treatment prior to the strain measurements, while the other, FBG2, was tested without annealing. The FBG1 was placed inside a tubular oven, in a centered position and on the outside it was fixed to a supporting structure on one end and to a translation stage on the other end.
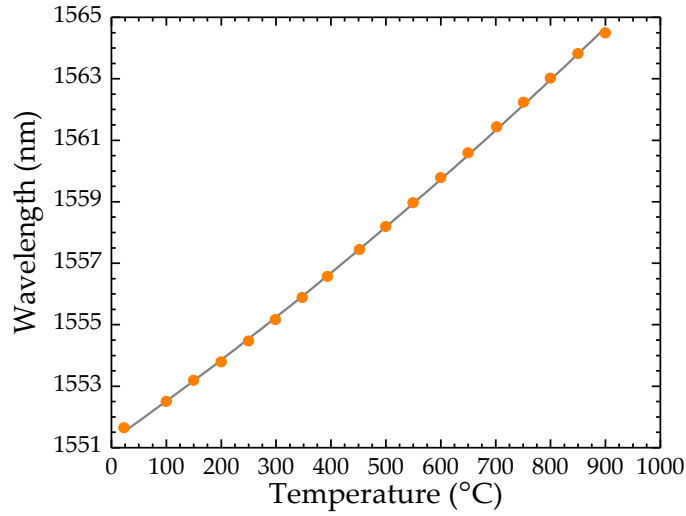
Figure 5.20 – FBG1 response to temperature.

At this stage of the experiment, the fiber was kept straight but loose, without any tension applied. Temperature was increased up to 900 °C and the Bragg wavelength shift was measured as the oven heated. The response, shown in Fig. 5.20, exhibits a nonlinear behavior that can be approximated to the second order equation:

$$\lambda(T) = \left(3.5 \pm 0.1\right) \times 10^{-6}\, T^2 - \left(11.5 \pm 0.1\right) \times 10^{-3}\, T + \left(1550.9 \pm 0.1\right), \tag{5.1}$$

where λ is the wavelength, in nm, and T corresponds to the temperature, in °C.

Once the oven reached 900 °C, it was kept at that temperature for ~7 hours, performing thermal annealing to the structure. The wavelength shift with time is presented in Fig. 5.21 (a). There is a higher increase in the Bragg wavelength in the first 40 minutes, with a rate of (12.4 ± 0.1) pm/min. After the first two hours, this variation was smoother, and the shift rate decreased to (0.9 ± 0.1) pm/min. However, after 7 hours the wavelength did not stabilize, which might have influenced the results that followed. Besides the wavelength shift, the reflectivity of the FBG1 also changed during the annealing process. The behavior is shown in Fig. 5.21 (b). There was a higher decrease in the reflectivity in the first 40 minutes than from that moment on. However, the reflectivity only decreased 3.1% during the thermal annealing, a consequence of the thermally ultra-stable defects that arise from the interaction between the high intensity laser pulses and the glass matrix of the fiber core [241]. After an annealing time of 7 hours, the oven was switched off and cooled down until it reached room temperature.
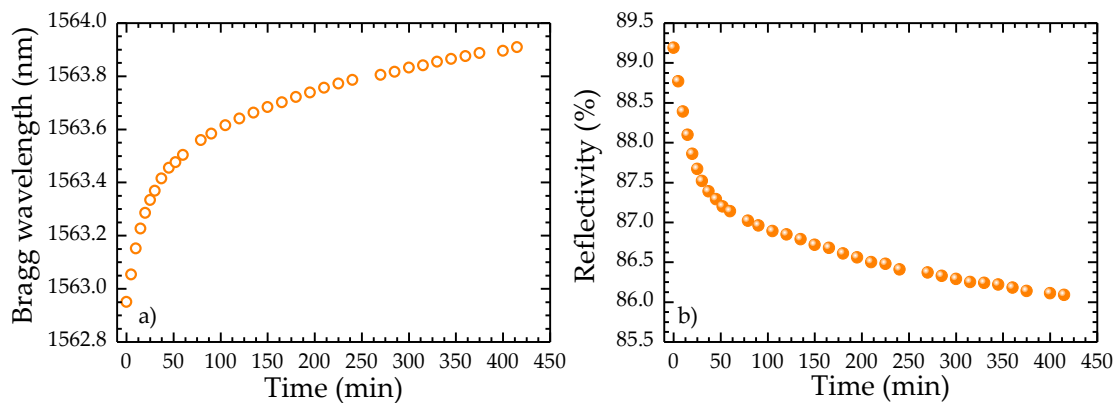
Figure 5.21 – FBG1 response to an annealing temperature of 900 °C. (a) Bragg wavelength shift with time and (b) Reflectivity variation with time.

The sample was once again subjected to temperature variations in the same range. However, now the temperature increase was set to steps of 150 °C until 750 °C and of 50 °C from 750 °C to 900 °C. At each temperature step the system was stabilized for ~30 minutes and strain measurements were carried out, by increasing strain up to 1000 µε and decreasing it back to its initial state. Figure 5.22 (a) shows the variation of the FBG1 strain sensitivity with temperature. The up curves are relative to the strain increase whereas the down curves correspond to the sensitivities obtained when decreasing strain. The sensor response was always linear, although the sensitivity changed slightly with temperature, as can be seen in Fig. 5.22 (a). For temperatures below 600 °C the sensitivity obtained when increasing and decreasing strain was nearly the same, of (1.2 ± 0.1) pm/µε. The small increase in the strain sensitivity observed at temperatures higher than 750 °C can be due to the fact the annealing has not been fully performed yet. In order to infer about the response of the grating structure without a prior thermal treatment, the FBG2 was also subjected to measurement of strain at high temperatures. The response, depicted in Fig. 5.22 (b) shows that at temperatures above 750 °C the sensitivity had a pronounced increase when tension was applied (up curves). Besides, at this temperature range, the sensor response became non-linear, a consequence of the joint effect of annealing and the applied strain. However, when the strain was diminished (down curves), the sensor response was linear and nearly constant. This effect was also observed in the FP configuration, and is due to the change of the Young modulus, as well as the induced plasticity in the fiber at such high temperatures.
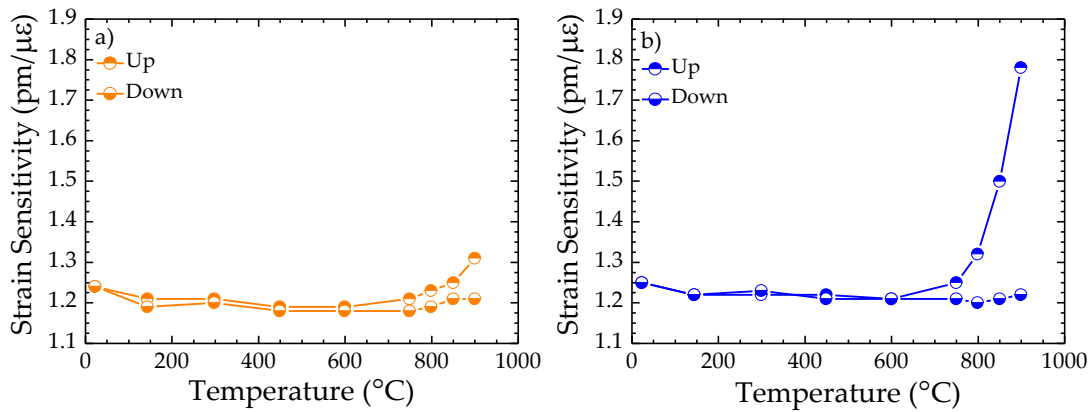
Figure 5.22 – Strain sensitivity variation with temperature (a) after annealing at 900 °C, FBG1, and (b) without annealing, FBG2.

With this sensing structure it is possible to clearly observe the effects of subjecting the fiber to high temperatures, when compared to the FP configuration, since in this case there is only a peak to track, opposite to the interferometric behavior of the previous sensor. Figure 5.23 shows the evolution of the FBGs spectra, acquired at room temperature. There is the initial spectrum, taken before beginning the experiments (dotted curves), after annealing (only in the case of FBG1, the dashed curves) and after all measurements were performed (final spectrum, solid curve). The main parameters are also listed on Table 5.1, for a clear comparison between the results. In the case of FBG1 (Fig. 5.23 (a)), the major wavelength shift occurred during the annealing procedure. In this case, the wavelength shift was of 0.72 nm. The effect of applying strain at high temperatures after the thermal treatment induced a variation of 0.17 nm, translating into a total Bragg wavelength shift of 0.89 nm.
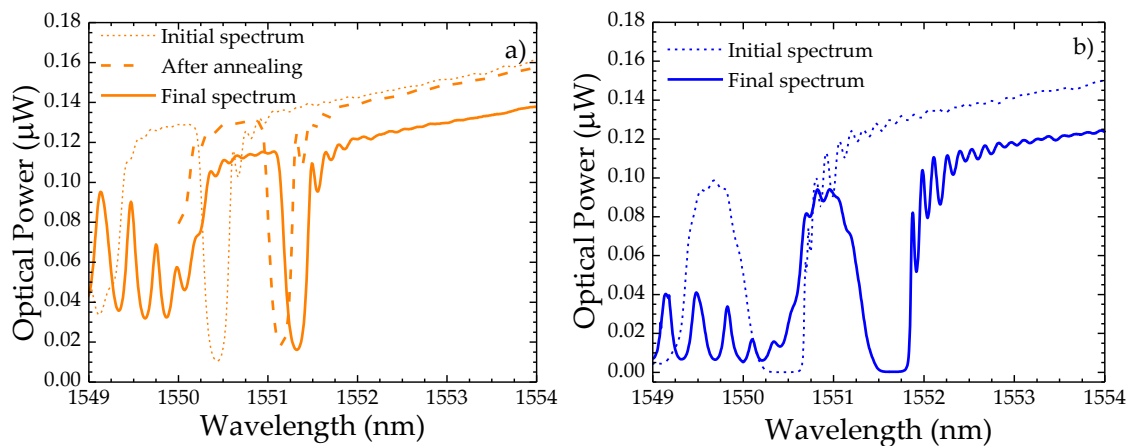
Figure 5.23 – Transmission spectra of (a) FBG1, before annealing (dotted curve), after annealing (dashed curve) and after strain at high temperatures (solid curve) and (b) FBG2, before (dotted curve) and after (solid curve) being subjected to strain at high temperatures.

On the other hand, the direct measurement of strain at high temperatures without any previous thermal treatment originated a Bragg wavelength shift of 1.24 nm. When strain and/or temperature are applied to a FBG, not only the grating period changes, but also the mean refractive index. However, the dominant parameter in the case of strain is the change in the grating period, whereas for temperature, it is the change in the refractive index. Without the previous thermal treatment, the structure is not so stable (which was evidenced by the non-linear response to strain), translating into a higher shift in the transmission spectrum. The FWHM diminishes in both cases, being more pronounced when no thermal annealing was performed. Besides, the reflectivity also diminished slightly.

Table 5.1 – Parameters of the FBGs at room temperature. The values were obtained through the optical transmission spectra, prior to any measurements (initial values), after 7 hours thermal annealing at 900 °C and after applying strain at different temperatures (final values). The total wavelength shift is relative to the beginning and end of the measurements.

	Parameter	FBG1	FBG2
Initial values	R (%)	94.23	99.96
	FWHM (nm)	0.33	0.82
	λ_{B1} (nm)	1550.42	1550.31
After annealing	R (%)	89.63	No annealing
	FWHM (nm)	0.31	
	λ_{B2} (nm)	1551.14	
Final values	R (%)	89.40	99.84
	FWHM (nm)	0.29	0.65
	λ_{B3} (nm)	1551.31	1551.54
Total wavelength shift	$\Delta\lambda = \lambda_{B3} - \lambda_{B1}$ (nm)	0.89	1.24

5.5 Final Remarks

In this Chapter, three different configurations were proposed, one for the measurement of strain at room temperature and the other two for the measurement of strain at high temperatures. The first configuration was a Fabry-Perot (FP) cavity based on a hollow core photonic crystal fiber spliced between two sections of single mode fiber. The dependence of the strain sensitivity on the cavity length and with the total length was explored. It was found that smaller cavities and longer total lengths exhibit higher

sensitivities to strain. This configuration presented low sensitivity to temperature. This study was further developed by considering a different sensing element, based on a silica tube spliced between two sections of single mode fiber. Several samples were characterized in strain, and it was confirmed that the smaller the FP cavity length, the higher the sensitivity. The sensor showed low sensitivity to temperature, thus being a good candidate to perform strain measurements in high temperature environments. However, when strain was applied at temperatures higher than 750 °C, the sensitivity increased as the fiber was tensioned. When the fiber returned to its initial state, without strain applied, the sensitivity decreased to a value similar to the one found at lower temperatures. This difference was reduced through thermal annealing before subjecting the sensing head to strain at extreme conditions. Furthermore, the strain sensitivity decreased as temperature increased up to 600 °C, increasing once again for higher temperatures. This configuration was also compared to a FP cavity based on a conventional silica tube and presented not only higher strain sensitivity, but also better mechanical resilience.

Fiber Bragg gratings written in standard single mode fiber were also characterized in strain at high temperatures. The fabrication process was determinant for the high thermal stability of the device, as it was produced using the point-by-point femtosecond laser technique. The Bragg wavelength shifted towards longer wavelengths and the reflectivity decreased slightly, independently of the annealing treatment. However, the sensor response became more stable after the annealing treatment, following the same trend as in the FP configuration.

Fiber Lasers for Sensing
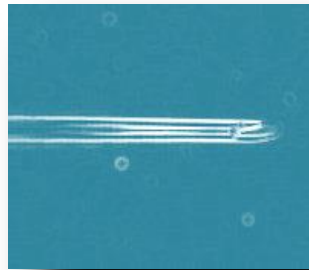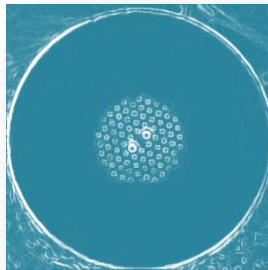
6.1   Introduction

The first works on optical fiber lasers were published in the 1960s by E. Snitzer [242]. However, it was only in 1993 that Kim *et al.* presented the first optical fiber laser as sensor with frequency read-out [243]. The Nd^{3+}-doped fiber, used as the cavity active medium, was subjected to lateral stress variations that modified the fiber birefringence, thus changing the modal beat frequency. In the proposed configuration, two dichroic mirrors were employed to create the cavity. The employment of a Faraday rotating mirror was proposed by Park *et al.*, for the measurement of magnetic-fields [244]. The use of such reflective element ensured the laser stability to strain and temperature variations.

In the meantime, with the development of the fiber Bragg grating (FBG), the quintessentially wavelength filter, the external bulk mirrors fell into disuse. The FBGs were not only used as reflective elements, but also as sensing devices, thus combining the advantages of the fiber laser (such as high signal-to-noise ratio (SNR) and reduced linewidth) with the ability to perform active sensing, by exposing one mirror, or even the whole cavity, to the environmental changes to be measured.

The most simple fiber laser sensor, and the one most explored by the scientific community, is the linear cavity, where the active medium (usually Er^{3+}-doped fiber) is placed between two FBGs, constituting the distributed Bragg reflector (DBR) laser. The presence of a wavelength division multiplexer (WDM) enables the coupling of the 980 nm pump light to the cavity [245]. This kind of configuration has been used to measure dynamic strain [246], temperature [247], ultrasound [248], liquid refractive index [249], gas pressure [250] and twist [251].

Still considering the linear cavity configuration, it is possible to achieve laser action by using a single phase-shifted FBG [252]. This type of fiber laser is usually denoted as distributed feedback (DFB) laser, and it has been used for measurement of several physical parameters, such as pressure and force [252], simultaneous measurement of strain and temperature [253], or even acoustic signals [254].

A different approach to the linear cavity is the fiber ring laser. In such cavity, the Er^{3+}-doped fiber is incorporated in a loop. The pump is coupled to the ring cavity through a WDM and the output signal is detected by using an optical coupler. In a simpler configuration, a commercial erbium-doped fiber amplifier (EDFA) is placed in the loop. The wavelength filter can be a FBG placed outside the ring, connected through an optical circulator [255], a pair of long period gratings incorporated in the ring [256, 257], a section of polarization maintaining (PM) PANDA fiber inside the ring [258] or even a phase-shifted chirped FBG [259]. The fiber ring laser has been applied in the measurement of pressure [260], bending and strain [256], vibration [255], and torsion [257]. When compared to the behavior linear cavities, the unidirectional travelling wave obtained in the ring configuration eliminates both the backscattering and the spatial-hole burning effects [261]. Thus, these cavities present good stability, flexibility, and are easy to manufacture [262].

Going further in the ring configuration, if a non-amplifying loop is added to the amplifying loop through an optical coupler, a figure-of-eight configuration is obtained. In this case, the inclusion of an optical filter in the loop can be decisive in achieving good output stability [263]. The filter can be a PM fiber [261], a twin-core photonic crystal fiber (PCF) [264], or a triangular core PCF [265]. All these works have been proposed only for laser action, not for sensing.

In this Chapter, two fiber sensors are proposed, one for torsion measurements and the other for strain sensing. The first sensor is based on a post-processed FBG. The device is subjected to strain measurements, where it exhibits an ultra-high sensitivity. Two different approaches are compared, for passive and active measurements. The second configuration consists on a figure-of-eight laser, whose interferometric filter, a PM PCF, also acts as the sensing element. In this case, the torsion can be applied over a range of 180°.

6.2 Strain Sensor based on Post-Processed Fiber Bragg Grating

The sensor developed in this work consisted on an etched fiber Bragg grating tip. The ultra-thin structure was characterized in strain and temperature. A theoretical model was used to better understand the device behavior.

6.2.1 Theoretical Considerations

The Bragg wavelength of a fiber Bragg grating (FBG) is determined by $\lambda_B = 2n_{eff}\Lambda$, where n_{eff} and Λ are, respectively, the effective refractive index of the propagating mode and the grating pitch [266]. When the FBG is subjected to axial strain, ε, its Bragg wavelength will shift according to Eq. 6.1:

$$\Delta\lambda_B = \lambda_B(1 - p_e)\varepsilon, \tag{6.1}$$

where p_e is the photoelastic coefficient for silica, considered to be ≈ 0.22 [267]. In the case of a tapered FBG created by means of chemical etching, the cross-section area of the fiber changes with the position z, as exemplified in Fig. 6.1.
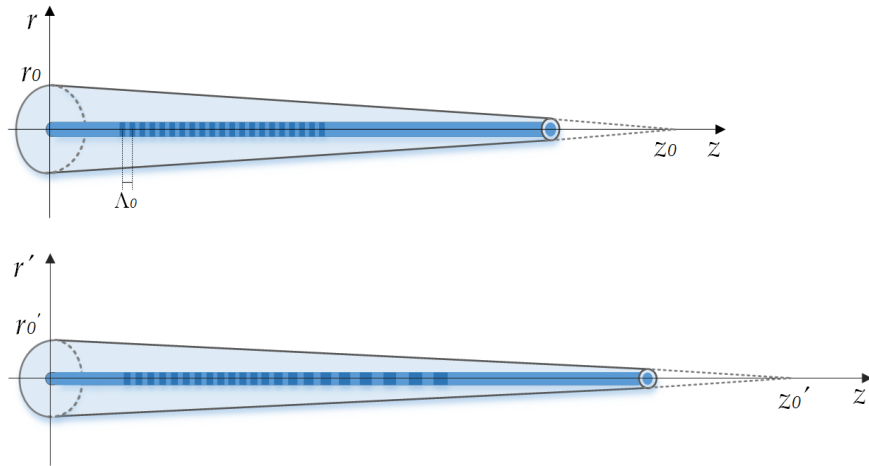
Figure 6.1 – Scheme of a tapered FBG without strain applied (top) and under strain (bottom). Adapted from [268].

Considering a linearly tapered fiber, the radius across z is given by [268]

$$r(z) = r_0\left(1 - \frac{z}{z_0}\right), \tag{6.2}$$

where r_0 is the original radius and z_0 is the point along the z axis where the radius of the fiber becomes zero. The cross-section area comes also a function of z, according to Eq. 6.3:

$$A(z) = \pi r(z)^2 = \pi r_0^{\ 2}\left(1 - z/z_0\right)^2 . \tag{6.3}$$

When the fiber is under a tension force N, the strain along z can be determined through

$$\varepsilon(z) = \frac{N}{EA(z)} = \frac{N}{E\pi r_0^{\ 2}\left(1 - z/z_0\right)^2} , \tag{6.4}$$

where E is the Young modulus of silica. The strain at $z = 0$ is given by

$$\varepsilon(0) = \frac{N}{E\pi r_0^{\ 2}} . \tag{6.5}$$

Thus, substituting Eq. 6.5 in Eq. 6.4, one gets that

$$\varepsilon(z) = \frac{\varepsilon(0)}{\left(1 - z/z_0\right)^2} . \tag{6.6}$$

When the fiber is under strain, the FBG pitch along the z axis becomes a function of the applied tension force, according to Eq. 6.7:

$$\Lambda(z) = \Lambda_0(1 + \varepsilon(z)) = \Lambda_0 + \frac{\Delta\Lambda(0)}{\left(1 - z/z_0\right)^2} , \tag{6.7}$$

where Λ_0 is the original pitch and $\Delta\Lambda(0) = \varepsilon(0)\Lambda_0$ is the change in the pitch at $z = 0$. The variation of the pitch along the FBG translates into a chirp of the spectrum. Besides, the distribution of strain is not constant in this case.

The previous equations were used in a numerical simulation to better understand the consequences of having such a structure subjected to strain. Some assumptions were made, based on the etching behavior observed experimentally. The chemical etching was performed in the liquid phase; thus, there was an abrupt change of the fiber diameter at the interface between the un-etched and the etched regions. The decrease of the fiber cross-section area will induce a larger amount of strain throughout the etched region.

Considering that the whole structure is under the same amount of tension force, and using Eq. 6.5, it is possible to relate the strain applied to the un-etched structure to the one obtained at the etched region:

$$\varepsilon_u A_u = \varepsilon_e A_e \Leftrightarrow \varepsilon_e = \frac{\varepsilon_u r_u^2}{r_e^2},$$

(6.8)

where the subscripts u and e designate the un-etched and etched fiber sections, respectively. Thus, considering fiber radii of 62.5 μm and 10 μm (r_0), for the un-etched and etched fiber regions, respectively, and that the length of un-etched fiber is much larger than the length of etched fiber, when 10 με are applied to the whole structure, the amount of strain at the beginning of the tapered region is determined to be ~390 με. The other parameters considered for the numerical simulations were a reduction of the fiber radius by 10^{-3} μm by unit length, meaning that $z_0 = 9 \times 10^3$ μm. It was also considered that the FBG was located ~1.5 mm after the beginning of the tapered region, and had a length of 3 mm. Besides, three different values were considered for the strain applied to the whole structure: 10, 50 and 100 με. The results obtained for the variation of the FBG pitch and for the strain along the taper length are shown in Fig. 6.2. The gray rectangle indicates where the FBG was positioned along the fiber.
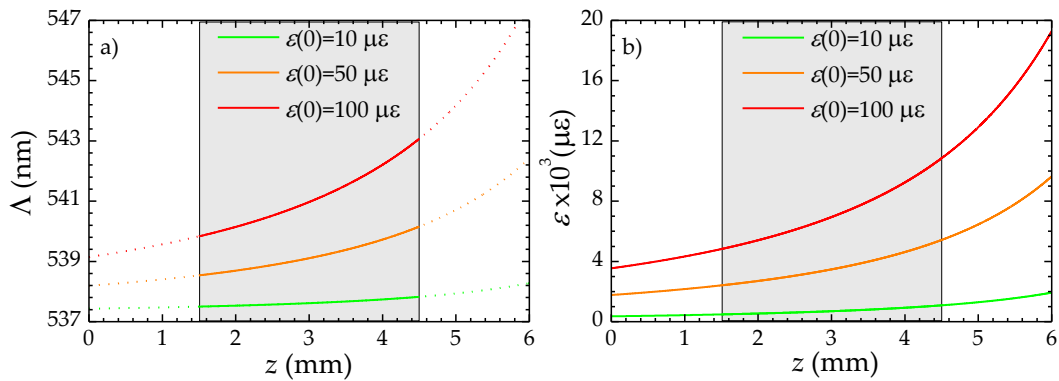
Figure 6.2 – Numerical simulation of an etched FBG, considering three values of initial strain. (a) variation of the pitch with the length and (b) strain variation along the grating length.

Figure 6.2 (a) presents the pitch variation along the z axis, for three different values of initial strain. A maximum increase of ~4 nm was attained, when the applied strain was 100 με. The dotted lines represented in the Figure are the expected variation of the FBG pitch if it was located in other regions of the taper. When the analysis is performed

considering the increase of strain as the taper becomes thinner, the values obtained are much more explanatory. In fact, according to the green curve in Fig. 6.2 (b), when the fiber is subjected to 10 $\mu\varepsilon$, the strain in the tapered region, in $z = 0$ mm, is ~100 times higher. In this case, the applied strain only increases slightly with the taper length. However, when the applied strain is of 100 $\mu\varepsilon$, the tension will be more than 5 times higher near the fiber tip than at the beginning of the taper. However, the strain experienced by the FBG increases over its length and, at its edge, the strain is twice the value determined at its beginning. Thus, although the whole structure is only strained by 100 $\mu\varepsilon$, the tapered region is locally strained up to 20000 $\mu\varepsilon$, an impressive amount of strain for such a thin structure.

The variation of strain along the FBG length, and its induced broadening of the grating pitch translate into a chirped spectrum, which broadens as strain is applied, as a consequence of an increase in the pitch difference between the beginning and the end of the FBG. Besides, this sensor is expected to be more sensitive to the applied strain than a standard, un-etched FBG, due to the unusual distribution of strain throughout the structure.

6.2.2 Sensor Design and Spectral Characteristics

The first step to produce the sensor consisted of writing the FBG in a photosensitive SMF, using a KrF excimer laser that operated at 248 nm and the phase-mask technique. The fiber, commercialized by the FBGS Company, had a core diameter of 5 μm, a cladding diameter of 125 μm and a numerical aperture of 0.26. The configuration for the gratings inscription, described in Appendix III, was based on a Talbot interferometer. Since the fiber was photosensitive, there was no need for prior hydrogenation. The length of the FBG was of 3 mm. The second step consisted of cleaving the end section of the sensor, guaranteeing that there were ~2 mm of SMF with no inscription between the FBG and the fiber end. Since the core of the fiber was Ge-doped, the etching rate in this region was higher than that of the cladding. Thus, it was important to ensure that the acid did not reach the core area with the FBG. The following step was to submerge the fiber tip in a 40%-hydrofluoric acid (HF) solution for around one hour, at room

temperature, thus obtaining a very thin fiber tip, with a thickness lower than 10 μm. The chemical reactions involved in this step are [81]

$$SiO_2 + 6HF \rightarrow 2H_2O + H_2SiF_6,$$
$$GeO_2 + 6HF \rightarrow 2H_3O^+ + GeF_6^{2-}.$$

(6.9)

The chemical etching in the liquid medium favored the formation of a linearly tapered fiber tip, with a small diameter slope over the etched tip length. If the etching were performed in gas medium, a sharp conic-shaped tip would be expected [226]. Figure 6.3 (a) shows the reduction of the cladding diameter as a function of time. From the linear relationship between these two parameters, it is possible to estimate the etching rate to be ~(115 ± 1) μm/h. Fig. 6.3. (b)-(d) show microscope images of the fiber at different etching times. On Fig. 6.3 (b), the fiber was submerged for ~30 min and the cladding diameter was of (65 ± 2) μm. Notice the conical shape of the inner region, that corroborates the assumption that the etching will be faster in the core than in the cladding. After ~55 min, the outer diameter was of (18.2 ± 2) μm (Fig. 6.3 (c)). Finally, after a time of ~61 min, the diameter was reduced to (8 ± 2) μm.
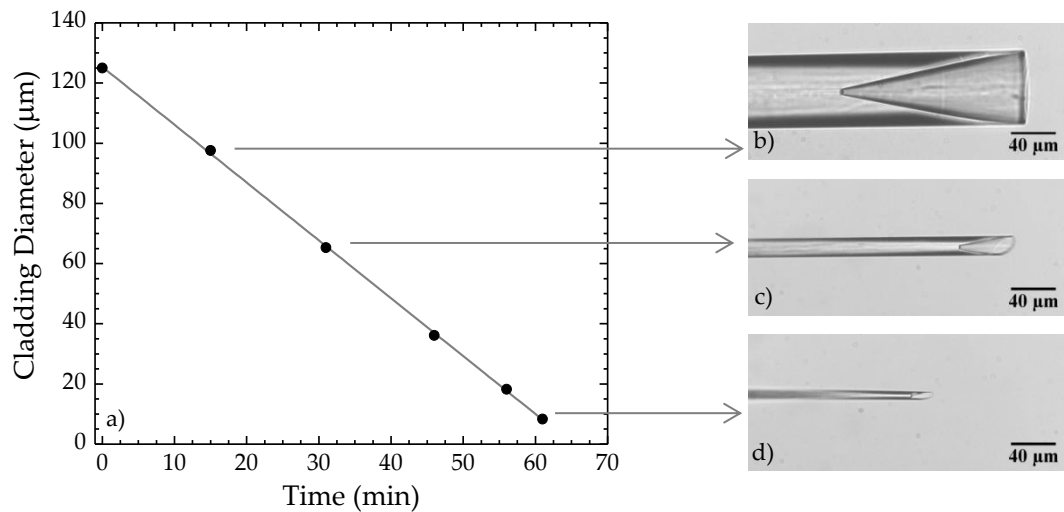
Figure 6.3 – (a) Cladding diameter variation with the chemical etching time. Also shown microscope images of the fiber tip after etching times of (b) ~30 min, (c) ~55 min and (d) ~61 min.

Throughout this time, there was a reduction of the length of the fiber; however, it did not reach the FBG inscription area, as evidenced by the reflection spectra, taken at different time steps (0, 30, 55 and 61 min), shown in Fig. 6.4. The Bragg wavelength shifts towards blue and, as the fiber diameter decreases below 10 μm, this shift becomes more

pronounced. As the fiber becomes thinner, the evanescent field becomes more exposed to the environment, decreasing the effective refractive index of the fundamental mode [269]. Besides, the full-width at half-maximum (FWHM) also increases significantly at this point. This chirp effect is due to the conic shape acquired by the fiber tip during the etching, as discussed in Section 6.2.1. Several FBG etched tips were produced as described and all presented identical properties.
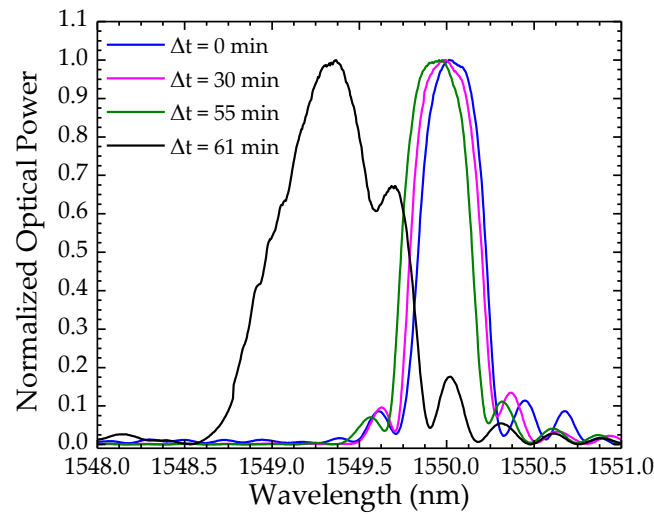
Figure 6.4 – Reflection spectra of the FBG at different etching times.

6.2.3 Passive Configuration

One FBG etched tip sample was tested for the measurement of strain and temperature, using the experimental setup shown in Fig. 6.5. The optical source had a bandwidth of 100 nm, centered at 1570 nm. Regarding the optical spectrum analyzer (OSA), the resolution used was 0.01 nm. An optical circulator connected these two components and the etched tip, as depicted in the Figure.
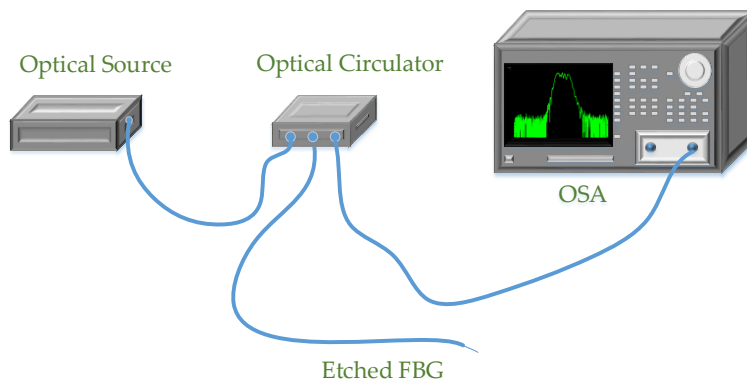
Figure 6.5 – Scheme of the experimental setup.

To perform strain measurements, the tip was placed in a translation stage with a resolution of 0.01 mm. In Fig. 6.6, the spectra of the grating with no strain applied and with a strain of 93 μɛ are shown. Two different effects arise when strain is applied: the Bragg wavelength shifts and the spectrum broadens. This behavior is in agreement with the theoretical considerations given in Section 6.2.1. Since the sensor has a conical shape, the stress is not constant throughout its length. This translates in the elongation of the FBG periods, with a consequent widening of the range of wavelengths filtered.
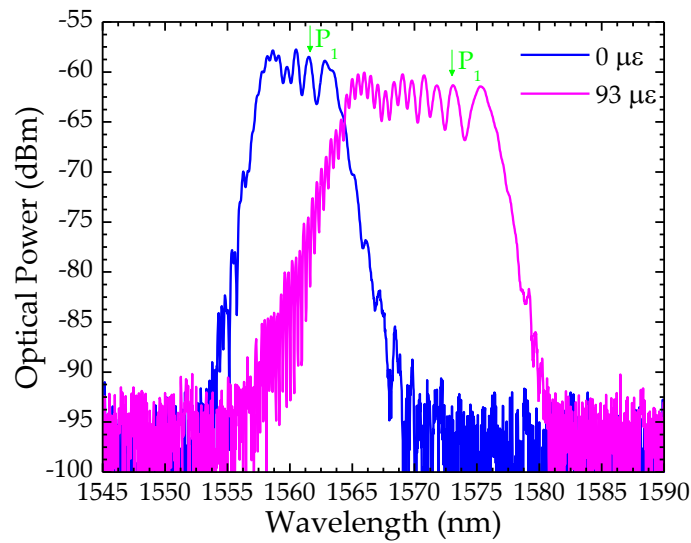
Figure 6.6 – Spectra of the etched FBG tip when no strain is applied (blue line) and with 93 μɛ (pink line).

The strain analysis can be done from different points of view, considering the wavelength shift of the whole spectrum (measured at 3 dB), the changes in the FWHM of the spectrum, or even by tracking one single peak. In the first case, a linear sensitivity of (104.7 ± 1.1) pm/μɛ was achieved, as presented in Fig. 6.7 (a). This indicates that it is possible to improve ~100 times the sensitivity of a standard FBG with the proposed configuration [267]. If one considers the variation of the FWHM, shown in Fig. 6.7 (b), the experimental data are also well adjusted by a linear fitting. In this case, the sensitivity obtained was (61.7 ± 1.7) pm/μɛ.

A different analysis was performed by considering the peak identified as P_1 in Fig. 6.6. The response, also shown in Fig. 6.7 (a), was likewise linear and a sensitivity of (127.3 ± 2.4) pm/μɛ was determined through the linear fitting. The increase of sensitivity in this case was mainly due to the fact that the wavelength of operation was longer than

the one obtained for the full spectrum analysis and that in the region considered the fiber was thinner, thus subjected to a higher amount of strain, as predicted by the theoretical analysis. The reason why the sample was only subjected to 100 με, besides the high increase of strain over the sensing element, was the intention of comparing the sensing head behavior in different situations. However, with this configuration it is quite a challenge to measure high strain ranges. With only 100 με, there was a shift of ~10 nm on the Bragg wavelength. This means that if the applied strain was higher than 600 με, the Bragg wavelength would be outside the source spectrum. Besides, with the broadening of the FWHM it would become more difficult to track the changes of the Bragg wavelength. Thus, this ultra-sensitive configuration is only suitable for applications where small strain changes take place.
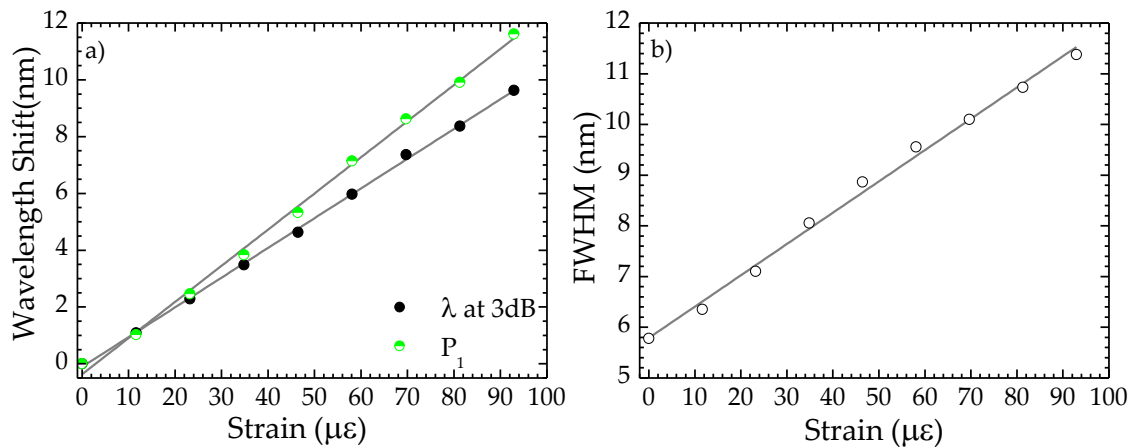
Figure 6.7 – Response of the etched FBG tip to the applied strain by monitoring (a) the wavelength at 3 dB (solid black dots) and the peak P₁ wavelength (green dots) and (b) the full-width at half-maximum (FWHM).

To perform the temperature measurements, the fiber tip was carefully removed from the translation stage and introduced in a tubular oven, which presented a temperature resolution of 0.1 °C. The sensor exhibited the same response of a typical un-etched FBG, with a linear sensitivity of (9.4 ± 0.3) pm/°C (see Fig. 6.8).

In this case no broadening of the spectra was observed, only a shift of the Bragg wavelength. Thus, by taking into account this effect due to temperature and the FWHM changes due to strain; it is possible to use this sensing tip to perform simultaneous measurement of temperature and strain.
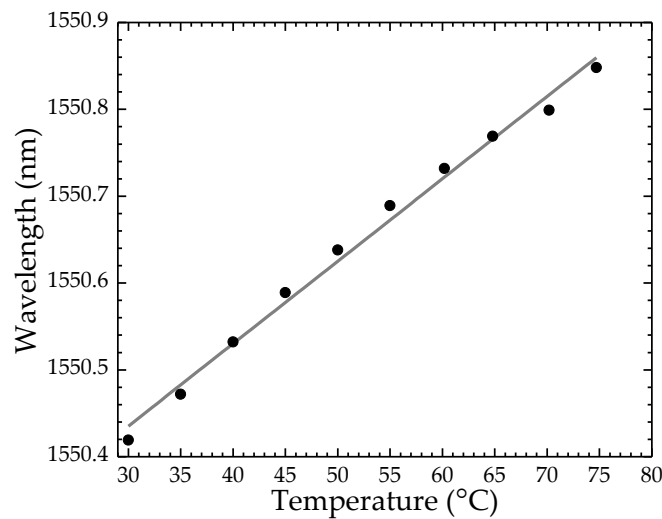
Figure 6.8 – Sensor response to temperature.

6.2.4   Active Configuration

The broadening of the FWHM can make the monitoring of the sensor response to strain difficult. This limitation can be overcome by incorporating the sensing tip in a fiber ring laser configuration, such as the one presented in Fig. 6.9. An erbium-doped fiber amplifier (EDFA) was connected between an optical circulator and an 80/20 optical coupler. To close the loop, a connection was made between the optical circulator and the optical coupler. The 20% port of this device was connected to the data acquisition system, whereas the 80% arm was connected to the input port of the EDFA. The fiber with the etched FBG tip was connected to the optical circulator and the readings were performed in reflection. Two different kinds of equipment were used to acquire the signal, depending on the type of measurement. Thus, for reading optical power variations, a powermeter was used (with a maximum resolution of 0.01 nW); and for spectral monitoring, an OSA with a resolution of 0.01 nm was employed.
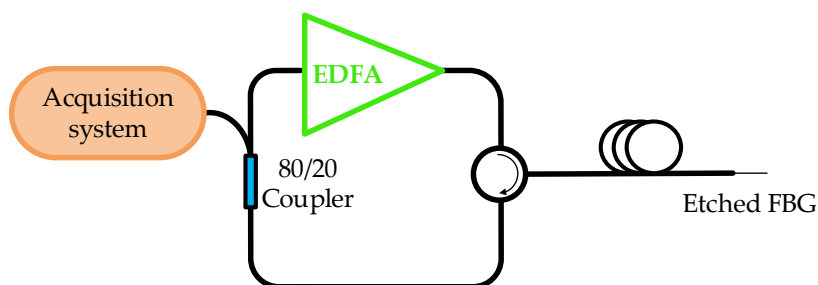
Figure 6.9 – Scheme of the experimental setup. EDFA is the erbium doped fiber amplifier and FBG stands for fiber Bragg grating.

The fiber laser sensor output power dependence on the EDFA pump power is shown in Fig. 6.10. The laser exhibited a threshold power of (5.48 ± 0.05) mW and a slope efficiency of (6.8 ± 0.1)%. Besides, the signal-to-noise ratio (SNR) of this device was above 50 dB. The stability of the laser cavity was analyzed by measuring the output power over 60 minutes, under a constant input power of 50 mW. Throughout this time, a fluctuation of only 0.11 mW was observed and the emission was quite stable, as can be seen by the purple line in Fig. 6.10.
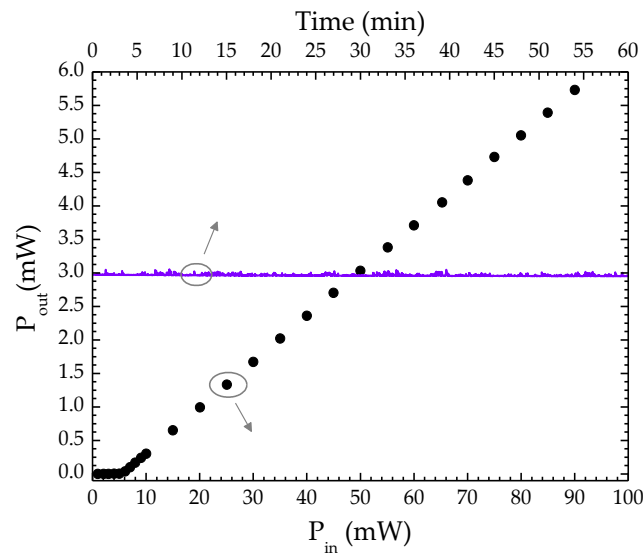
Figure 6.10 – Laser output power as a function of the pump power. The laser stability for a constant pump power of 50 mW, over 60 min is also shown (purple line).

Strain measurements were performed once again, using the same translation stage as in the previous configuration. Fig. 6.11 presents the laser emission curves for different strain values, the first peak (black line) corresponding to 0 µε. The laser was emitting at 1558.4 nm, which corresponds to the lower wavelength region of the chirped spectrum (see Fig. 6.11). Since the chirp increases for longer wavelengths and the sensitivity of the FBG also depends on this parameter, this active sensor is expected to be less sensitive than the passive one, explored in the previous configuration. Nevertheless, with the proper tuning of the lasing wavelength, higher sensitivities could be achievable. The inset in Fig. 6.11 (a) shows the dependence of the integrated power, measured with the powermeter, on the applied strain. There is a pronounced decrease in the optical power with increased strain which is due to the decrease in the gain of the EDFA in this range. In fact, this is one of the major limitations of this sensing head, since above 100 µε the

filter was placed out of the EDFA gain range and there was no laser emission. However, there was no apparent broadening of the laser peak, whose FWHM was limited by the OSA resolution (0.01 nm).

The wavelength variation with the applied strain is represented in Fig. 6.11 (b), for the case of the etched FBG tip (solid black lines) and for a non-etched FBG (purple hollow circles). The non-etched FBG, with λ_B = 1551.07 nm, was subjected to the same experimental conditions as the etched one, for comparison purposes. As expected, the non-etched FBG presented a linear sensitivity of (1.1 ± 0.1) pm/με, whilst the etched FBG tip exhibited a linear sensitivity of (74.4 ± 1.2) pm/με. It should be highlighted that throughout the experiments the laser did not suffer from mode hopping.
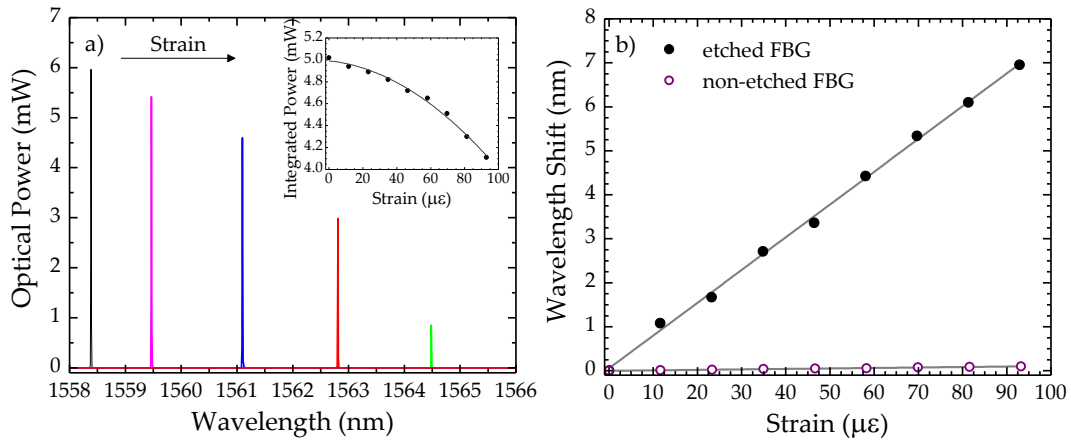
Figure 6.11 – Response of the laser to the applied strain, regarding (a) the spectral variation and (b) the wavelength shift. The inset represents the integrated power as a function of the applied strain.

The strain resolution of this sensor was evaluated by monitoring the emission peak wavelength over 30 seconds, for a constant strain value. Then, strain was increased by a step of 11.61 με and the measurement was repeated (see Fig. 6.12). Thus, the minimum value of strain, $\delta\varepsilon$, that the sensor is able to discriminate is given by [270]:

$$\delta\varepsilon = 2\frac{\sigma_\lambda \Delta\varepsilon}{\Delta\lambda}, \tag{6.10}$$

where σ_λ is the maximum standard deviation of λ for both values of strain, and $\Delta\varepsilon$ and $\Delta\lambda$ are the variation of strain and the mean wavelength shift between the two steps, respectively. This parameter was determined to be ~0.83 nm, and the maximum standard

deviation was of 0.01 nm. Thus, by applying Eq. 6.10, one gets a resolution of 280 nε. This value was mainly limited by the signal acquisition system resolution.
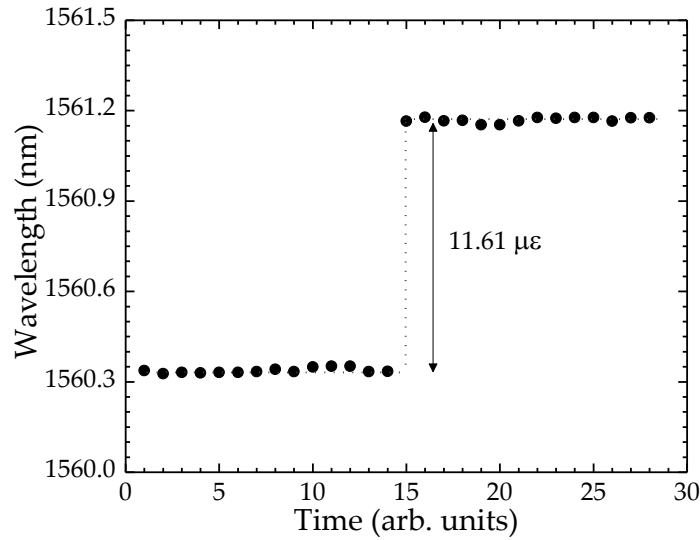
Figure 6.12 – Step technique to estimate the resolution of the fiber laser strain sensor.

6.3 Torsion Sensor based on Figure-of-Eight Fiber Laser

In this work, a figure-of-eight fiber laser is explored for torsion measurements. A section of polarization maintaining photonic crystal fiber acts both as interferometric filter and sensing element.

6.3.1 Working Principle

The figure-of-eight fiber laser sensor developed in this work was obtained according to the scheme depicted in Fig. 6.13. One of the loops was constituted by a pump laser diode emitting at 980 nm, a 980/1550 nm wavelength division multiplexer (WDM), an optical isolator, a 90:10 optical coupler and an optical spectrum analyzer (OSA), with a resolution of 0.01 nm, to perform the readings. In between the WDM and the optical isolator, a section of Er^{3+}-doped fiber (about 800 mm long) was inserted to provide the gain.

The concentrations of erbium and aluminum ions in the active fiber were of 1000 ppm and 10000 ppm, respectively. The numerical aperture of this fiber was 0.27, its core had a diameter of ~5 μm, and it presented a step index profile. The other fiber loop

included a polarization controller (PC) and the interferometric filter described in the following Section.
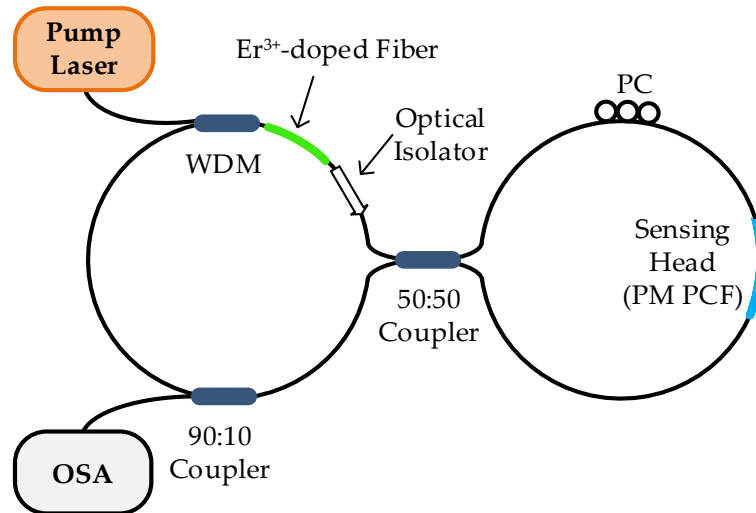
Figure 6.13 – Scheme of the figure-of-eight fiber laser. WDM stands for wavelength division multiplexer, PC is the polarization controller and OSA corresponds to the optical spectrum analyzer.

Using the appropriate pump power, the gain medium emits in the 1525-1560 nm region, according to the erbium spontaneous emission curve [271]. Light from the amplifier section will enter the loop on the right via the 50:50 coupler. The optical isolator is placed between the Er^{3+}-doped fiber and the optical coupler to prevent the return of light through this arm. The coupler splits the incoming light into two guided waves propagating in opposite directions: one wave will travel in the clockwise direction, with a certain velocity and polarization state; the other wave will propagate in the counter-clockwise direction, with a different velocity and polarization state. When they reach the coupler, the two beams interfere and a periodic spectrum is obtained. The sensing element, a polarization maintaining photonic crystal fiber (PM PCF), acts as an interferometric filter, selecting the wavelength at which laser emission will occur. Such selection results from the combination of two different aspects: the maximum transmission power of the filter and the region where the spontaneous emission gain is higher. Thus, the laser is expected to emit around 1530 nm. Depending on the polarization of lights travelling inside this loop, one or more lasing peaks were observed. However, all measurements were carried out with the emission of a single laser peak. The light that is recoupled at the 50:50 coupler is then redirected to the amplification loop, where a 90:10 coupler is introduced, to obtain the readings from the OSA.

6.3.2   Sensor Design and Spectral Characteristics

The sensing element used to perform the torsion measurements was an interferometric filter based on a PM PCF whose cross-section is shown in Fig. 6.14 (a). The fiber used is commercially available (PM-1550-01 from Thorlabs, Inc.) and presents a pure silica core and cladding. The fiber contains two large holes, with a diameter of 4.5 μm, and 82 smaller holes, with a diameter of 2.2 μm. The core, placed between the two larger holes, presents dimensions of 6.6/4.3 μm and the outer cladding has a diameter of 125 μm [272]. The characteristics of this fiber ensure a high birefringence, that beat length is lower than 4 mm and an attenuation < 2dB/km.
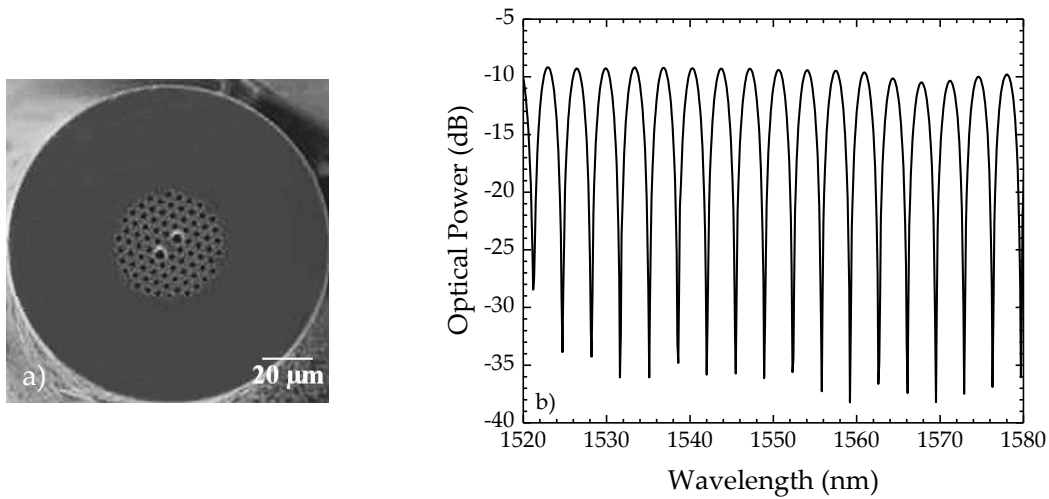
Figure 6.14 – (a) Microscopic photograph of the polarization-maintaining photonic crystal fiber used as sensing element. (b) Transmission spectrum of the sensor.

The channeled spectrum shown in Fig. 6.14 (b) was obtained by removing the amplification loop (the loop on the left on Fig. 6.13) and connecting one of the 50:50 coupler arms to the broadband optical source (bandwidth of 100 nm, centered at 1570 nm) and the other arm to the OSA, in a Sagnac configuration. The properties of the interferometric filter are gathered in Table 6.1. The channel spacing was determined by calculating the distance between two maxima, in the frequency domain. Regarding the channel passband and the full-width at half-maximum (FWHM), the two parameters are relative to the same concept, *i.e.*, the peak full width at half the maximum optical power. The former is in the frequency domain, whereas the last is in the wavelength domain.

Table 6.1 – Properties of the interferometric filter.

	Average Value
FWHM (nm)	1.72
Channel Spacing (THz)	0.43
Channel Passband (THz)	0.17

6.3.3 Experimental Results

The response of the laser optical power to the pump diode drive-in current is shown in Fig. 6.15. The current threshold was estimated to be (145.7 ± 5.2) mA and a maximum output power of (7.9 ± 0.1) µW was achieved for a drive-in current of (229.7 ± 0.1) mA.
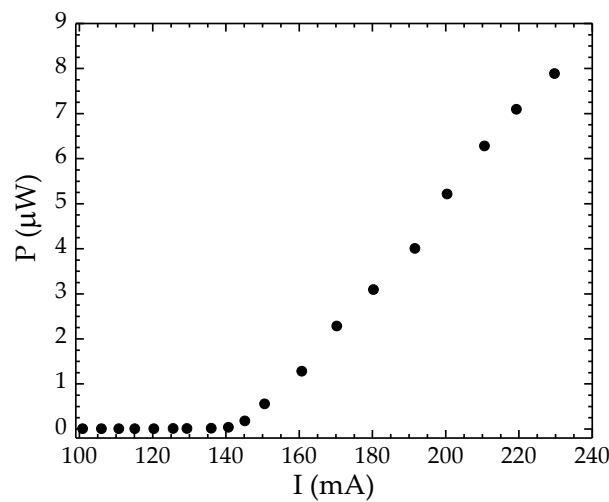
Figure 6.15 – Optical power variations with the drive-in current.

In order to perform torsion measurements, one side of the sensor was introduced in a torsion stage, which had a resolution of 0.5°, while the other side was kept fixed. It was found that both the amplitude and the central wavelength of the laser peak shifted as torsion was applied, for both negative and positive angles. This behavior, illustrated in Fig. 6.16 (a), was due to the rotation of the PM PCF cores.

Starting from 0°, the peak shifted towards longer wavelengths as the torsion angles increased (red shift). Accordingly, by decreasing the angles from 0° to -90°, the laser peak shifted towards shorter wavelengths (blue shift). The laser will emit in a wavelength that corresponds to the maximum response from the combination of the erbium fiber gain curve and of the interferometric filter function, as shown in Fig. 6.16 (b).
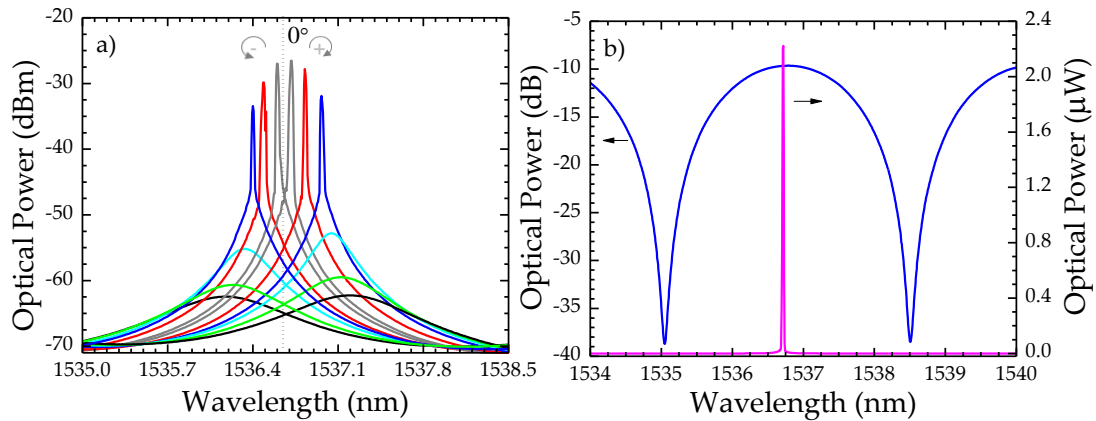
Figure 6.16 – (a) Variation of the laser emission with the applied torsion and (b) interferometric filter spectrum (blue line) and laser spectrum (pink line).

The response of the laser peak wavelength to the applied torsion angle is shown in Fig. 6.17 (a). The experimental data presented a linear behavior in this range, which led to a sensitivity of $-(7.13 \pm 0.05)$ pm/degree. The analysis could also have been done considering the variations of optical power, since the laser emission power varies depending on its wavelength vs. the interferometric filter response. Thus, when the wavelength corresponds to a maximum of the interferometric filter spectrum, a maximum also occurs in the laser peak emission, following the same trend as the filter itself. As the torsion is applied, besides the wavelength shift of the interferometric filter pattern, there is an increase on the filter transmission losses, which is responsible for the decrease in the laser peak power. Eventually, the losses become higher than the gain and the laser ceases to emit (black, blue and green curves in Fig. 6.16. (a)).
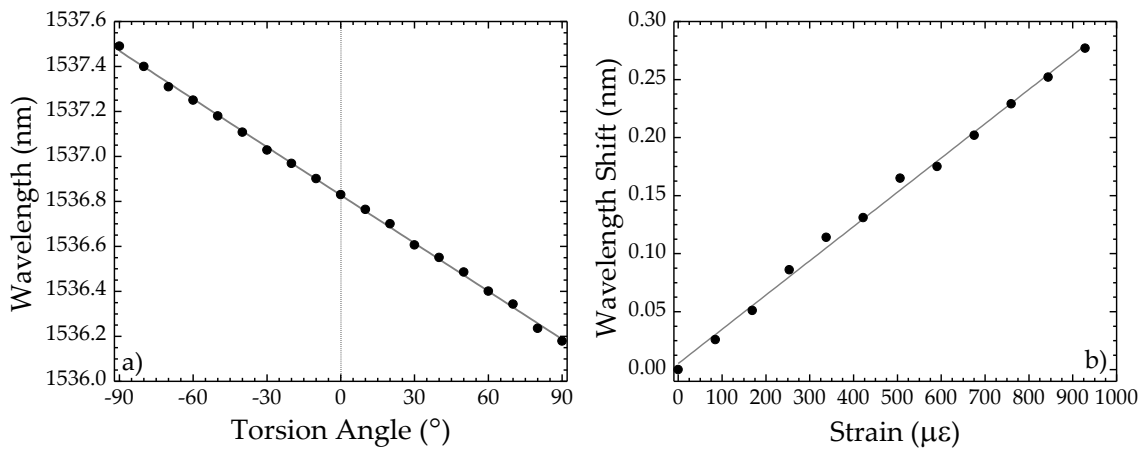
Figure 6.17 – Laser peak wavelength dependence on the applied (a) torsion angle and (b) strain.

Using the same active configuration, the interferometric filter was attached to a translation stage, with a resolution of 0.01 mm, and strain measurements were carried

out over a range of 1000 µε. The results, depicted in Fig. 6.17 (b), follow a linear trend. From the fitting, a sensitivity of only (0.30 ± 0.06) pm/µε was obtained. Besides, it has been reported in the literature that this fiber has a very low sensitivity to temperature (~0.3 pm/°C) [272], meaning that with this configuration it is possible to perform strain and temperature independent torsion measurements.

6.3.4 Final Remarks

In this Chapter two different fiber lasers were proposed to be applied as sensors. The first configuration was based on a post-processed fiber Bragg grating tip. The sensor was firstly characterized as a passive element, where ultra-high strain sensitivity was obtained. Three different approaches were considered for signal processing: one regarding the full-width at half maximum variation with the applied strain; the other regarding the wavelength variation of the whole spectrum, measured at 3 dB; and the third one consisted of tracking one single peak, where an outstanding sensitivity of (127.3 ± 2.4) pm/µε was achieved. The sensor was also tested in temperature, where it exhibited a sensitivity similar to the one of a non-etched fiber Bragg grating. However, the signal processing of this passive sensor is more complex if a commercial interrogation system is used. When incorporated in a fiber laser, the laser peak varied not only in wavelength, but also in integrated power, following the EDFA gain curve. In fact, this was one of the major drawbacks of this configuration, as it is only suitable to be used in small strain ranges. However, the peak did not broaden with strain and the laser did not suffer from mode hopping. Nevertheless, this sensor presents a very high signal-to-noise ratio, being very suitable for applications in remote sensing, and it can also be useful as vibration sensor. It is also possible to use the laser strain sensor with temperature independence, if the optical power variations are considered instead of wavelength variations.

The second configuration consisted of a figure-of-eight fiber laser and had a section of polarization maintaining photonic crystal fiber which acted simultaneously as an interferometric filter and the sensing element. The active sensor was subjected to torsion measurements, and both the peak laser wavelength and the optical power changed over

a range of 180°. Since the filter presents low sensitivity to strain and temperature, in addition to its low cost, ease of fabrication and reliable results, it proves to be a good choice for performing torsion measurements.

Sensors Based on Microspheres
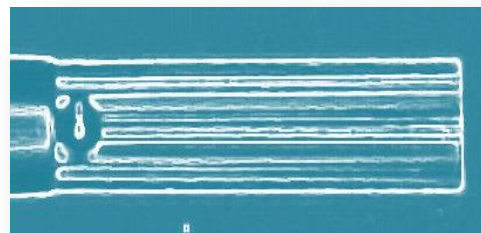
7.1 Introduction

The incorporation of microspheres in optical fiber-based configurations has attracted great attention over the last two decades. The microspheres, due to their physical characteristics and when successfully excited, can be used in a wide variety of practical applications, from sensing to lasing or even tight focusing of light, as it shall be seen next.

Two different mechanisms have been established to explain the propagation of light in microspheres. Under appropriate excitation conditions, they can provide periodical resonances in the transmission spectrum with very high Q-factors[3] and low transmission losses [273]. In this mechanism, based on the whispering gallery modes (WGMs), the light coupled to the microsphere is trapped and propagates in circular orbits close to the surface [274]. To produce the WGMs, it is necessary to couple the evanescent field adequately to and from the microsphere. When several microspheres form a linear chain, besides the tight binding of the WGMs, focusing of light is produced by each microsphere. The focused spot is designated by photonic nanojet and has an elongated shape and sub-wavelength lateral size. The nanojets present in a chain of microspheres produce periodic modes, called nanojet induced modes (NIMs) [275]. In long chains of microspheres (>10), the NIMs are the dominant effect [276]. However, the microspheres must display diameters and refractive indices that enable focusing of light at the shadow surface of the spheres, to ensure the presence of such NIMs.

There are currently several techniques to produce microspheres. The first microspheres produced on a fiber tip were reported in 1973 by Kato and co-workers [277]. A hydrogen-oxygen microtorch was used and microspheres with a maximum diameter of 250 μm were proposed to couple light from a laser into the fiber. A couple of years later, Paek *et al.* suggested the use of a CO_2 laser to produce the hemispherical lens

---

[3] The quality-factor, or Q-factor, is given by $Q = \lambda/\Delta\lambda$, where λ is the wavelength at which the resonance occurs and $\Delta\lambda$ corresponds to the linewidth of the resonant wavelength. The microsphere-based resonators can present Q-factors up to 10^{11} [273].

at the fiber tip [278]. Since then, and besides the CO_2 laser technique [279, 280], different methods have been reported, like flame fusing [274, 281], chemical etching prior to the CO_2 laser [282, 283], or by using a fusion splicer [284-286]. When the microspheres are intended to be used as laser cavities, the deposition of the active medium, by sol-gel or dip-coating techniques, is also employed. The deposition of a polymer at the tapered fiber tip also formed a spherical cavity, used for thermal sensing [287]. The simultaneous production of several Er^{3+}-doped microspheres was reported by Klitzing *et al.*, by using a microwave plasma torch [288]. A similar result can be obtained by using an electric vertical furnace [289-291]. More recently, the microspheres described in the literature became commercially available. These structures present extremely reduced dimensions (can be smaller than 10 μm) and are made of a wide variety of materials [275, 292, 293].

In systems with one microsphere, effective coupling of light to the micro-resonator is very important to ensure the desired high-Q WGMs. The first works reported the use of a prism to launch light onto the microsphere and to collect it to an interrogation system [294-296]. Successful coupling between a side-polished optical fiber and a microsphere was reported in 1995 [297, 298]. A couple of years later, Knight *et al.* used a fiber taper to excite the WGMs [274]. In a different approach, Ilchenko *et al.* placed a microsphere on top of an angle polished fiber tip [299]. Among these designs, the most popular and still currently used one is the fiber taper-based configuration. It is easy to manufacture, to handle and can provide very good conditions to study different types of interactions from single-atom detection [300] to optomechanics [301, 302]. More recently, a new scheme to excite WGMs has been proposed with the microspheres incorporated inside a microstructured optical fiber [293], and inside a microtube [303]. In both configurations, the input and/or the output sub-systems were located outside the fiber, requiring bulk optics to perform the measurements. In a different perspective, Wang *et al.* proposed the use of a thin wall capillary coupler to excite and interrogate the WGMs [304].

The configurations based on WGMs have been used as optical fiber sensors with applications in biosensing [305], temperature sensing [306] and radiation pressure [307], among others. Additionally, when doped with lanthanide elements, the microspheres

can be used as micro-lasers, where large free-spectral range and single mode operation are easily achievable [302].

Regarding the propagation of photonic nanojet induced modes, it has been theoretically and experimentally demonstrated using polystyrene [275, 276, 308] and sapphire [309] microspheres. Both materials present high refractive index, which when combined with appropriate dimensions and an optical source in the UV-VIS region allowed the transmission of light along chains of microspheres (more than 80 microspheres) [276]. These chains display very low propagation losses and the focusing properties show great potential for different applications, such as microprobes for biomedical optical spectroscopy [276], ophthalmic laser surgery [292], or enhancement of Raman scattering [310]. When the transmission spectrum is acquired, Fabry-Perot-like fringes are observed, even in the case of a high number of microspheres [276].

In this Chapter, two different approaches are presented for optical fiber sensing. The first one is a Mach-Zehnder type interferometer constituted by an array of microspheres produced in standard single mode fiber. Several samples are fabricated by splicing microspheres in series and producing an array. In this case, the light propagation occurs inside the whole structure. The second approach consists of a Fabry-Perot interferometer obtained by introducing microspheres inside a hollow-core silica tube. The sensing head is tested in temperature after inserting each microsphere.

7.2   Silica Microspheres Array Sensor

The sensing structure explored in this Section is based on an array of microspheres manufactured using a commercial splicing machine and incorporated in a standard single mode fiber (SMF). The sensors were tested in strain and temperature.

7.2.1   Theoretical Considerations

The dimensions of the microspheres here considered are much larger than the wavelength of the optical source, thus, geometrical optics can be used to explain the structure behavior, in a first approximation [209]. The optical path difference of light

travelling in the microspheres gives rise to an interferometric behavior, and to understand its basic characteristics a ray-tracing analysis was employed using the ZEMAX SE optical design software. The microspheres were simulated as ball lenses of fused silica, with refractive index 1.44402 at 1550 nm. It was also considered that the object numerical aperture was the same as in the SMF, translating in the divergence of the beam observed in Fig. 7.1. The simulations were performed as a first approach and did not take the polarization of light into account. Due to the broadening of the fiber in the region close to the first microsphere, the light seems to exit a point-like source (core of the SMF fiber) located before the microsphere (point f_1 in Fig. 7.1). As light passes through the first microsphere, the beam will diverge, whereas in the second microsphere, there will be a convergence of the beam. For the case of the 2-microspheres sensor, light will be recoupled in the SMF core region. Thus, an interference pattern obtained in transmission (discussed in Section 7.3.2) will be due to the optical path difference of light that travels from point f_1, associated with the first microsphere, to the exit fiber core connected to the second microsphere. Therefore, as illustrated in Fig. 7.1 (a), a Mach-Zehnder type interferometric pattern is to be expected.
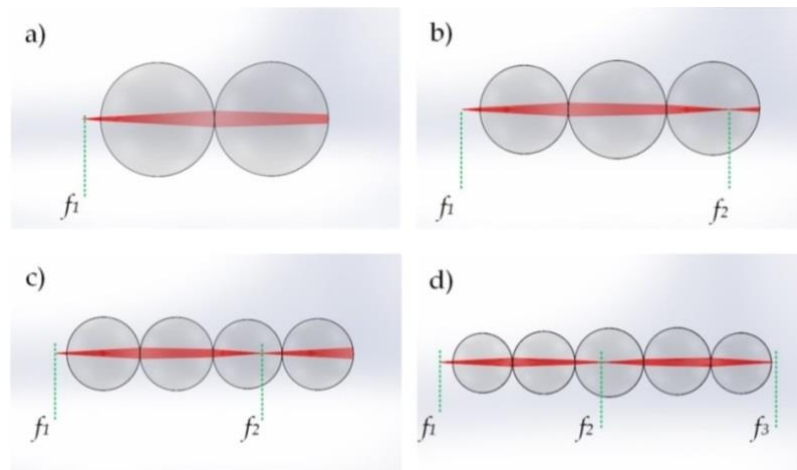
Figure 7.1 – Microspheres array sensors modeling using ZEMAX SE, considering (a) 2 microspheres, (b) 3 microspheres, (c) 4 microspheres and (d) 5 microspheres. The focal points f_1, f_2 and f_3 for each configuration are also shown (when applicable).

With the addition of a third microsphere the light will converge on its inside, at a point indicated by f_2 in Fig. 7.1 (b - d). Notice, in Fig. 7.1 (b), that there is further divergence of the beam after f_2. Nevertheless, it will not have much influence on the power coupling to the output SMF since it is very close to the edge of the microsphere.

However, when a fourth microsphere is introduced, the beam will broaden once more, originating some change on the amount of optical power that propagates down the exit fiber. The inclusion of a fifth microsphere translates into a convergence of the beam inside the third microsphere (f_2), and divergence once again between the third and fourth microspheres. Close to the edge of the fifth microsphere, convergence will occur once again, at the point indicated by f_3. The three points, f_1, f_2 and f_3, are associated with light focusing, therefore can be identified as focal points.

7.2.2 Sensor Design and Spectral Characteristics

The first step to make the proposed sensor consisted of the fabrication of the microspheres at the tip of a SMF, using a splicing machine (FITEL S182PM) in the manual program. The arc power was 110 arb. units (pre-defined by the manufacturer), the pre-fuse time was 240 ms and the arc duration was of 2000 ms. The high power of the electric arc discharge was transferred to the fiber tip, which partially melted. The fiber acquired a spherical shape due to surface tension.

The fiber was firstly cleaved and inserted in the splice machine. It was then moved forward ~125 µm, ensuring that the arc discharge occurred in the SMF region. The arrows represented in the first photograph of Fig. 7.2 illustrate the position of the electrodes relative to the fiber. After each arc discharge a photograph was taken for posterior analysis. The first eleven results are shown in Fig. 7.2.
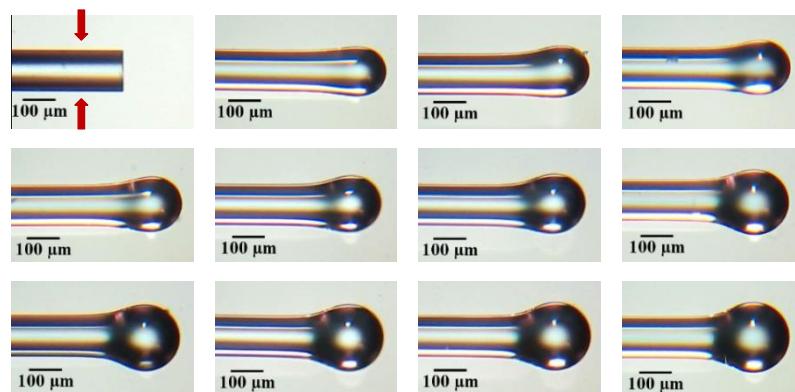
Figure 7.2 – Microphotographs of the microspheres manufactured using the splicing machine. Each photo was taken after one electric arc discharge.

The microsphere diameter was estimated from the microscope images, with a measurement uncertainty of ± 3 µm, and its evolution is depicted in Fig. 7.3. The

measurement was carried out perpendicularly to the SMF length. The growth is stronger at the beginning of the fabrication (first seven arc discharges). From that point on, the diameter increase becomes less pronounced, as can be verified in Figure. With this fabrication method, after a certain amount of electric discharges, the microsphere growth tends to stabilize. A final diameter of ~240 μm was attained, after 18 electric discharges. The sensing structures developed present a mean diameter of ~230 μm.
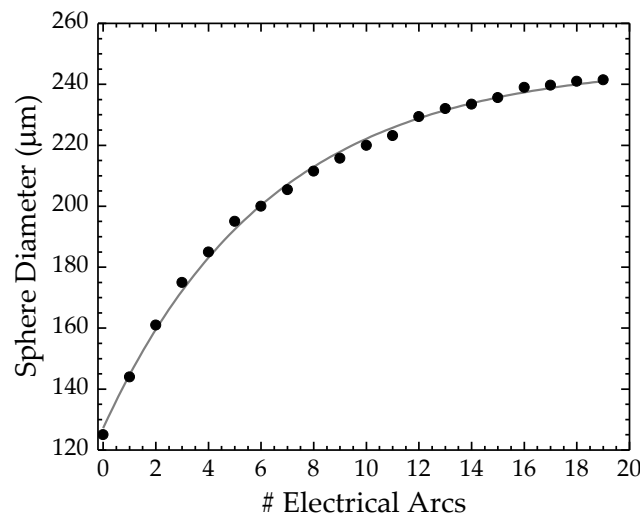
Figure 7.3 – Dependence of the sphere diameter on the number of electric arc discharges.

Four different structures were produced by connecting from 2 up to 5 microspheres in series. The microscope images of each sensor are shown in the insets of Fig. 7.4. The 2-microspheres sensor, shown in the inset of Fig. 7.4 (a), was fabricated by fusion splicing two microspheres that were produced separately. This fusion was done using the same program of the splicing machine, with the two microspheres aligned, and a total of 5 electric arc discharges were applied to ensure the mechanical stability of the sensor without collapsing the two microspheres. The procedure to fabricate the other sensors was similar. First, the microspheres were produced separately. Afterwards, two microspheres were fusion spliced as previously described. A cleave was then made after the second microsphere. This intermediate structure was placed once again in the splicing machine and a few electric arc discharges were applied to re-shape it into the two spherical shapes required. This structure was then spliced to a third microsphere fiber tip, completing the 3-microspheres sensor. The previous steps were repeated to produce the 4- and 5-microspheres samples.

The sensors spectral response was obtained by connecting the sample between a broadband optical source and an optical spectrum analyzer (OSA), in a typical transmission setup. The optical source had a bandwidth of 50 nm and it was centered at 1550 nm. The transmission readings were done with a resolution of 0.2 nm. The spectrum of each sensor is shown in Fig. 7.4. The interferometric behavior obtained was due to the optical-path difference of light travelling inside the microspheres, as considered in Section 7.2.1. The channeled spectrum behavior obtained for the 2-microspheres sensor resulted from a Mach-Zehnder type interferometer, consistent with the analysis previously described. When further microspheres are integrated into the chain, there are more possibilities for different propagation lengths from the input SMF to the output one. Therefore, additional waves are generated, with non-negligible amplitude, that add together with the two main waves, originating an interference pattern with an envelope modulation. This effect becomes more pronounced when the number of these additional waves increases as a consequence of cascading an increasing number of microspheres, resulting in a multi-wave interferometric behavior.
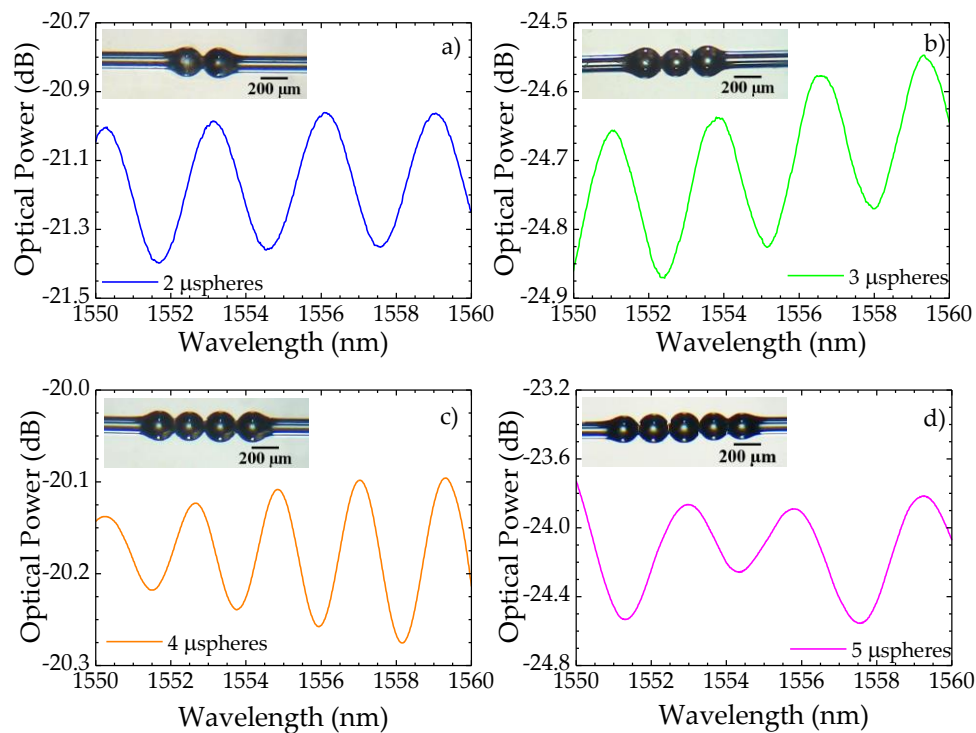
Figure 7.4 – Channeled spectra of light that exits the sensing heads with (a) 2 microspheres, (b) 3 microspheres, (c) 4 microspheres and (d) 5 microspheres.

7.2.3   Experimental Results

The sensors were held out in a support structure on one end and attached to a translation stage, with a resolution of 0.01 mm, on the other. Strain measurements were carried out over a range of 750 µε, by tracking one of the peaks of the channeled spectrum. The response, shown in Fig. 7.5, was linear in all cases and the sensitivities obtained through the fitting curves are gathered in Table 7.1.

Table 7.1 – Strain sensitivity obtained for each sensor.

No. of Microspheres	Sensitivity (pm/µε)
2	-0.87 ± 0.01
3	**-1.83 ± 0.05**
4	-0.44 ± 0.01
5	**-1.31 ± 0.04**
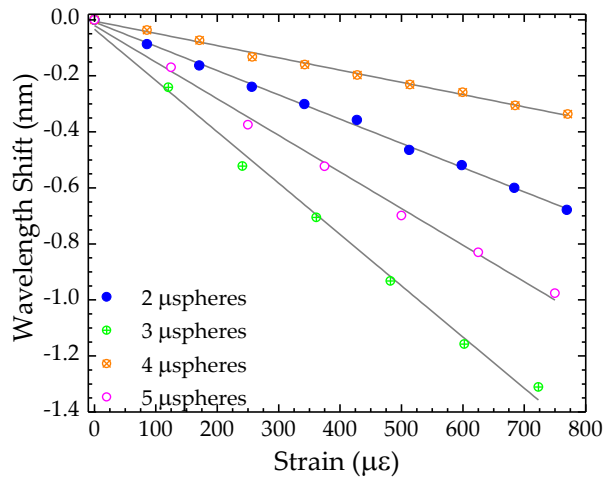
Figure 7.5 – Sensors response to applied strain.

These results seem to indicate that the sensitivity is a function dependent on the number of microspheres being even or odd. However, in all cases, as strain was increased, a shift towards shorter wavelengths (blue shift) was noticed. This was a surprising result, considering that the normal tendency is to observe a red shift, since the interferometric path imbalance increases as the deformation gets larger. A preliminary explanation was oriented to admit the dominance of the elastooptic effect relatively to the change in the optical path (expansion effect [185]). However, the contact area between the microspheres is small, which means that the deformation in those regions may be substantial. Thus, the dominance of the elastooptic effect over the expansion component is unlikely to occur. Other mechanisms must be taken into account to explain the behavior observed, and so far there is no definite explanation.

The sample with 3-microspheres was also tested against temperature variations. It was placed inside a tubular oven, in a centered position, and it was kept straight. Temperature measurements were carried out in a range of 200 °C, with a resolution of

0.1 °C. A linear behavior was observed, as depicted in Fig. 7.6, and a sensitivity of (18.4 ± 0.6) pm/°C was attained. The wavelength shift towards longer wavelengths indicates that the thermal expansion of the silica microspheres is the dominant effect.
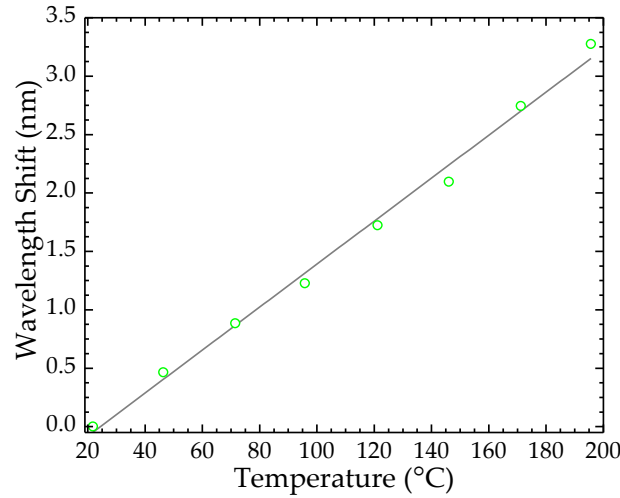
Figure 7.6 – Response of the 3-microspheres sample to temperature variation.

7.3   Fabry-Perot based on Array of Soda-Lime Glass Microspheres

The configuration discussed in this Section is based on an array of soda-lime glass microspheres incorporated inside a hollow core silica tube. The sensors are tested for temperature changes.

7.3.1   Theoretical Considerations

The microsphere dimensions are smaller than the ones presented in the previous configuration, however still large enough for the analysis to be within the limits of validity of geometrical optics. Considering the scheme presented in Fig. 7.7, the focal length, f, is measured from the center of the sphere, where the extensions of the entering and exiting ray meet [311]. This parameter is related to the refractive index of the sphere, n, and its radius, r, by Eq. 7.1:

$$f = \frac{rn}{2(n-1)}.$$

(7.1)

Considering the microsphere parameters given by the manufacturer, $r = 26.34$ µm and $n = 1.52$, the focal length for the microspheres used in this work is 38.5 µm. The back

focal length, *bfl*, is determined by the difference between the sphere radius and the focal length.

$$bfl = f - r = \frac{r(2-n)}{2(n-1)}. \tag{7.2}$$

In this case, *bfl* = 12.2 µm. In order to have nanojet induced modes (NIMs), the *bfl* should be close to zero. This only happens when *n* = 2.
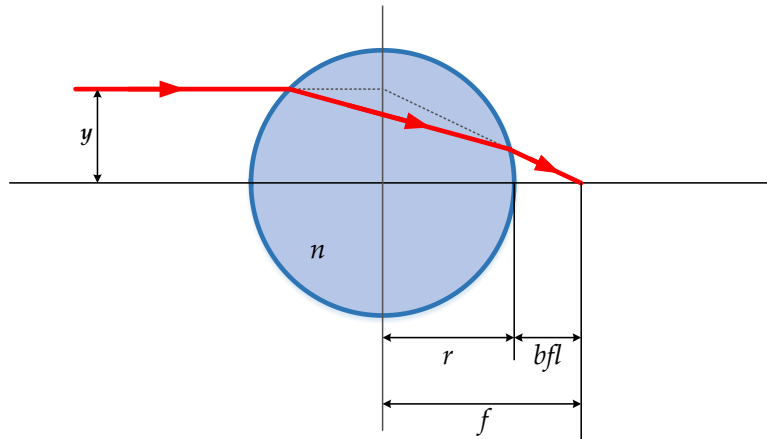
Figure 7.7 – Scheme of the ray tracing through a ball lens. Adapted from [311].

Under certain conditions, it is possible to obtain NIMs for microspheres with low refractive index [312, 313]. However, the lowest value reported was 1.68 RIU, which is still much higher than the refractive index of silica.

7.3.2   *Sensor Design and Spectral Characteristics*

The hollow core structure used to support the soda-lime glass microspheres was the same as in Section 5.3. The presence of the four rods increased slightly the electrostatic forces between the microspheres and the support structure, enabling a higher stability of the sensor.

The sensing structure was fabricated by fusion splicing a section of hollow core silica tube with four rods to a SMF, using the manual program of the splicing machine. The fibers were positioned with a lateral offset relative to the electrodes to prevent the collapse of the hollow structure, following the same procedures as described in Section 3.3.1. The support structure was cleaved to the desired length, of the order of several hundred micrometers, and it was attached to a vertical platform that was placed under a

5× magnifying lens. The microspheres were inserted, one by one, with the aid of a built on purpose fiber taper and a short section of a 30 µm thick platinum wire. The microspheres used in the experiment were made of soda-lime glass, with an average diameter of (52.68 ± 0.90) µm and a refractive index of 1.51-1.52 RIU. These parameters were supplied by the manufacturer, Whitehouse Scientific.

The sensing structure was interrogated in a reflection setup constituted by a broadband optical source (bandwidth 100 nm, centered at 1570 nm), an OSA with a resolution of 0.1 nm, and an optical circulator, according to the scheme in Fig. 7.8.
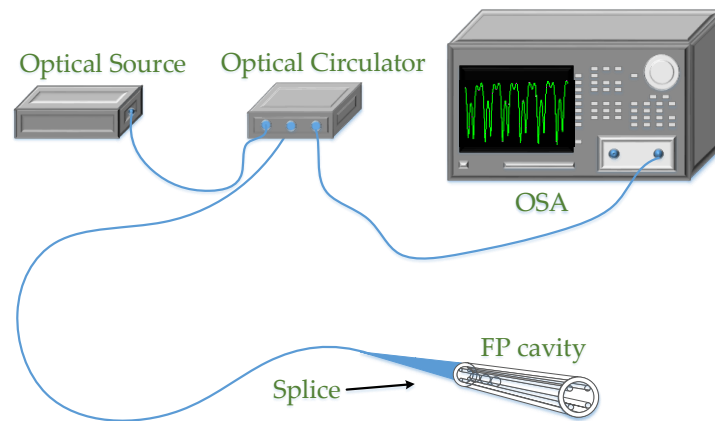
Figure 7.8 – Scheme of the experimental setup.

The reflection spectrum obtained from the support structure, without microspheres, is shown in Fig. 7.9 (a). There is an interferometric behavior with very low visibility, ~1%. The interference has the same origin as in other similar configurations previously studied (see Chapter 3). The first reflection occurs at the SMF/silica tube interface. Some of the light is transferred to the silica tube and a second reflection occurs at its end face. This light is recoupled once again at the SMF. When a first microsphere is placed inside the silica tube the visibility increases to 62.3 % (see Fig. 7.9 (b)). A two-wave interferometric behavior is spectrally observed. In this case, light exiting the SMF will interact with the microsphere and the reflections occurring at the SMF/microsphere and microsphere/air interfaces constitute the two FP cavity mirrors. From the spectrum it is possible to confirm this statement, as for an effective refractive index of 1.51 RIU and considering the wavelength of two adjacent peaks (*e.g.* 1546.9 nm and 1561.9 nm), the

cavity length is $L_{FP} = 53.4\ \mu m$, which is in good agreement with the microspheres diameter value supplied by the manufacturer.
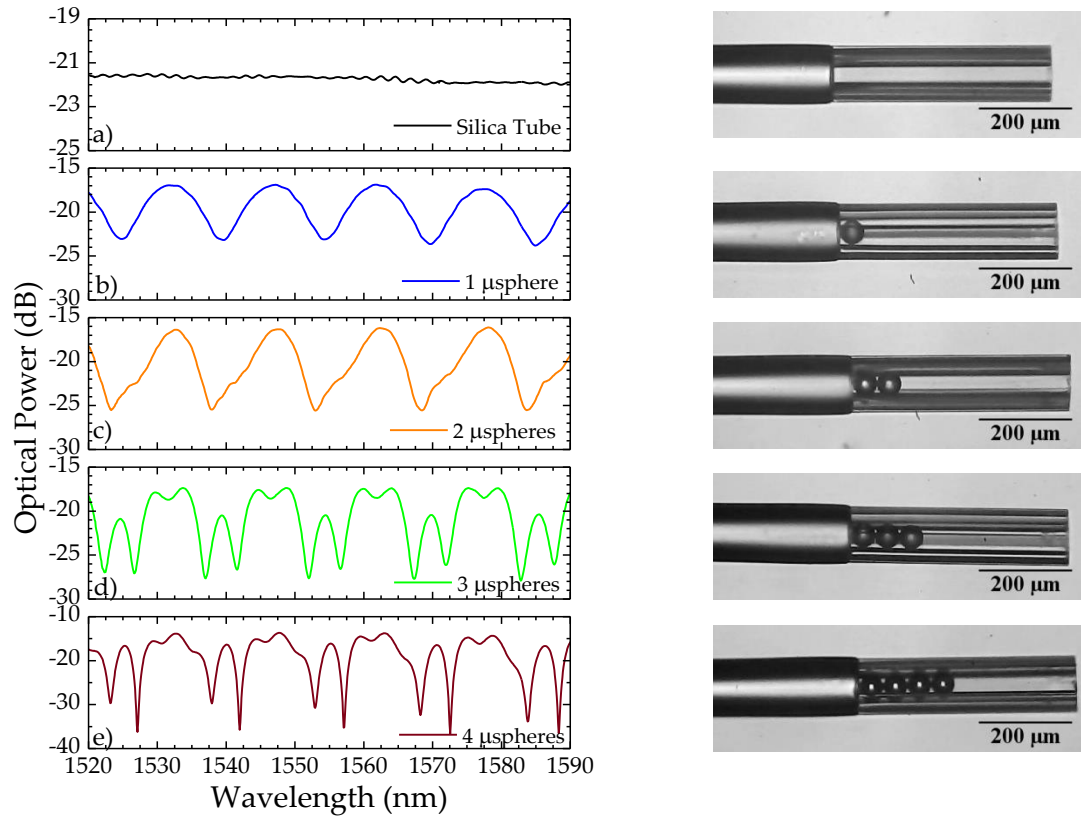
Figure 7.9 – (left) Spectra of the sensing heads tested. (right) Microphotographs of the characterized sensors.

The alignment of the microspheres relative to the core of the SMF and relative to each other is of utmost importance to obtain a spectrum with high visibility. In the case of the two microspheres sample it is not possible to distinguish the interference arising from each microsphere (see Fig. 7.9. (c)). However, the 3-microspheres sensing head spectrum, presented in Fig. 7.9 (d), shows the presence of a periodic pattern with three distinct peaks, corresponding to the three microspheres. The inclusion of a fourth microsphere increased the number of peaks observed in the periodic pattern (Fig. 7.9 (e)). The microscope images of each sensor are also presented in Fig. 7.9, on the right side. The overall visibility increased with the number of microspheres, as can be seen in Fig. 7.10. The 4-microspheres sample was illuminated with a He-Ne laser and a microphotograph, shown in the inset in Fig. 7.10, was taken where the FP cavity mirrors at each interface can be well identified.
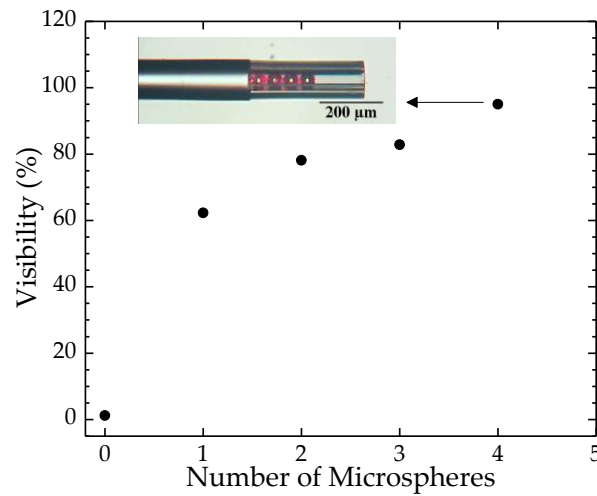
Figure 7.10 – Dependence of the spectral visibility on the number of microspheres. Inset: Microphotograph of the 4-microspheres sample when illuminated with a He-Ne laser.

7.3.3 Experimental Results

The sensing structure was subjected to temperature variations over a range of ~100 °C. The experiment was repeated each time one additional microsphere was inserted in the silica tube. The sensing head was placed inside a tubular oven, in a centered position. The temperature readings had a resolution of 1 °C. The sensors responses are shown in Fig. 7.11. In all cases, the behavior was non-linear and the experimental data were adjusted by second order polynomials. The results are gathered in Table 7.2.
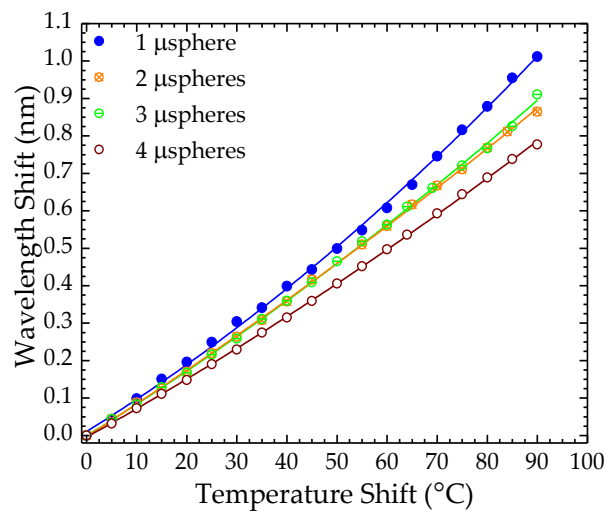
Figure 7.11 – Wavelength variation with temperature.

Table 7.2 – Temperature sensitivity obtained for each sensor. λ corresponds to the wavelength, in nm, and T to the temperature, in °C. The correlation coefficient, r^2 is also shown.

No. of Microspheres	Polynomial Fitting	r^2
1	$\lambda = (0.03 \pm 0.01) \times 10^{-5} T^2 + (8.28 \pm 0.32) \times 10^{-3} T + (10.92 \pm 6.13) \times 10^{-3}$	0.99902
2	$\lambda = (1.24 \pm 0.17) \times 10^{-5} T^2 + (8.61 \pm 0.16) \times 10^{-3} T - (2.77 \pm 2.98) \times 10^{-3}$	0.99971
3	$\lambda = (1.90 \pm 0.24) \times 10^{-5} T^2 + (8.27 \pm 0.22) \times 10^{-3} T - (0.83 \pm 4.31) \times 10^{-3}$	0.99938
4	$\lambda = (1.47 \pm 0.12) \times 10^{-5} T^2 + (7.47 \pm 0.12) \times 10^{-3} T - (4.44 \pm 2.24) \times 10^{-3}$	0.99979

Although the second order polynomial is the curve that best represents the behavior of this sensing structure, a linear fit was also applied to the experimental results. The coefficient of determination, r^2, decreased from a mean value of 0.9995 to 0.9970, which is still very close to the unity. The samples with 1 and 3 microspheres presented a linear sensitivity of (11.13 ± 0.20) pm/°C and (9.95 ± 0.12) pm/°C, respectively. In turn, the devices with 2 and 4 microspheres exhibited a linear sensitivity of (9.74 ± 0.08) pm/°C and (8.79 ± 0.09) pm/°C, respectively. An interpretation can be developed by recalling Eq. 3.17,

$$\frac{1}{\lambda}\frac{\partial \lambda}{\partial T} = \frac{1}{n_{eff}}\frac{\partial n_{eff}}{\partial T} + \frac{1}{L_{FP}}\frac{\partial L_{FP}}{\partial T}, \tag{7.3}$$

where $\partial n_{eff}/\partial T$ and $\partial L_{FP}/\partial T$ are the thermo-optic coefficient and the thermal expansion coefficient of the microspheres, respectively. Since the microspheres are constituted of soda-lime glass, these parameters are 2.06×10^{-6} /°C and 7.75×10^{-6} /°C, respectively [314]. For the case of a single microsphere sensor, dividing its linear sensitivity by the operation wavelength (1540.55 nm) gives 7.22×10^{-6} /°C which is in very good agreement with the microspheres thermal expansion coefficient. Thus, in this case the thermal expansion is the dominant effect when the sensor is subjected to temperature variations. However, for the other sensors, when the sensitivity is divided by the operation wavelength, the values obtained are lower $(6.29 \times 10^{-6}$ /°C, 6.41×10^{-6} /°C and 5.66×10^{-6} /°C for the 2-, 3- and 4-microspheres sensor, respectively), indicating that other effects arise when there is an increase of the structure complexity. By increasing the number of microspheres, the number of fringes increases, as a consequence of the cavity length increase. Thus, according to Eq. 7.3, the contribution of the thermal expansion coefficient will be smaller, which is in agreement with the values obtained. The response

of the sensor clearly depends on the number of microspheres and the results lead to believe that sensors with and even number of microspheres are less sensitive than sensors with and odd number of microspheres. To ensure the validity of this observation, a sensor with five microspheres should be produced and subjected to the same experimental conditions. This matter will be further investigated in the near future.

7.4 Final Remarks

In this Chapter, two different configurations based on microspheres were proposed for sensing. The first one was constituted by an array of microspheres incorporated in a SMF, manufactured using a splicing machine. Four different samples were characterized in terms of strain, and exhibited a negative response (blue shift of the interferometric pattern). The reasons behind such behavior are still not fully understood. Besides, the sensors response showed a dependence on the number of microspheres being even or odd. This sensor was also tested in respect to temperature.

The second configuration was obtained at the tip of an optical fiber, by introducing commercially available soda-lime glass microspheres inside a hollow core silica tube. A Fabry-Perot cavity was obtained, with a spectral response dependent on the number of microspheres. Four devices were tested in terms of temperature response and exhibited non-linear behavior. In this configuration, and with the results obtained so far, it is probable that better responses are achieved from sensors with an odd number of microspheres. This is a matter for further investigation.

This last structure has a great potential for sensing applications. It can be used to perform pressure or refractive index measurements, and with adequate post-processing through chemical etching or focused ion beam, it can be used to measure different parameters such as flow or magnetic fluids. The employment of different microspheres, with higher refractive index, can also enhance the sensor performance. Besides, with a different experimental setup, whispering gallery modes can be detected and the device can be incorporated in a laser configuration.

CHAPTER EIGHT

Final Conclusions and Future Work

Final Conclusions and Future Work

Considering an overall perspective, the work developed in this PhD was broadband, both on the number of sensing configurations and applications. New fiber designs were explored in different contexts. Some were post-processed, by means of chemical etching or by writing periodic patterns through excimer laser and femtosecond laser, or even by producing microspheres with the aid of a fusion splicer.

The majority of sensors presented in this Thesis were based on the Fabry-Perot (FP) interferometer. For that reason, it was essential to have an overview of what was published in the field. This state-of-the-art was done on the second Chapter, focusing in the configurations, the applications and the sensitivities obtained so far. It also evidenced that even though the first papers were published more than thirty years ago, this is still a hot topic, as the number of publications continues to grow. This indicates that the overview is not complete and should be expanded in the years to come.

The FP configurations developed in the third and fourth Chapter were microcavities at the tip of a single mode optical fiber. The focus on the third Chapter was on gas sensing applications and two different hollow core fibers were used in a diaphragm-free cavity. The results were surprising and some of them are still not fully understood. There was a clear influence of the cavity shape and physical dimensions on the pressure response. However, further studies are required to understand why smaller cavities present higher sensitivities than the larger ones. Besides, the study of the sensors responses to other gases, such as methane, carbon monoxide and dioxide, hydrogen and sulphur species should be performed, due to the vital importance in many industries.

The fourth Chapter was focused on the post-processing of a double-clad optical fiber. The inner cladding was removed through chemical etching, exposing the core to the environment. However, the core was still protected by the outer cladding, enhancing the mechanical stability of the sensor. The diaphragm-free configuration was only subjected to temperature variations. The inscription of a fiber Bragg grating (FBG) on this tip could translate in a high sensitivity refractometer, and should be explored in the future. The cavity with a diaphragm, on the other hand, revealed different responses to temperature

in water and in air, when the diaphragm was thin enough. This idea of post-processing fibers that did not guide light, by means of chemical etching, could be taken forward with new fiber designs and finding suitable applications.

On the fifth Chapter three different configurations were proposed for the measurement of strain. The FP cavity based on a hollow-core ring photonic crystal fiber presented the highest sensitivity to strain reported, by the time it was published. The remaining two configurations were used to measure strain at high temperatures. Further studies should be done to better understand the strain sensitivity obtained with a FP cavity. Besides, if the high-temperatures strain sensor ought to be considered for a real application, annealing tests with a longer duration should be performed, to allow the stabilization of the structure.

Chapter 6 presented the ability of using the same fiber section as a filter in a laser cavity and the sensing element itself. The figure-of-eight fiber laser was characterized in strain and torsion. An etched FBG fiber tip was characterized as a passive and an active sensor. Ultra-high sensitivity to strain was achieved with this sensing element, in both cases. The field of fiber laser sensors, namely when using microlasers, is still little explored by the scientific community, and can be a very interesting area to proceed with the fiber sensors-based investigation.

The employment of microresonators, such as the microspheres has such a huge potential, both as lasers and as sensors. The incorporation of a microsphere inside the optical fiber makes the sensor easy to handle. However, to prevent contaminations, a clean environment is needed. Two different sensors based on microspheres were developed and characterized in this Thesis. The first, a Mach-Zehnder interferometer, was obtained by fusion splicing an array of microspheres in series. Many different configurations can be explored from this. For example, the use of hollow core fibers to produce hollow core spheres, splicing the spheres with lateral offsets, or even microspheres with different dimensions. The mechanisms behind the strain behavior should also be better understood. This configuration is rather complex, and further studies are required, mainly by computational modelling. The preliminary results

obtained with the FP cavities based on soda-lime glass microspheres placed inside a hollow structure presented in the seventh Chapter point out that these structures have a huge potential to be applied as fiber sensors. Some guidelines for future work would be to use these cavities to measure other parameters, such as gas pressure or refractive index; using high-refractive index microspheres (higher than soda lime glass) instead of the soda-lime glass ones; and considering the application of hollow structures that would be able to guide light. With this enhancement, the microspheres would be protected and would be able to perform passive and active sensing, under the appropriate conditions, opening a new field in optical fiber sensing.

Appendices

Appendix I – Fabrication of a Double Clad Optical Fiber

The preform was obtained by the modified chemical vapor deposition (MCVD) method. In a simple way, gas mixtures with the required compounds are injected in a quartz silica tube which is continuously rotating. On the outside of this tube there is a burner that can operate at temperatures above 2000 °C. This burner moves along the length of the tube and the layers of silica/ phosphorous-doped silica are gradually deposited, as shown in Fig. 9.1 (a), according to the following steps:

1. Cleaning and refining of the silica tube at temperatures of 1900 °C and 1980 °C (outer cladding);

2. Deposition of 22 P_2O_5-doped SiO_2 layers at a temperature of 1630 °C (inner cladding);

3. Deposition of 3 SiO_2 layers at a temperature of 1910 °C (fiber core);

4. Collapsing 4 times at temperatures of 2230 °C, 2250 °C, 2160 °C and 2000 °C

Figure 9.1 (b) shows the preform being collapsed, in the fourth step. The details of the whole process are in [315].
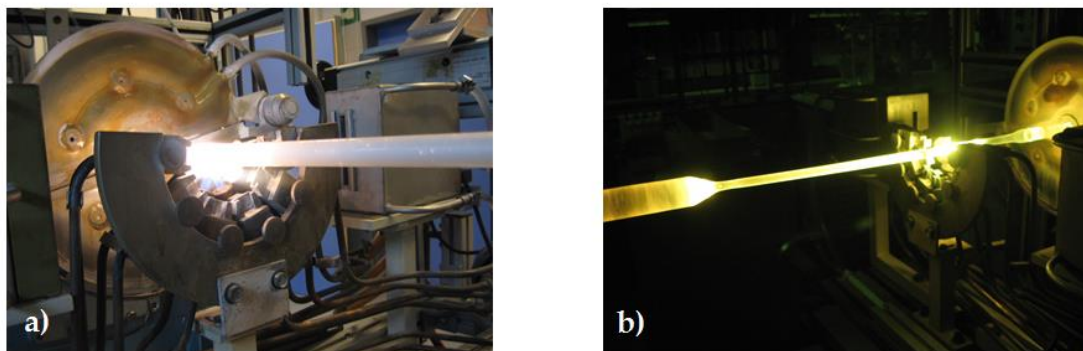
Figure 9.1 – Preform fabrication using the MCVD technique, evidencing (a) the burner that moves along the tube when the layers are being deposited and (b) when the structure is being collapsed at extremely high temperatures.

During the MCVD process there was an unusual behavior of the dopants and the final structure was not perfectly symmetric, as would have been expected. Nevertheless, the fiber was drawn, by locally heating the fiber preform. Initially, the neck-down region of the preform is heated up until it softens and it starts to be pulled down by the action

of gravity (Fig. 9.2 (a)). This molten section of the preform is analyzed by a diameter controller, after which it is cut, leaving the thin fiber to be drawn. The drawing temperature was ~1800 °C. Besides temperature, pressure and drawing speed can also affect the final structure, so these parameters must be controlled throughout the entire process. However, given the preform dense structure, in this case, the pressure did not play a role. The temperature was constant and set to a value adequate to achieve moderate tensile forces in order to prevent fiber breakage. Therefore, the drawing force was continuously recorded and showed values ~0.2 N. The preform feed rate was 0.78 mm/min and the drawing speed was adjusted between 4.2 - 4.5 m/min to reach a constant fiber diameter of 125 μm. The fiber was coated with a single layer UV cured acrylate coating. The diameter of the coated fiber was 230 μm. Figure 9.2 (b) shows the UV curing lamp used to process the acrylate. Finally, the fiber was coiled, using a system of capstans and a drum winder, as shown in Fig. 9.2 (c). A more detailed description of the drawing process is presented in the literature [315].
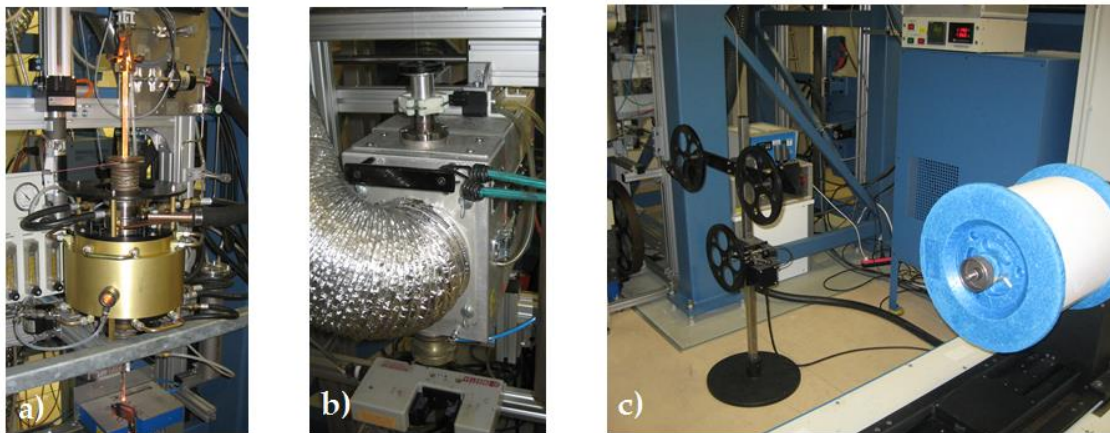
Figure 9.2 – Fiber drawing components: (a) the drawing furnace with the preform, (b) the UV curing lamp and (c) capstan and drum winder.

Appendix II - Point-by-Point Femtosecond Laser FBG Inscription

The experimental setup used to write the fiber Bragg gratings using the point-by-point technique is shown in Fig. 9.3. A mode-locked Yb:YAG laser system, centered at 1026 nm and with a repetition rate of 100 kHz (Amplitude System S-Pulse HP) was used for the generation of sub-500 fs-laser pulses [316, 317]. The work was carried out under a 20× objective lens (Mititoyo M-Plan Apo NIR Series) which had a numerical aperture of 0.4. The effective laser spot diameter was of 2 µm. The samples were placed in a sub-nanometer precision XY air-bearing translational stage with mechanical z-translation (ABL1000, Aerotech). The stages were controlled through a control unit (Aerotech A3200) connected to a personal computer (PC), and a custom made program was developed using G-code commands for the translation stages motion control.
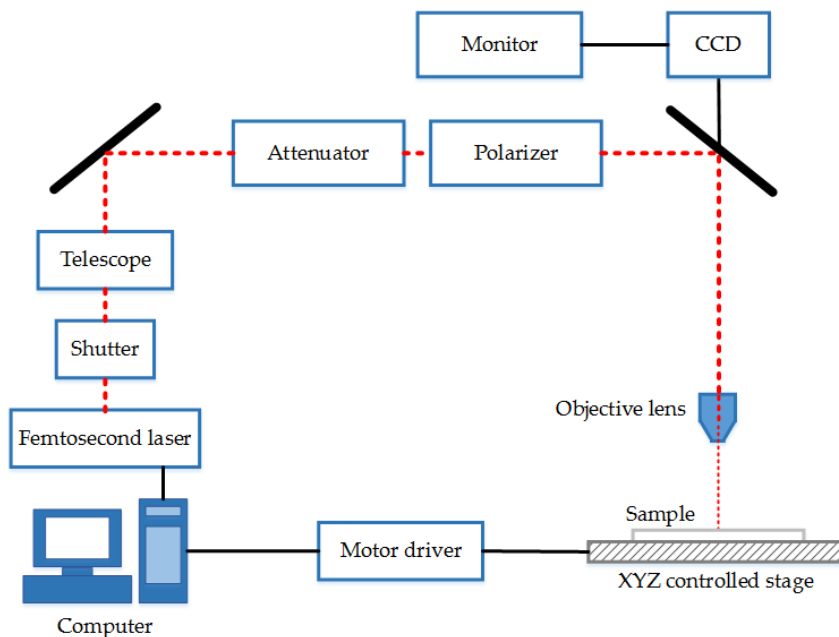
Figure 9.3 – Experimental setup for the femtosecond laser system used to inscribe the fiber Bragg gratings. CCD stands for charged coupled device. Adapted from [317].

A section of ~1 cm of fiber coating was removed and afterwards the fiber was secured to a standard microscope glass slide. In order to compensate the fiber curvature, thus guaranteeing the tight focus of the laser beam during the inscription and improving the visibility on the CCD camera, a droplet of index matching oil was placed on the fiber section without coating. Finally, a cover slip was placed on top of the oil.

Through a controlled motion, the laser was focused on the fiber core, at the beginning of the writing section. As the translation stage acquired the required speed, of 1.071 mm/s, the shutter was opened and the FBG was written on the fiber core. The writing process was monitored in real time connecting the fiber ends to a transmission setup constituted by a broadband optical source and an optical spectrum analyzer.

Appendix III - Interferometric Excimer Laser FBG inscription

The experimental setup used to write the FBGs using the phase-mask technique is shown in Fig. 9.4. It consisted on a KrF excimer laser source from Lambda Physik (Compex150) with a wavelength of 248 nm and a Talbot interferometer [318, 319]. The beam is focused by a cylindrical lens and passes through the phase mask, which acts as a beam splitter. For the FBGs written in this work, a phase mask with a period of 530 nm was used. The split light is then reflected by two rotating mirrors. Depending on the angle of these components, the angle at which light is recombined, θ_{FBG}, changes, allowing the tunability of the Bragg wavelength, λ_B, according to Eq. 9.1 [319]:

$$\lambda_B = \frac{n_{eff}\lambda_{UV}}{\sin\theta_{FBG}} = 2n_{eff}\Lambda, \qquad\qquad (9.1)$$

where n_{eff} is the optical fiber effective refractive index and λ_{UV} is the KrF excimer laser source wavelength and Λ is the grating period. This setup is incorporated in the fiber drawing tower facilities, enabling the simultaneous fiber manufacturing and FBG inscription. The fibers need to be photosensitive in order to achieve high-reflectivity FBGs. This can be obtained by using fibers with a highly-doped core (ca. 18% Ge dopants). However, the setup can also be used independently to the fiber drawing tower. This was the case for the FBGs tested in Chapter 6.
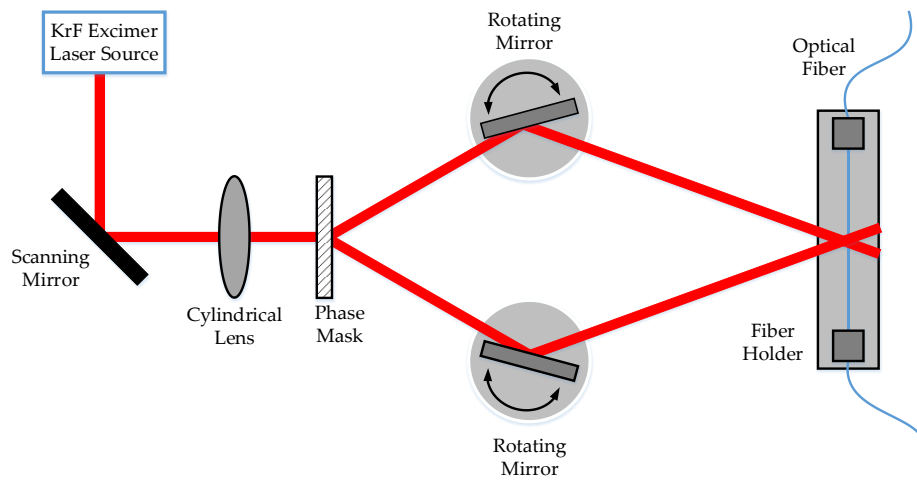
Figure 9.4 – Scheme of the interferometric KrF excimer laser setup. Adapted from [318].

References

References

[1]   Santos, J. L. and Farahi, F., Handbook of Optical Sensors, CRC Press/Taylor & Francis Group, 2015.

[2]   Gerges, A. S., Newson, T. P., Farahi, F., Jones, J. D. C. and Jackson, D. A., *A hemispherical air cavity fiber Fabry-Perot sensor*, Opt Commun, **68**(3), 157-160, 1988.

[3]   Kersey, A. D., Jackson, D. A. and Corke, M., *A simple fiber Fabry-Perot sensor*, Opt Commun, **45**(2), 71-74, 1983.

[4]   Morey, W. W., Meltz, G. and Glenn, W. H., *Fiber optic Bragg grating sensors*, Fiber Optic and Laser Sensors Vii, **1169**, 98-107, 1990.

[5]   Knight, J. C., Birks, T. A., Russell, P. S. and Atkin, D. M., *All-silica single-mode optical fiber with photonic crystal cladding*, Opt Lett, **21**(19), 1547-1549, 1996.

[6]   Huang, Z. Y., Zhu, Y. Z., Chen, X. P. and Wang, A. B., *Intrinsic Fabry-Perot fiber sensor for temperature and strain measurements*, Ieee Photonic Tech L, **17**(11), 2403-2405, 2005.

[7]   Donlagic, D. and Cibula, E., *All-fiber high-sensitivity pressure sensor with SiO2 diaphragm*, Opt Lett, **30**(16), 2071-2073, 2005.

[8]   Rao, Y. J., Deng, M., Duan, D. W., Yang, X. C., Zhu, T. and Cheng, G. H., *Micro Fabry-Perot interferometers in silica fibers machined by femtosecond laser*, Opt Express, **15**(21), 14123-14128, 2007.

[9]   Watson, S., Gander, M. J., MacPherson, W. N., Barton, J. S., Jones, J. D. C., Klotzbuecher, T., Braune, T., Ott, J. and Schmitz, F., *Laser-machined fibers as Fabry-Perot pressure sensors*, Appl Optics, **45**(22), 5590-5596, 2006.

[10]   Kou, J. L., Feng, J., Ye, L., Xu, F. and Lu, Y. Q., *Miniaturized fiber taper reflective interferometer for high temperature measurement*, Opt Express, **18**(13), 14245-14250, 2010.

[11]   Fabry, C. and Perot, A., *Sur les franges des lames minces argentées et leur application à la mesure de petites épaisseurs d'air.*, Ann. Chim. Phys., **12**, 459–501, 1897.

[12]   Cielo, P. G., *Fiber optic hydrophone - improved strain configuration and environmental noise protection*, Appl Optics, **18**(17), 2933-2937, 1979.

[13]   Yoshino, T. and Ohno, Y., Fiber Fabry-Perot interferometers, in: 3rd Int. Conf. on Integrated Optics and Optical Fiber Commun., San Franscisco, CA, 1981.

[14]   Petuchowski, S. J., Giallorenzi, T. G. and Sheem, S. K., *A sensitive fiber-optic Fabry-Perot interferometer*, Ieee J Quantum Elect, **17**(11), 2168-2170, 1981.

[15]   Franzen, D. L. and Kim, E. M., *Long optical-fiber Fabry-Perot interferometers*, Appl Optics, **20**(23), 3991-3992, 1981.

[16]   Yoshino, T., Kurosawa, K., Itoh, K. and Ose, T., *Fiberoptic Fabry-Perot interferometer and its sensor applications*, Ieee J Quantum Elect, **18**(10), 1624-1633, 1982.

[17]   Ohtsuka, Y., *Optical coherence effects on a fiber-sensing Fabry-Perot interferometer*, Appl Optics, **21**(23), 4316-4320, 1982.

[18]   Kist, R. and Sohle, W., *Fiber-optic spectrum analyzer*, J Lightwave Technol, **LT-1**(1), 105-110, 1983.

[19]   Leilabady, P. A., Jones, J. D. C., Kersey, A. D., Corke, M. and Jackson, D. A., *Monomode fiber optic vortex shedding flowmeter*, Electron Lett, **20**(16), 664-665, 1984.

[20]   Beheim, G., *Remote displacement measurement using a passive interferometer with a fiber-optic link*, Appl Optics, **24**(15), 2335-2340, 1985.

[21]   Beheim, G., Fritsch, K. and Poorman, R. N., *Fiber-linked interferometric pressure sensor*, Rev Sci Instrum, **58**(9), 1655-1659, 1987.

[22]   Dakin, J. P., Wade, C. A. and Withers, P. B., *An optical fiber sensor for the measurement of pressure*, Fiber Integrated Opt, **7**(1), 35-46, 1988.

[23] Ito, T., *Precise measurement of the change in the optical-length of a fiber optic Fabry-Perot interferometer*, Appl Optics, **25**(7), 1072-1075, 1986.

[24] Tseng, S. M. and Chen, C. L., *Optical fiber Fabry-Perot sensors*, Appl Optics, **27**(3), 547-551, 1988.

[25] Lee, C. E. and Taylor, H. F., *Interferometric optical fiber sensors using internal mirrors*, Electron Lett, **24**(4), 193-194, 1988.

[26] Farahi, F., Newson, T. P., Jones, J. D. C. and Jackson, D. A., *Coherence multiplexing of remote fiber optic Fabry-Perot sensing system*, Opt Commun, **65**(5), 319-321, 1988.

[27] Lee, C. E., Atkins, R. A. and Taylor, H. F., *Performance of a fiber optic temperature sensor from -200 to 1050 ºC*, Opt Lett, **13**(11), 1038-1040, 1988.

[28] Kersey, A. D., Dorsey, K. L. and Dandridge, A., *Cross talk in a fiber optic Fabry-Perot sensor array with ring reflectors*, Opt Lett, **14**(1), 93-95, 1989.

[29] Maystre, F. and Bertholds, A., *Magneto-optic current sensor using a helical-fiber Fabry-Perot resonator*, Opt Lett, **14**(11), 587-589, 1989.

[30] Lee, C. E., Taylor, H. F., Markus, A. M. and Udd, E., *Optical fiber Fabry-Perot embedded sensor*, Opt Lett, **14**(21), 1225-1227, 1989.

[31] Valis, T., Hogg, D. and Measures, R. M., *Fiber optic Fabry-Perot strain gauge*, Ieee Photonic Tech L, **2**(3), 227-228, 1990.

[32] Farahi, F., Webb, D. J., Jones, J. D. C. and Jackson, D. A., *Simultaneous measurement of temperature and strain: cross-sensitivity considerations*, J Lightwave Technol, **8**(2), 138-142, 1990.

[33] Alcoz, J. J., Lee, C. E. and Taylor, H. F., *Embedded fiber optic Fabry-Perot ultrasound sensor*, Ieee T Ultrason Ferr, **37**(4), 302-306, 1990.

[34] Lee, C. E. and Taylor, H. F., *Fiber optic Fabry-Perot temperature sensor using a low-coherence light source*, J Lightwave Technol, **9**(1), 129-134, 1991.

[35] Murphy, K. A., Gunther, M. F., Vengsarkar, A. M. and Claus, R. O., *Quadrature phase-shifted, extrinsic Fabry-Perot optical fiber sensors*, Opt Lett, **16**(4), 273-275, 1991.

[36] Claus, R. O., Gunther, M. F., Wang, A. and Murphy, K. A., *Extrinsic Fabry-Perot sensor for strain and crack opening displacement measurements from -200 to 900 ºC*, Smart Mater Struct, **1**, 237-242, 1992.

[37] Santos, J. L., Leite, A. P. and Jackson, D. A., *Optical fiber sensing with a low-finesse Fabry-Perot cavity*, Appl Optics, **31**(34), 7361-7366, 1992.

[38] Wang, A., Gollapudi, S., Murphy, K. A., May, R. G. and Claus, R. O., *Sapphire fiber-based intrinsic Fabry-Perot interferometer*, Opt Lett, **17**(14), 1021-1023, 1992.

[39] Belleville, C. and Duplain, G., *White-light interferometric multimode fiber optic strain sensor*, Opt Lett, **18**(1), 78-80, 1993.

[40] Kersey, A. D., Berkoff, T. A. and Morey, W. W., *Multiplexed fiber Bragg grating strain-sensor system with a fiber Fabry-Perot wavelength filter*, Opt Lett, **18**(16), 1370-1372, 1993.

[41] Sirkis, J. S., Brennan, D. D., Putman, M. A., Berkoff, T. A., Kersey, A. D. and Friebele, E. J., *In-line fiber etalon for strain measurement*, Opt Lett, **18**(22), 1973-1975, 1993.

[42] Atkins, R. A., Gardner, J. H., Gibler, W. N., Lee, C. E., Oakland, M. D., Spears, M. O., Swenson, V. P., Taylor, H. F., Mccoy, J. J. and Beshouri, G., *Fiber-optic pressure sensors for internal-combustion engines*, Appl Optics, **33**(7), 1315-1320, 1994.

[43] Hsu, K., Miller, C. M., Kringlebotn, J. T., Taylor, E. M., Townsend, J. and Payne, D. N., *Single-mode tunable erbium-ytterbium fiber Fabry-Perot microlaser*, Opt Lett, **19**(12), 886-888, 1994.

[44] Sorin, W. V. and Baney, D. M., *Multiplexed sensing using optical low-coherence reflectometry*, Ieee Photonic Tech L, **7**(8), 917-919, 1995.

[45] Dorighi, J. F., Krishnaswamy, S. and Achenbach, J. D., *Stabilization of an embedded fiber optic Fabry-Perot sensor for ultrasound detection*, Ieee T Ultrason Ferr, **42**(5), 820-824, 1995.

[46] Sadkowski, R., Lee, C. E. and Taylor, H. F., *Multiplexed interferometric fiber optic sensors with digital signal-processing*, Appl Optics, **34**(25), 5861-5866, 1995.

[47] Ezbiri, A. and Tatam, R. P., *Interrogation of low finesse optical fibre Fabry-Perot interferometers using a four wavelength technique*, Meas Sci Technol, **7**(2), 117-120, 1996.

[48] Beard, P. C. and Mills, T. N., *Extrinsic optical-fiber ultrasound sensor using a thin polymer film as a low-finesse Fabry-Perot interferometer*, Appl Optics, **35**(4), 663-675, 1996.

[49] Kao, T. W. and Taylor, H. F., *High-sensitivity intrinsic fiber-optic Fabry-Perot pressure sensor*, Opt Lett, **21**(8), 615-617, 1996.

[50] Bhatia, V., Murphy, K. A., Claus, R. O., Jones, M. E., Grace, J. L., Tran, T. A. and Greene, J. A., *Optical fibre based absolute extrinsic Fabry-Perot interferometric sensing system*, Meas Sci Technol, **7**(1), 58-61, 1996.

[51] Dorighi, J., Krishnaswamy, S. and Achenbach, J. D., *Response of an embedded fiber optic ultrasound sensor*, J Acoust Soc Am, **101**(1), 257-263, 1997.

[52] Chang, C. C. and Sirkis, J., *Absolute phase measurement in extrinsic Fabry-Perot optical fiber sensors using multiple path-match conditions*, Exp Mech, **37**(1), 26-32, 1997.

[53] Oh, K. D., Ranade, J., Arya, V., Wang, A. and Claus, R. O., *Optical fiber Fabry-Perot interferometric sensor for magnetic field measurement*, Ieee Photonic Tech L, **9**(6), 797-799, 1997.

[54] Wang, T. Y., Zheng, S. X. and Yang, Z. G., *A high precision displacement sensor using a low-finesse fiber-optic Fabry-Perot interferometer*, Sensor Actuat a-Phys, **69**(2), 134-138, 1998.

[55] Fang, J. X., Taylor, H. F. and Choi, H. S., *Fiber-optic Fabry-Perot flow sensor*, Microw Opt Techn Let, **18**(3), 209-211, 1998.

[56] Lawrence, C. M., Nelson, D. V., Bennett, T. E. and Spingarn, J. R., *An embedded fiber optic sensor method for determining residual stresses in fiber-reinforced composite materials*, J Intel Mat Syst Str, **9**(10), 788-799, 1998.

[57] Du, W. C., Tao, X. M. and Tam, H. Y., *Fiber Bragg grating cavity sensor for simultaneous measurement of strain and temperature*, Ieee Photonic Tech L, **11**(1), 105-107, 1999.

[58] Schmidt, M. and Furstenau, N., *Fiber-optic extrinsic Fabry-Perot interferometer sensors with three-wavelength digital phase demodulation*, Opt Lett, **24**(9), 599-601, 1999.

[59] Arregui, F. J., Liu, Y. J., Matias, I. R. and Claus, R. O., *Optical fiber humidity sensor using a nano Fabry-Perot cavity formed by the ionic self-assembly method*, Sensor Actuat B-Chem, **59**(1), 54-59, 1999.

[60] Liu, T. and Fernando, G. F., *A frequency division multiplexed low-finesse fiber optic Fabry-Perot sensor system for strain and displacement measurements*, Rev Sci Instrum, **71**(3), 1275-1278, 2000.

[61] Katsumata, T., Haga, Y., Minami, K. and Esashi, M., *Micromachined 125 μm diameter ultra miniature fiber-optic pressure sensor for catheter*, Trans. Inst. Electron. Commun. Eng. Jpn., **120-E**(2), 58-63, 2000.

[62] Jiang, M. Z. and Gerhard, E., *A simple strain sensor using a thin film as a low-finesse fiber-optic Fabry-Perot interferometer*, Sensor Actuat a-Phys, **88**(1), 41-46, 2001.

[63] Tsai, W. H. and Lin, C. J., *A novel structure for the intrinsic Fabry-Perot fiber-optic temperature sensor*, J Lightwave Technol, **19**(5), 682-686, 2001.

[64] Dahlem, M., Santos, J. L., Ferreira, L. A. and Araujo, F. M., *Passive interrogation of low-finesse Fabry-Perot cavities using fiber Bragg gratings*, Ieee Photonic Tech L, **13**(9), 990-992, 2001.

[65] Chen, Y. C. and Taylor, H. F., *Multiplexed fiber Fabry-Perot temperature sensor system using white-light interferometry*, Opt Lett, **27**(11), 903-905, 2002.

[66] Gander, M. J., MacPherson, W. N., Barton, J. S., Reuben, R. L., Jones, J. D. C., Stevens, R., Chana, K. S., Anderson, S. J. and Jones, T. V., *Embedded micromachined fiber-optic Fabry-Perot pressure sensors in aerodynamics applications*, Ieee Sens J, **3**(1), 102-107, 2003.

[67] Yu, B., Kim, D. W., Deng, J. D., Xiao, H. and Wang, A., *Fiber Fabry-Perot sensors for detection of partial discharges in power transformers*, Appl Optics, **42**(16), 3241-3250, 2003.

[68]   Lin, C. J. and Tseng, F. G., *A micro Fabry-Perot sensor for nano-lateral displacement sensing with enhanced sensitivity and pressure resistance*, Sensor Actuat a-Phys, **114**(2-3), 163-170, 2004.

[69]   Xiao, G. Z., Adnet, A., Zhang, Z. Y., Lu, Z. G. and Grover, C. P., *Fiber-optic Fabry-Perot interferometric gas-pressure sensors embedded in pressure fittings*, Microw Opt Techn Let, **42**(6), 486-489, 2004.

[70]   Zhang, G. J., Yu, Q. X. and Song, S. D., *An investigation of interference/intensity demodulated fiber-optic Fabry-Perot cavity sensor*, Sensor Actuat a-Phys, **116**(1), 33-38, 2004.

[71]   Shen, F., Peng, W., Cooper, K., Pickrell, G. and Wang, A. B., *UV-induced intrinsic Fabry-Perot interferometric fiber sensors*, Sensors for Harsh Environments, **5590**, 47-56, 2004.

[72]   Xiao, G. Z., Adnet, A., Zhang, Z. Y., Sun, F. G. and Grover, C. P., *Monitoring changes in the refractive index of gases by means of a fiber optic Fabry-Perot interferometer sensor*, Sensor Actuat a-Phys, **118**(2), 177-182, 2005.

[73]   Xu, J. C., Wang, X. W., Cooper, K. L. and Wang, A. B., *Miniature all-silica fiber optic pressure and acoustic sensors*, Opt Lett, **30**(24), 3269-3271, 2005.

[74]   Cibula, E. and Donlagic, D., *Miniature fiber-optic pressure sensor with a polymer diaphragm*, Appl Optics, **44**(14), 2736-2744, 2005.

[75]   Kim, D. W., Shen, F., Chen, X. P. and Wang, A. B., *Simultaneous measurement of refractive index and temperature based on a reflection-mode long-period grating and an intrinsic Fabry-Perot interferometer sensor*, Opt Lett, **30**(22), 3000-3002, 2005.

[76]   Zhu, Y. Z., Cooper, K. L., Pickrell, G. R. and Wang, A., *High-temperature fiber-tip pressure sensor*, J Lightwave Technol, **24**(2), 861-869, 2006.

[77]   Wang, X. W., Xu, J. C., Zhu, Y. Z., Cooper, K. L. and Wang, A. B., *All-fused-silica miniature optical fiber tip pressure sensor*, Opt Lett, **31**(7), 885-887, 2006.

[78]   Cranch, G. A., Flockhart, G. M. H., MacPherson, W. N., Barton, J. S. and Kirkendall, C. K., *Ultra-high-sensitivity two-dimensional bend sensor*, Electron Lett, **42**(9), 520-522, 2006.

[79]   Chen, X. P., Shen, F. B., Wang, Z. A., Huang, Z. Y. and Wang, A. B., *Micro-air-gap based intrinsic Fabry-Perot interferometric fiber-optic sensor*, Appl Optics, **45**(30), 7760-7766, 2006.

[80]   Tuck, C. J., Hague, R. and Doyle, C., *Low cost optical fibre based Fabry-Perot strain sensor production*, Meas Sci Technol, **17**(8), 2206-2212, 2006.

[81]   Machavaram, V. R., Badcock, R. A. and Fernando, G. F., *Fabrication of intrinsic fibre Fabry-Perot sensors in silica fibres using hydrofluoric acid etching*, Sensor Actuat a-Phys, **138**(1), 248-260, 2007.

[82]   Cibula, E. and Donlagic, D., *In-line short cavity Fabry-Perot strain sensor for quasi distributed measurement utilizing standard OTDR*, Opt Express, **15**(14), 8719-8730, 2007.

[83]   Zhang, Y., Chen, X. P., Wang, Y. X., Cooper, K. L. and Wang, A. B., *Microgap multicavity Fabry-Perot biosensor*, J Lightwave Technol, **25**(7), 1797-1804, 2007.

[84]   Ran, Z. L., Rao, Y. J., Deng, H. Y. and Liao, X., *Miniature in-line photonic crystal fiber etalon fabricated by 157 nm laser micromachining*, Opt Lett, **32**(21), 3071-3073, 2007.

[85]   Rao, Y. J., Zhu, T., Yang, X. C. and Duan, D. W., *In-line fiber-optic etalon formed by hollow-core photonic crystal fiber*, Opt Lett, **32**(18), 2662-2664, 2007.

[86]   Wang, Z., Shen, F. B., Song, L. J., Wang, X. W. and Wang, A. B., *Multiplexed fiber Fabry-Perot interferometer sensors based on ultrashort Bragg gratings*, Ieee Photonic Tech L, **19**(5-8), 622-624, 2007.

[87]   Ran, Z. L., Rao, Y. J., Liu, W. J., Liao, X. and Chiang, K. S., *Laser-micromachined Fabry-Perot optical fiber tip sensor for high-resolution temperature-independent measurement of refractive index*, Opt Express, **16**(3), 2252-2263, 2008.

[88]   Wei, T., Han, Y. K., Li, Y. J., Tsai, H. L. and Xiao, H., *Temperature-insensitive miniaturized fiber inline Fabry-Perot interferometer for highly sensitive refractive index measurement*, Opt Express, **16**(8), 5764-5769, 2008.

[89] Wei, T., Han, Y. K., Tsai, H. L. and Xiao, H., *Miniaturized fiber inline Fabry-Perot interferometer fabricated with a femtosecond laser*, Opt Lett, **33**(6), 536-538, 2008.

[90] Rao, Y. J., Deng, M., Duan, D. W. and Zhu, T., *In-line fiber Fabry-Perot refractive-index tip sensor based on endlessly photonic crystal fiber*, Sensor Actuat a-Phys, **148**(1), 33-38, 2008.

[91] Choi, H. Y., Park, K. S., Park, S. J., Paek, U. C., Lee, B. H. and Choi, E. S., *Miniature fiber-optic high temperature sensor based on a hybrid structured Fabry-Perot interferometer*, Opt Lett, **33**(21), 2455-2457, 2008.

[92] Shi, Q., Lv, F. Y., Wang, Z., Jin, L., Hu, J. J., Liu, Z. Y., Kai, G. Y. and Dong, X. Y., *Environmentally stable Fabry-Perot-type strain sensor based on hollow-core photonic bandgap fiber*, Ieee Photonic Tech L, **20**(1-4), 237-239, 2008.

[93] Corres, J. M., Matias, I. R., Hernaez, M., Bravo, J. and Arregui, F. J., *Optical fiber humidity sensors using nanostructured coatings of SiO2 nanoparticles*, Ieee Sens J, **8**(3-4), 281-285, 2008.

[94] Jiang, Y. and Tang, C. J., *High-finesse micro-lens fiber-optic extrinsic Fabry-Perot interferometric sensors*, Smart Mater Struct, **17**(5), 2008.

[95] Liu, J., Sun, Y. Z. and Fan, X. D., *Highly versatile fiber-based optical Fabry-Perot gas sensor*, Opt Express, **17**(4), 2731-2738, 2009.

[96] Cibula, E., Pevec, S., Lenardic, B., Pinet, E. and Donlagic, D., *Miniature all-glass robust pressure sensor*, Opt Express, **17**(7), 5098-5106, 2009.

[97] Morris, P., Hurrell, A., Shaw, A., Zhang, E. and Beard, P., *A Fabry-Perot fiber-optic ultrasonic hydrophone for the simultaneous measurement of temperature and acoustic pressure*, J Acoust Soc Am, **125**(6), 3611-3622, 2009.

[98] Ran, Z. L., Rao, Y. J., Zhang, J., Liu, Z. W. and Xu, B., *A miniature fiber-optic refractive-index sensor based on laser-machined Fabry-Perot interferometer tip*, J Lightwave Technol, **27**(23), 5426-5429, 2009.

[99] Frazao, O., Baptista, J. M., Santos, J. L., Kobelke, J. and Shuster, K., *Refractive index tip sensor based on Fabry-Perot cavities formed by a suspended core fibre*, J Eur Opt Soc-Rapid, **4**, 2009.

[100] Frazao, O., Aref, S. H., Baptista, J. M., Santos, J. L., Latifi, H., Farahi, F., Kobelke, J. and Schuster, K., *Fabry-Perot cavity based on a suspended-core fiber for strain and temperature measurement*, Ieee Photonic Tech L, **21**(17), 1229-1231, 2009.

[101] Villatoro, J., Finazzi, V., Coviello, G. and Pruneri, V., *Photonic-crystal-fiber-enabled micro-Fabry-Perot interferometer*, Opt Lett, **34**(16), 2441-2443, 2009.

[102] Gong, Y., Rao, Y. J., Guo, Y., Ran, Z. L. and Wu, Y., *Temperature-insensitive micro Fabry-Prot strain sensor fabricated by chemically etching Er-doped fiber*, Ieee Photonic Tech L, **21**(22), 1725-1727, 2009.

[103] Rao, Y. J., Deng, M., Zhu, T. and Li, H., *In-line Fabry-Perot etalons based on hollow-core photonic bandgap fibers for high-temperature applications*, J Lightwave Technol, **27**(19), 4360-4365, 2009.

[104] Choi, H. Y., Mudhana, G., Park, K. S., Paek, U. C. and Lee, B. H., *Cross-talk free and ultra-compact fiber optic sensor for simultaneous measurement of temperature and refractive index*, Opt Express, **18**(1), 141-149, 2010.

[105] Gong, Y. A., Guo, Y., Rao, Y. J., Zhao, T. A. and Wu, Y., *Fiber-Optic Fabry-Perot sensor based on periodic focusing effect of graded-index multimode fibers*, Ieee Photonic Tech L, **22**(23), 1708-1710, 2010.

[106] Gong, Y. A., Zhao, T. A., Rao, Y. J., Wu, Y. and Guo, Y., *A ray-transfer-matrix model for hybrid fiber Fabry-Perot sensor based on graded-index multimode fiber*, Opt Express, **18**(15), 15844-15852, 2010.

[107] Frazao, O., Silva, S. F., Viegas, J., Baptista, J. M., Santos, J. L. and Roy, P., *A hybrid Fabry-Perot/Michelson interferometer sensor using a dual asymmetric core microstructured fiber*, Meas Sci Technol, **21**(2), 2010.

[108] Kou, J. L., Feng, J., Wang, Q. J., Xu, F. and Lu, Y. Q., *Microfiber-probe-based ultrasmall interferometric sensor*, Opt Lett, **35**(13), 2308-2310, 2010.

[109] Deng, M., Tang, C. P., Zhu, T., Rao, Y. J., Xu, L. C. and Han, M., *Refractive index measurement using photonic crystal fiber-based Fabry-Perot interferometer*, Appl Optics, **49**(9), 1593-1598, 2010.

[110] Zhao, J. R., Huang, X. G., He, W. X. and Chen, J. H., *High-resolution and temperature-insensitive fiber optic refractive index sensor based on Fresnel reflection modulated by Fabry-Perot interference*, J Lightwave Technol, **28**(19), 2799-2803, 2010.

[111] Zhu, T., Ke, T., Rao, Y. J. and Chiang, K. S., *Fabry-Perot optical fiber tip sensor for high temperature measurement*, Opt Commun, **283**(19), 3683-3685, 2010.

[112] Pinto, A. M. R., Frazao, O., Santos, J. L., Lopez-Amo, M., Kobelke, J. and Schuster, K., *Interrogation of a suspended-core Fabry-Perot temperature sensor through a dual wavelength Raman fiber laser*, J Lightwave Technol, **28**(21), 3149-3155, 2010.

[113] Ke, T., Zhu, T., Rao, Y. J. and Deng, M., *Accelerometer based on all-fiber Fabry-Perot interferometer formed by hollow-core photonic crystal fiber*, Microw Opt Techn Let, **52**(11), 2531-2535, 2010.

[114] Wang, W. H., Wu, N., Tian, Y., Niezrecki, C. and Wang, X. W., *Miniature all-silica optical fiber pressure sensor with an ultrathin uniform diaphragm*, Opt Express, **18**(9), 9006-9014, 2010.

[115] Duan, D. W., Rao, Y. J., Wen, W. P., Yao, J., Wu, D., Xu, L. C. and Zhu, T., *In-line all-fibre Fabry-Perot interferometer high temperature sensor formed by large lateral offset splicing*, Electron Lett, **47**(6), 401-402, 2011.

[116] Nguyen, L. V., Vasiliev, M. and Alameh, K., *Three-wave fiber Fabry-Perot interferometer for simultaneous measurement of temperature and water salinity of seawater*, Ieee Photonic Tech L, **23**(7), 450-452, 2011.

[117] Pevec, S. and Donlagic, D., *All-fiber, long-active-length Fabry-Perot strain sensor*, Opt Express, **19**(16), 15641-15651, 2011.

[118] Cibula, E. and Donlagic, D., *In-line Fabry-Perot refractive index sensor*, Ieee Photonic Tech L, **23**(21), 1609-1611, 2011.

[119] Zhou, K. M., Yan, Z. J., Zhang, L. and Bennion, I., *Refractometer based on fiber Bragg grating Fabry-Perot cavity embedded with a narrow microchannel*, Opt Express, **19**(12), 11769-11779, 2011.

[120] Zhou, X. L. and Yu, Q. X., *Wide-range displacement sensor based on fiber-optic Fabry-Perot interferometer for subnanometer measurement*, Ieee Sens J, **11**(7), 1602-1606, 2011.

[121] Deng, M., Tang, C. P., Zhu, T. and Rao, Y. J., *PCF-based Fabry-Perot interferometric sensor for strain measurement at high temperatures*, Ieee Photonic Tech L, **23**(11), 700-702, 2011.

[122] Ferreira, M. S., Coelho, L., Schuster, K., Kobelke, J., Santos, J. L. and Frazao, O., *Fabry-Perot cavity based on a diaphragm-free hollow-core silica tube*, Opt Lett, **36**(20), 4029-4031, 2011.

[123] Gouveia, C., Jorge, P. A. S., Baptista, J. M. and Frazao, O., *Fabry-Perot cavity based on a high-birefringent fiber Bragg grating for refractive index and temperature measurement*, Ieee Sens J, **12**(1), 17-21, 2012.

[124] Wang, T. T. and Wang, M., *Fabry-Perot fiber sensor for simultaneous measurement of refractive index and temperature based on an in-fiber ellipsoidal cavity*, Ieee Photonic Tech L, **24**(19), 1733-1736, 2012.

[125] Silva, S., Coelho, L., Andre, R. M. and Frazao, O., *Gas refractometry based on an all-fiber spatial optical filter*, Opt Lett, **37**(16), 3450-3452, 2012.

[126] Liao, C. R., Hu, T. Y. and Wang, D. N., *Optical fiber Fabry-Perot interferometer cavity fabricated by femtosecond laser micromachining and fusion splicing for refractive index sensing*, Opt Express, **20**(20), 22813-22818, 2012.

[127] Duan, D. W., Rao, Y. J. and Zhu, T., *High sensitivity gas refractometer based on all-fiber open-cavity Fabry-Perot interferometer formed by large lateral offset splicing*, J Opt Soc Am B, **29**(5), 912-915, 2012.

[128] Liu, L., Gong, Y., Wu, Y., Zhao, T., Wu, H. J. and Rao, Y. J., *Spatial frequency multiplexing of fiber-optic interferometric refractive index sensors based on graded-index multimode fibers*, Sensors-Basel, **12**(9), 12377-12385, 2012.

[129] Hu, D. J. J., Wang, Y. X., Lim, J. L., Zhang, T. S., Milenko, K. B., Chen, Z. H., Jiang, M., Wang, G. H., Luan, F., Shum, P. P., Sun, Q. Z., Wei, H. F., Tong, W. J. and Wolinski, T. R., *Novel miniaturized Fabry-Perot refractometer based on a simplified hollow-core fiber with a hollow silica sphere tip*, Ieee Sens J, **12**(5), 1239-1245, 2012.

[130] Favero, F. C., Araujo, L., Bouwmans, G., Finazzi, V., Villatoro, J. and Pruneri, V., *Spheroidal Fabry-Perot microcavities in optical fibers for high-sensitivity sensing*, Opt Express, **20**(7), 7112-7118, 2012.

[131] Wang, T. T., Wang, M. and Ni, H. B., *Micro-Fabry-Perot interferometer with high contrast based on an in-fiber ellipsoidal cavity*, Ieee Photonic Tech L, **24**(11), 948-950, 2012.

[132] Duan, D. W., Rao, Y. J., Hou, Y. S. and Zhu, T., *Microbubble based fiber-optic Fabry-Perot interferometer formed by fusion splicing single-mode fibers for strain measurement*, Appl Optics, **51**(8), 1033-1036, 2012.

[133] Ferreira, M. S., Bierlich, J., Kobelke, J., Schuster, K., Santos, J. L. and Frazao, O., *Towards the control of highly sensitive Fabry-Perot strain sensor based on hollow-core ring photonic crystal fiber*, Opt Express, **20**(20), 21946-21952, 2012.

[134] Tafulo, P. A. R., Jorge, P. A. S., Santos, J. L., Araujo, F. M. and Frazao, O., *Intrinsic Fabry-Perot cavity sensor based on etched multimode graded index fiber for strain and temperature measurement*, Ieee Sens J, **12**(1), 8-12, 2012.

[135] Tafulo, P. A. R., Jorge, P. A. S., Santos, J. L. and Frazao, O., *Fabry-Perot cavities based on chemical etching for high temperature and strain measurement*, Opt Commun, **285**(6), 1159-1162, 2012.

[136] Zhang, J., Sun, H., Rong, Q. Z., Ma, Y., Liang, L., Xu, Q. F., Zhao, P., Feng, Z. Y., Hu, M. L. and Qiao, X. G., *High-temperature sensor using a Fabry-Perot interferometer based on solid-core photonic crystal fiber*, Chin Opt Lett, **10**(7), 2012.

[137] Xu, L. C., Deng, M., Duan, D. W., Wen, W. P. and Han, M., *High-temperature measurement by using a PCF-based Fabry-Perot interferometer*, Opt Laser Eng, **50**(10), 1391-1396, 2012.

[138] Pevec, S. and Donlagic, D., *Miniature all-fiber Fabry-Perot sensor for simultaneous measurement of pressure and temperature*, Appl Optics, **51**(19), 4536-4541, 2012.

[139] Lai, C. W., Lo, Y. L., Yur, J. P., Liu, W. F. and Chuang, C. H., *Application of Fabry-Perot and fiber Bragg grating pressure sensors to simultaneous measurement of liquid level and specific gravity*, Measurement, **45**(3), 469-473, 2012.

[140] Wang, D. H., Wang, S. J. and Jia, P. G., *In-line silica capillary tube all-silica fiber-optic Fabry-Perot interferometric sensor for detecting high intensity focused ultrasound fields*, Opt Lett, **37**(11), 2046-2048, 2012.

[141] Wang, Y., Wang, D. N., Liao, C. R., Hu, T. Y., Guo, J. T. and Wei, H. F., *Temperature-insensitive refractive index sensing by use of micro Fabry-Perot cavity based on simplified hollow-core photonic crystal fiber*, Opt Lett, **38**(3), 269-271, 2013.

[142] Sun, H., Zhang, J., Rong, Q., Feng, D., Du, Y., Zhang, X., Su, D., Zhou, L., Feng, Z., Qiao, X. and Hu, M., *A hybrid fiber interferometer for simultaneous refractive index and temperature measurements based on Fabry–Perot/Michelson interference*, Ieee Sens J, **13**(5), 2039-2044, 2013.

[143] Zhang, J. J., Sun, Q. Z., Liang, R. B., Jia, W. H., Li, X. L., Wo, J. H., Liu, D. M. and Shum, P. P., *Microfiber Fabry-Perot interferometer for dual-parameter sensing*, J Lightwave Technol, **31**(10), 1608-1615, 2013.

[144] Lee, C. L., Hsu, J. M., Horng, J. S., Sung, W. Y. and Li, C. M., *Microcavity fiber Fabry-Perot interferometer with an embedded golden thin film*, Ieee Photonic Tech L, **25**(9), 833-836, 2013.

[145] Ferreira, M. S., Bierlich, J., Unger, S., Schuster, K., Santos, J. L. and Frazao, O., *Post-processing of Fabry-Perot microcavity tip sensor*, Ieee Photonic Tech L, **25**(16), 1593-1596, 2013.

[146] Zhao, Y., Wang, D. and Lv, R. Q., *A novel optical fiber temperature sensor based on Fabry-Perot cavity*, Microw Opt Techn Let, **55**(10), 2487-2490, 2013.

[147] Jin, L., Guan, B. O. and Wei, H. F., *Sensitivity characteristics of Fabry-Perot pressure sensors based on hollow-core microstructured fibers*, J Lightwave Technol, **31**(15), 2526-2532, 2013.

[148] Zou, X. T., Wu, N., Tian, Y., Zhang, Y., Fitek, J., Maffeo, M., Niezrecki, C., Chen, J. and Wang, X. W., *Ultrafast Fabry-Perot fiber-optic pressure sensors for multimedia blast event measurements*, Appl Optics, **52**(6), 1248-1254, 2013.

[149] Lee, C. L., Chang, H. J., You, Y. W., Chen, G. H., Hsu, J. M. and Horng, J. S., *Fiber Fabry-Perot interferometers based on air-bubbles/liquid in hollow core fibers*, Ieee Photonic Tech L, **26**(8), 749-752, 2014.

[150] Liu, S., Wang, Y. P., Liao, C. R., Wang, G. J., Li, Z. Y., Wang, Q., Zhou, J. T., Yang, K. M., Zhong, X. Y., Zhao, J. and Tang, J., *High-sensitivity strain sensor based on in-fiber improved Fabry-Perot interferometer*, Opt Lett, **39**(7), 2121-2124, 2014.

[151] Zhou, A., Qin, B. Y., Zhu, Z., Zhang, Y. X., Liu, Z. H., Yang, J. and Yuan, L. B., *Hybrid structured fiber-optic Fabry-Perot interferometer for simultaneous measurement of strain and temperature*, Opt Lett, **39**(18), 5267-5270, 2014.

[152] Ferreira, M. S., Bierlich, J., Unger, S., Schuster, K., Santos, J. L. and Frazao, O., *Optical phase refractometer based on post-processed interferometric tip sensors*, J Lightwave Technol, **32**(17), 3002-3007, 2014.

[153] Pevec, S. and Donlagic, D., *Miniature fiber-optic sensor for simultaneous measurement of pressure and refractive index*, Opt Lett, **39**(21), 6221-6224, 2014.

[154] Andre, R. M., Pevec, S., Becker, M., Dellith, J., Rothhardt, M., Marques, M. B., Donlagic, D., Bartelt, H. and Frazao, O., *Focused ion beam post-processing of optical fiber Fabry-Perot cavities for sensing applications*, Opt Express, **22**(11), 13102-13108, 2014.

[155] Gao, S. C., Zhang, W. G., Bai, Z. Y., Zhang, H., Lin, W., Wang, L. and Li, J. L., *Microfiber-enabled in-line Fabry-Perot interferometer for high-sensitive force and refractive index sensing*, J Lightwave Technol, **32**(9), 1682-1688, 2014.

[156] Ding, W. H. and Jiang, Y., *Miniature photonic crystal fiber sensor for high-temperature measurement*, Ieee Sens J, **14**(3), 786-789, 2014.

[157] Du, Y. Y., Qiao, X. G., Rong, Q. Z., Yang, H. Z., Feng, D. Y., Wang, R. H., Hu, M. L. and Feng, Z. Y., *A miniature Fabry-Perot interferometer for high temperature measurement using a double-core photonic crystal fiber*, Ieee Sens J, **14**(4), 1069-1073, 2014.

[158] Liao, C. R., Liu, S., Xu, L., Wang, C., Wang, Y. P., Li, Z. Y., Wang, Q. and Wang, D. N., *Sub-micron silica diaphragm-based fiber-tip Fabry-Perot interferometer for pressure measurement*, Opt Lett, **39**(10), 2827-2830, 2014.

[159] Eom, J., Park, C.-J., Lee, B. H., Lee, J.-H., Kwon, I.-B. and Chung, E., *Fiber optic Fabry–Perot pressure sensor based on lensed fiber and polymeric diaphragm*, Sensors and Actuators A **225**, 25–32, 2015.

[160] Lee, C.-L., Ho, H.-Y., Gu, J.-H., Yeh, T.-Y. and Tseng, C.-H., *Dual hollow core fiber-based Fabry–Perot interferometer for measuring the thermo-optic coefficients of liquids*, Opt Lett, **40**(4), 459-462, 2015.

[161] Sun, B., Wang, Y., Qu, J., Liao, C., Yin, G., He, J., Zhou, J., Tang, J., Liu, S., Li, Z. and Liu, Y., *Simultaneous measurement of pressure and temperature by employing Fabry-Perot interferometer based on pendant polymer droplet* Opt Express, **23**(3), 1906-1911, 2015.

[162] Wu, D., Huang, Y., Fu, J.-Y. and Wang, G.-Y., *Fiber Fabry–Perot tip sensor based on multimode photonic crystal fiber*, Opt Commun, **338**, 288–291, 2015.

[163] Li, Q. and Chen, H., *Design of fiber magnetic field sensor based on fiber Bragg grating Fabry-Perot cavity ring-down spectroscopy*, Photonic Sensors, 2015.

[164] Pullteap, S. and Seat, H. C., *An extrinsic fiber Fabry-Perot interferometer for dynamic displacement measurement*, Photonic Sensors, **5**(1), 50-59, 2015.

[165] Liu, S., Yang, K. M., Wang, Y. P., Qu, J. L., Liao, C. R., He, J., Li, Z. Y., Yin, G. L., Sun, B., Zhou, J. T., Wang, G. J., Tang, J. and Zhao, J., *High-sensitivity strain sensor based on in-fiber rectangular air bubble*, Sci Rep-Uk, **5**, 2015.

[166] Chen, Z., Yuan, L., Hefferman, G. and Wei, T., *Ultraweak intrinsic Fabry-Perot cavity array for distributed sensing*, Opt Lett, **40**(3), 320-323, 2015.

[167] Liu, G. G., Han, M. and Hou, W. L., *High-resolution and fast-response fiber-optic temperature sensor using silicon Fabry-Perot cavity*, Opt Express, **23**(6), 7237-7247, 2015.

[168] Liu, T. G., Yin, J. D., Jiang, J. F., Liu, K., Wang, S. and Zou, S. L., *Differential-pressure-based fiber-optic temperature sensor using Fabry-Perot interferometry*, Opt Lett, **40**(6), 1049-1052, 2015.

[169] Zhang, X. P. and Peng, W., *Temperature-independent fiber salinity sensor based on Fabry-Perot interference*, Opt Express, **23**(8), 10353-10358, 2015.

[170] Ferreira, M. S., Bierlich, J., Lehmann, H., Schuster, K., Kobelke, J., Santos, J. L. and Frazao, O., *Fabry-Perot cavity based on hollow-core ring photonic crystal fiber for pressure sensing*, Ieee Photonic Tech L, **24**(23), 2122-2124, 2012.

[171] Bravo, J., Matias, I. R., Del Villar, I., Corres, J. M. and Arregui, F. J., *Nanofilms on hollow core fiber-based structures: An optical study*, J Lightwave Technol, **24**(5), 2100-2107, 2006.

[172] Tian, J. J., Lu, Y. J., Zhang, Q. and Han, M., *Microfluidic refractive index sensor based on an all-silica in-line Fabry-Perot interferometer fabricated with microstructured fibers*, Opt Express, **21**(5), 6633-6639, 2013.

[173] Duan, D. W., Rao, Y. J., Xu, L. C., Zhu, T., Deng, M., Wu, D. and Yao, J., *In-fiber Fabry-Perot and Mach-Zehnder interferometers based on hollow optical fiber fabricated by arc fusion splicing with small lateral offsets*, Opt Commun, **284**(22), 5311-5314, 2011.

[174] Ferreira, M. S., Schuster, K., Kobelke, J., Santos, J. L. and Frazao, O., *Spatial optical filter sensor based on hollow-core silica tube*, Opt Lett, **37**(5), 890-892, 2012.

[175] Passaro, D., Foroni, M., Poli, F., Cucinotta, A., Selleri, S., Laegsgaard, J. and Bjarklev, A. O., *All-silica hollow-core micro structured Bragg fibers for biosensor application*, Ieee Sens J, **8**(7-8), 1280-1286, 2008.

[176] Cox, F. M., Argyros, A. and Large, M. C. J., *Liquid-filled hollow core microstructured polymer optical fiber*, Opt Express, **14**(9), 4135-4140, 2006.

[177] Yan, H., Gua, C., Yang, C. X., Liu, J., Jin, G. F., Zhang, J. T., Hou, L. T. and Yao, Y., *Hollow core photonic crystal fiber surface-enhanced Raman probe*, Appl Phys Lett, **89**(20), 2006.

[178] Smolka, S., Barth, M. and Benson, O., *Highly efficient fluorescence sensing with hollow core photonic crystal fibers*, Opt Express, **15**(20), 12783-12791, 2007.

[179] Zhang, Y., Shi, C., Gu, C., Seballos, L. and Zhang, J. Z., *Liquid core photonic crystal fiber sensor based on surface enhanced Raman scattering*, Appl Phys Lett, **90**(19), 2007.

[180] Shi, C., Lu, C., Gu, C., Tian, L., Newhouse, R., Chen, S. W. and Zhang, J. Z., *Inner wall coated hollow core waveguide sensor based on double substrate surface enhanced Raman scattering*, Appl Phys Lett, **93**(15), 2008.

[181] Ritari, T., Tuominen, J., Ludvigsen, H., Petersen, J. C., Sorensen, T., Hansen, T. P. and Simonsen, H. R., *Gas sensing using air-guiding photonic bandgap fibers*, Opt Express, **12**(17), 4080-4087, 2004.

[182] Hoo, Y. L., Jin, W., Ho, H. L., Ju, J. and Wang, D. N., *Gas diffusion measurement using hollow-core photonic bandgap fiber*, Sensor Actuat B-Chem, **105**(2), 183-186, 2005.

[183] Shavrin, I., Novotny, S., Shevchenko, A. and Ludvigsen, H., *Gas refractometry using a hollow-core photonic bandgap fiber in a Mach-Zehnder-type interferometer*, Appl Phys Lett, **100**(5), 2012.

[184] Zhao, Y., Lv, R. Q., Ying, Y. and Wang, Q., *Hollow-core photonic crystal fiber Fabry-Perot sensor for magnetic field measurement based on magnetic fluid*, Opt Laser Technol, **44**(4), 899-902, 2012.

[185] Aref, S. H., Amezcua-Correa, R., Carvalho, J. P., Frazao, O., Caldas, P., Santos, J. L., Araujo, F. M., Latifi, H., Farahi, F., Ferreira, L. A. and Knight, J. C., *Modal interferometer based on*

hollow-core photonic crystal fiber for strain and temperature measurement, Opt Express, **17**(21), 18669-18675, 2009.

[186] Kim, G., Cho, T. Y., Hwang, K., Lee, K., Lee, K. S., Han, Y. G. and Lee, S. B., *Strain and temperature sensitivities of an elliptical hollow-core photonic bandgap fiber based on Sagnac interferometer*, Opt Express, **17**(4), 2481-2486, 2009.

[187] Lu, Y. J., Han, M. and Tian, J. J., *Fiber-optic temperature sensor using a Fabry-Perot cavity filled with gas of variable pressure*, Ieee Photonic Tech L, **26**(8), 757-760, 2014.

[188] Zhu, Y. Z. and Wang, A. B., *Miniature fiber-optic pressure sensor*, Ieee Photonic Tech L, **17**(2), 447-449, 2005.

[189] Coelho, L., Tafulo, P. A. R., Jorge, P. A. S., Santos, J. L., Viegas, D., Schuster, K., Kobelke, J. and Frazao, O., *Simultaneous measurement of partial pressure of O_2 and CO_2 with a hybrid interferometer*, Opt Lett, **37**(15), 3063-3065, 2012.

[190] Bae, H. and Yu, M., *Miniature Fabry-Perot pressure sensor created by using UV-molding process with an optical fiber based mold*, Opt Express, **20**(13), 14573-14583, 2012.

[191] Bae, H. D., Yun, D., Liu, H. J., Olson, D. A. and Yu, M., *Hybrid miniature Fabry-Perot sensor with dual optical cavities for simultaneous pressure and temperature measurements*, J Lightwave Technol, **32**(8), 1585-1593, 2014.

[192] Tian, F., He, Z. H. and Du, H., *Numerical and experimental investigation of long-period gratings in photonic crystal fiber for refractive index sensing of gas media*, Opt Lett, **37**(3), 380-382, 2012.

[193] Fliessbach, T., Curso de física estatística, 3rd ed., Fundação Calouste Gulbenkian, 2000.

[194] Edlén, B., *The refractive index of air*, Metrologia, **2**(2), 71-80, 1966.

[195] Bradley, C. C. and Gebbie, H. A., *Refractive index of nitrogen, water vapor, and their mixtures at submillimeter wavelengths*, Appl Optics, **10**(4), 755-&, 1971.

[196] Simmons, A. C., *Refractive-index and Lorentz-Lorenz functions of propane, nitrogen and carbon-dioxide in spectral range 15803-22002 cm^{-1} and at 944 cm^{-1}*, Opt Commun, **25**(2), 211-214, 1978.

[197] Achtermann, H. J., Hong, J. G., Wagner, W. and Pruss, A., *Refractive-index and density isotherms for methane from 273 K to 373 K and at pressures up to 34 Mpa*, J Chem Eng Data, **37**(4), 414-418, 1992.

[198] Ciddor, P. E., *Refractive index of air: New equations for the visible and near infrared*, Appl Optics, **35**(9), 1566-1573, 1996.

[199] Birch, K. P. and Downs, M. J., *An updated Edlen equation for the refractive-index of air*, Metrologia, **30**(3), 155-162, 1993.

[200] Zhang, J., Lu, Z. H. and Wang, L. J., *Precision refractive index measurements of air, N_2, O_2, Ar, and CO_2 with a frequency comb*, Appl Optics, **47**(17), 3143-3151, 2008.

[201] Birch, K. P. and Downs, M. J., *Correction to the updated Edlen equation for the refractive-index of air*, Metrologia, **31**(4), 315-316, 1994.

[202] Bonsch, G. and Potulski, E., *Measurement of the refractive index of air and comparison with modified Edlen's formulae*, Metrologia, **35**(2), 133-139, 1998.

[203] Peck, E. R. and Khanna, B. N., *Dispersion of nitrogen*, J Opt Soc Am, **56**(8), 1059-&, 1966.

[204] Wright, J. D., Gas property equations for NIST fluid flow goup gas flow measurement calibration services, in, National Institute of Standards and Technology (NIST), 2004.

[205] Hilsenrath, J., Beckett, C. W., Benedict, W. S., Fano, L., Hoge, H. J., Masi, J. F., Nuttal, R. L., Touloukian, Y. S. and Woolley, H. W., Tables of thermal properties of gases, U.S. Government Printing Office, 1955.

[206] Frazao, O., Carvalho, J. P. and Salgado, H. M., *Low-loss splice in a microstructured fibre using a conventional fusion splicer*, Microw Opt Techn Let, **46**(2), 172-174, 2005.

[207] Pal, B. P., Optical waveguide sensors, in: Handbook of optical sensors, CRC Press, Taylor & Francis Group, 2015.

[208] Roriz, P., Ferreira, M. S., Schuster, K., Kobelke, J. and Frazao, O., *A Fabry-Perot sensor prototype for low-pressure measurements*, Microw Opt Techn Let, **56**(12), 2981-2984, 2014.

[209] Hecht, E., *Óptica*, 3rd ed., Fundação Calouste Gulbenkian, 2002.

[210] Kawakami, S. and Nishida, S., *Anomalous dispersion of new doubly clad optical fiber*, Electron Lett, **10**(4), 38-40, 1974.

[211] Kawakami, S. and Nishida, S., *Characteristics of a doubly clad optical fiber with a low-index inner cladding*, Ieee J Quantum Elect, **Qe10**(12), 879-887, 1974.

[212] Stolen, R. H., Ramaswamy, V., Kaiser, P. and Pleibel, W., *Linear polarization in birefringent single-mode fibers*, Appl Phys Lett, **33**(8), 699-701, 1978.

[213] Snitzer, E., Po, H., Hakimi, F., Tumminelli, R. and McCollum, B. C., Double-clad, offset-core Nd fiber laser, in: Optical Fiber Sensors, New Orleans, Louisiana United States, 1988, PD5.

[214] Jeong, Y., Sahu, J. K., Payne, D. N. and Nilsson, J., *Ytterbium-doped large-core fiber laser with 1.36 kW continuous-wave output power*, Opt Express, **12**(25), 6088-6092, 2004.

[215] Marhic, M. E., Amplification and lasing in optical fibers, in: L. Thévenaz (Ed.) Advanced fiber optics, EPFL Press, 2011, 171-194.

[216] Salhi, M., Leblond, H. and Sanchez, F., *High power tunable all fiber double-clad Er : Yb : silicate fiber laser*, Opt Commun, **247**(1-3), 181-185, 2005.

[217] Hirano, Y., Shoji, Y., Kasahara, K., Yoshida, M. and Hisada, Y., Multiwatt operation of square-shaped double-clad Nd-doped fiber amplifier, in: CLEO, 1998, CTh058.

[218] Po, H., Cao, J. D., Laliberte, B. M., Minns, R. A., Robinson, R. F., Rockney, B. H., Tricca, R. R. and Zhang, Y. H., *High-power neodymium-doped single transverse-mode fiber laser*, Electron Lett, **29**(17), 1500-1501, 1993.

[219] Li, Y. H., Jackson, S. D. and Fleming, S., *High absorption and low splice loss properties of hexagonal double-clad fiber*, Ieee Photonic Tech L, **16**(11), 2502-2504, 2004.

[220] Fu, L., Jain, A., Xie, H. K., Cranfield, C. and Gu, M., *Nonlinear optical endoscopy based on a double-clad photonic crystal fiber and a MEMS mirror*, Opt Express, **14**(3), 1027-1032, 2006.

[221] Han, Q., Lan, X. W., Huang, J., Kaur, A., Wei, T., Gao, Z. and Xiao, H., *Long-period grating inscribed on concatenated double-clad and single-clad fiber for simultaneous measurement of temperature and refractive index*, Ieee Photonic Tech L, **24**(13), 1130-1132, 2012.

[222] Pang, F. F., Liu, H. H., Chen, N., Liu, Y. Q., Zeng, X. L., Chen, Z. Y. and Wang, T. Y., *Cladding-mode resonance of a double-cladding fiber at a near modal cut-off wavelength for RI sensing*, Meas Sci Technol, **21**(9), 2010.

[223] Liu, H. H., Pang, F. F., Guo, H. R., Cao, W. X., Liu, Y. Q., Chen, N., Chen, Z. Y. and Wang, T. Y., *In-series double cladding fibers for simultaneous refractive index and temperature measurement*, Opt Express, **18**(12), 13072-13082, 2010.

[224] Baiad, M. D., Gagne, M., Madore, W. J., De Montigny, E., Godbout, N., Boudoux, C. and Kashyap, R., *Surface plasmon resonance sensor interrogation with a double-clad fiber coupler and cladding modes excited by a tilted fiber Bragg grating*, Opt Lett, **38**(22), 4911-4914, 2013.

[225] Baiad, M. D., Gagne, M., Lemire-Renaud, S., De Montigny, E., Madore, W. J., Godbout, N., Boudoux, C. and Kashyap, R., *Capturing reflected cladding modes from a fiber Bragg grating with a double-clad fiber coupler*, Opt Express, **21**(6), 6873-6879, 2013.

[226] Bierlich, J., Kobelke, J., Brand, D., Kirsch, K., Dellith, J. and Bartelt, H., *Nanoscopic tip sensors fabricated by gas phase etching of optical glass fibers*, Photonic Sensors, **2**, 331-339, 2012.

[227] Kell, G. S., *Precise representation of volume properties of water at 1 atmosphere*, J Chem Eng Data, **12**(1), 66-&, 1967.

[228] Olson, J. D. and Horne, F. H., *Direct determination of temperature-dependence of refractive-index of liquids*, B Am Phys Soc, **18**(3), 406-406, 1973.

[229] Abbate, G., Bernini, U., Ragozzino, E. and Somma, F., *Temperature-dependence of refractive-index of water*, J Phys D Appl Phys, **11**(8), 1167-1172, 1978.

[230] Thormahlen, I., Straub, J. and Grigull, U., *Refractive-index of water and its dependence on wavelength, temperature, and density*, J Phys Chem Ref Data, **14**(4), 933-946, 1985.

[231] Rao, Y. J., *In-fibre Bragg grating sensors*, Meas Sci Technol, **8**(4), 355-375, 1997.

[232] Rao, Y. J., Duan, D. W., Fan, Y. E., Ke, T. and Xu, M., *High-temperature annealing behaviors of CO_2 laser pulse-induced long-period fiber grating in a photonic crystal fiber*, J Lightwave Technol, **28**(10), 1530-1535, 2010.

[233] Mihailov, S. J., *Fiber Bragg grating sensors for harsh environments*, Sensors-Basel, **12**(2), 1898-1918, 2012.

[234] Martinez, A., Khrushchev, I. Y. and Bennion, I., *Thermal properties of fibre Bragg gratings inscribed point-by-point by infrared femtosecond laser*, Electron Lett, **41**(4), 176-178, 2005.

[235] Martinez, A., Dubov, M., Khrushchev, I. and Bennion, I., *Direct writing of fibre Bragg gratings by femtosecond laser*, Electron Lett, **40**(19), 1170-1172, 2004.

[236] Wang, Y. P., Qiao, X. G., Yang, H. Z., Su, D., Li, L. and Guo, T., *Sensitivity-improved strain sensor over a large range of temperatures ysing an etched and regenerated fiber Bragg grating*, Sensors-Basel, **14**(10), 18575-18582, 2014.

[237] Frazao, O., Silva, S. F. O., Guerreiro, A., Santos, J. L., Ferreira, L. A. and Araujo, F. M., *Strain sensitivity control of fiber Bragg grating structures with fused tapers*, Appl Optics, **46**(36), 8578-8582, 2007.

[238] Mazurin, O., Streltsina, M. and Shvaiko-Shvaikovskaia, T., Handbook of glass data. Part A: silica glass and binary silicate glasses, 1983.

[239] Bucaro, J. A. and Dardy, H. D., *High-temperature Brillouin-scattering in fused quartz*, J Appl Phys, **45**(12), 5324-5329, 1974.

[240] Mihailov, S. J., Grobnic, D., Smelser, C. W., Lu, P., Walker, R. B. and Ding, H. M., *Bragg grating inscription in various optical fibers with femtosecond infrared lasers and a phase mask*, Opt Mater Express, **1**(4), 754-765, 2011.

[241] Grobnic, D., Smelser, C. W., Mihailov, S. J. and Walker, R. B., *Long-term thermal stability tests at 1000 degrees C of silica fibre Bragg gratings made with ultrafast laser radiation*, Meas Sci Technol, **17**(5), 1009-1013, 2006.

[242] Snitzer, E., *Proposed fiber cavities for optical masers*, J Appl Phys, **32**(1), 36-&, 1961.

[243] Kim, H. K., Kim, S. K., Park, H. G. and Kim, B. Y., *Polarimetric fiber laser sensors*, Opt Lett, **18**(4), 317-319, 1993.

[244] Park, J. S., Yun, S. H., Ahn, S. J. and Kim, B. Y., *Polarization- and frequency-stable fiber laser for magnetic-field sensing*, Opt Lett, **21**(14), 1029-1031, 1996.

[245] Melle, S. M., Alavie, A. T., Karr, S., Coroy, T., Liu, K. X. and Measures, R. M., *A Bragg grating-tuned fiber laser strain sensor system*, Ieee Photonic Tech L, **5**(2), 263-266, 1993.

[246] Koo, K. P. and Kersey, A. D., *Bragg grating-based laser sensors systems with interferometric interrogation and wavelength-division multiplexing*, J Lightwave Technol, **13**(7), 1243-1249, 1995.

[247] Mandal, J., Pal, S., Sun, T., Grattan, K. T. V., Augousti, A. T. and Wade, S. A., *Bragg grating-based fiber-optic laser probe for temperature sensing*, Ieee Photonic Tech L, **16**(1), 218-220, 2004.

[248] Guan, B. O., Tam, H. Y., Lau, S. T. and Chan, H. L. W., *Ultrasonic hydrophone based on distributed Bragg reflector fiber laser*, Ieee Photonic Tech L, **17**(1), 169-171, 2005.

[249] Arellano-Sotelo, H., Barmenkov, Y. O. and Kir'yanov, A. V., *The use of erbium fiber laser relaxation frequency for sensing refractive index and solute concentration of aqueous solutions*, Laser Phys Lett, **5**(11), 825-829, 2008.

[250] Idris, S. M., Abdullah, F., Al-Mansoori, M. H., Jamaludin, M. Z. and Din, N. M., *Pressure sensing utilizing linear cavity erbium-doped fiber laser*, Laser Phys, **20**(4), 855-858, 2010.

[251] Wo, J. H., Jiang, M., Malnou, M., Sun, Q. Z., Zhang, J. J., Shum, P. P. and Liu, D. M., *Twist sensor based on axial strain insensitive distributed Bragg reflector fiber laser*, Opt Express, **20**(3), 2844-2850, 2012.

[252] Kringlebotn, J. T., Loh, W. H. and Laming, R. I., *Polarimetric Er^{3+}-doped fiber distributed-feedback laser sensor for differential pressure and force measurements*, Opt Lett, **21**(22), 1869-1871, 1996.

[253] Hadeler, O., Ronnekleiv, E., Ibsen, M. and Laming, R. I., *Polarimetric distributed feedback fiber laser sensor for simultaneous strain and temperature measurements*, Appl Optics, **38**(10), 1953-1958, 1999.

[254] Lovseth, S. W., Kringlebotn, J. T., Ronnekleiv, E. and Blotekjaer, K., *Fiber distributed-feedback lasers used as acoustic sensors in air*, Appl Optics, **38**(22), 4821-4830, 1999.

[255] Tanaka, S., Ogawa, T., Thongnum, W., Takahashi, N. and Takahashi, S., *Thermally stabilized fiber-Bragg-grating vibration sensor using erbium-doped fiber laser*, Jpn J Appl Phys 1, **42**(5b), 3060-3062, 2003.

[256] Frazao, O., Correia, C., Baptista, J. M., Marques, M. B. and Santos, J. L., *Ring fibre laser with interferometer based in long period grating for sensing applications*, Opt Commun, **281**(22), 5601-5604, 2008.

[257] Shi, L. L., Zhu, T., Fan, Y. E., Chiang, K. S. and Rao, Y. J., *Torsion sensing with a fiber ring laser incorporating a pair of rotary long-period fiber gratings*, Opt Commun, **284**(22), 5299-5302, 2011.

[258] Wei, S., Zhang, W., Shang, J. and Yin, L., *Torsion sensing characteristics of fibre ring laser based on nonlinear polarisation rotation*, Electron Lett, **48**(2), 116-U1227, 2012.

[259] Lima, S. E. U., Farias, R. G., Araujo, F. M., Ferreira, L. A., Santos, J. L., Miranda, V. and Frazao, O., *Fiber laser sensor based on a phase-shifted chirped grating for acoustic sensing of partial discharges*, Photonic Sensors, **3**(1), 44-51, 2013.

[260] Abdullah, F., Idris, S. M., Jamaludin, M. Z. and Al-Mansoori, M. H., *Hybrid erbium-doped fiber laser-pressure sensor utilizing ring cavity*, Laser Phys, **21**(6), 1099-1102, 2011.

[261] Zhou, K. J. and Ruan, Y. F., *Fiber ring laser employing an all-polarization-maintaining loop periodic filter*, Laser Phys, **20**(6), 1449-1452, 2010.

[262] Sun, G., Chung, Y. and Moon, D. S., *L-band tunable multiwavelength fiber laser using an unpumped polarization maintaining an erbium-ytterbium double-clad fiber-loop mirror*, Laser Phys, **18**(10), 1196-1199, 2008.

[263] Liang, P. S., Zhang, Z. X., Kuang, Q. Q. and Sang, M. H., *All-fiber birefringent filter with fine tunability and changeable spacing*, Laser Phys, **19**(11), 2124-2128, 2009.

[264] Kim, B. K. and Chung, Y., *Tunable and switchable SOA-based multi-wavelength fiber laser using twin-core photonic crystal fiber*, Laser Phys Lett, **9**(10), 734-738, 2012.

[265] Tan, S. J., Harun, S. W., Shahabuddin, N. S., Arof, H. and Ahmad, H., *Dual-cavity dual-output multi-wavelength fiber laser based on nonlinear polarization rotation effect*, Laser Phys, **22**(10), 1601-1605, 2012.

[266] Erdogan, T., *Fiber grating spectra*, J Lightwave Technol, **15**(8), 1277-1294, 1997.

[267] Kersey, A. D., Davis, M. A., Patrick, H. J., LeBlanc, M., Koo, K. P., Askins, C. G., Putnam, M. A. and Friebele, E. J., *Fiber grating sensors*, J Lightwave Technol, **15**(8), 1442-1463, 1997.

[268] Zhang, J., Shum, P., Cheng, X. P., Ngo, N. Q. and Li, S. Y., *Analysis of linearly tapered fiber Bragg grating for dispersion slope compensation*, Ieee Photonic Tech L, **15**(10), 1389-1391, 2003.

[269] Zhang, Q., Ianno, N. J. and Han, M., *Fiber-optic refractometer based on an etched high-Q π-phase-shifted fiber Bragg grating*, Sensors-Basel, **13**(7), 8827-8834, 2013.

[270] Romero, R., Frazao, O., Pereira, D. A., Salgado, H. M., Araujo, F. M. and Ferreira, L. A., *Intensity-referenced and temperature-independent curvature-sensing concept based on chirped fiber Bragg gratings*, Appl Optics, **44**(18), 3821-3826, 2005.

[271] Cranch, G. A., Fiber-optic sensor multiplexing principles in: J.L. Santos, F. Farahi (Eds.) Handbook of optical sensors, CRC Press, Taylor & Francis Group, 2015.

[272] Frazao, O., Baptista, J. M. and Santos, J. L., *Temperature-independent strain sensor based on a Hi-Bi photonic crystal fiber loop mirror*, Ieee Sens J, **7**(9-10), 1453-1455, 2007.

[273] Righini, G. C., Dumeige, Y., Feron, P., Ferrari, M., Conti, G. N., Ristic, D. and Soria, S., *Whispering gallery mode microresonators: Fundamentals and applications*, Riv Nuovo Cimento, **34**(7), 435-488, 2011.

[274] Knight, J. C., Cheung, G., Jacques, F. and Birks, T. A., *Phase-matched excitation of whispering-gallery-mode resonances by a fiber taper*, Opt Lett, **22**(15), 1129-1131, 1997.

[275] Kapitonov, A. M. and Astratov, V. N., *Observation of nanojet-induced modes with small propagation losses in chains of coupled spherical cavities*, Opt Lett, **32**(4), 409-411, 2007.

[276] Yang, S. and Astratov, V. N., *Photonic nanojet-induced modes in chains of size-disordered microspheres with an attenuation of only 0.08 dB per sphere*, Appl Phys Lett, **92**(26), 2008.

[277] Kato, D., *Light coupling from a stripe-geometry GaAs diode laser into an optical fiber with spherical end*, J Appl Phys, **44**(6), 2756-2758, 1973.

[278] Paek, U. C. and Weaver, A. L., *Formation of a spherical lens at optical fiber ends with a CO_2 laser*, Appl Optics, **14**(2), 294-298, 1975.

[279] Tanaka, A., Asai, T., Toubaru, K., Takashima, H., Fujiwara, M., Okamoto, R. and Takeuchi, S., *Phase shift spectra of a fiber-microsphere system at the single photon level*, Opt Express, **19**(3), 2278-2285, 2011.

[280] Wang, P. F., Lee, T., Ding, M., Dhar, A., Hawkins, T., Foy, P., Semenova, Y., Wu, Q., Sahu, J., Farrell, G., Ballato, J. and Brambilla, G., *Germanium microsphere high-Q resonator*, Opt Lett, **37**(4), 728-730, 2012.

[281] Cai, M. and Vahala, K., *Highly efficient hybrid fiber taper coupled microsphere laser*, Opt Lett, **26**(12), 884-886, 2001.

[282] White, I. M., Hanumegowda, N. M., Oveys, H. and Fan, X. D., *Tuning whispering gallery modes in optical microspheres with chemical etching*, Opt Express, **13**(26), 10754-10759, 2005.

[283] Totsuka, K. and Tomita, M., *Slow and fast light in a microsphere-optical fiber system*, J Opt Soc Am B, **23**(10), 2194-2199, 2006.

[284] Fan, K. C., Hsu, H. Y., Hung, P. Y. and Wang, W. L., *Experimental study of fabricating a microball tip on an optical fibre*, J Opt a-Pure Appl Op, **8**(9), 782-787, 2006.

[285] Ma, J., Ju, J., Jin, L., Jin, W. and Wang, D. N., *Fiber-tip micro-cavity for temperature and transverse load sensing*, Opt Express, **19**(13), 12418-12426, 2011.

[286] Wang, M. M., Jiang, L., Wang, S. M., Tan, X. D. and Lu, Y. F., *A robust fiber inline interferometer sensor based on a core-offset attenuator and a microsphere-shaped splicing junction*, Opt Laser Technol, **63**, 76-82, 2014.

[287] Dong, C. H., He, L., Xiao, Y. F., Gaddam, V. R., Ozdemir, S. K., Han, Z. F., Guo, G. C. and Yang, L., *Fabrication of high-Q polydimethylsiloxane optical microspheres for thermal sensing*, Appl Phys Lett, **94**(23), 2009.

[288] von Klitzing, W., Jahier, E., Long, R., Lissillour, F., Lefevre-Seguin, V., Hare, J., Raimond, J. M. and Haroche, S., *Very low threshold lasing in Er3+ doped ZBLAN microsphere*, Electron Lett, **35**(20), 1745-1746, 1999.

[289] Hayakawa, T., Ooishi, H. and Nogami, M., *Optical bistability of stimulated-emission lines in Sm3+-doped glass microspheres*, Opt Lett, **26**(2), 84-86, 2001.

[290] Elliott, G. R., Hewak, D. W., Murugan, G. S. and Wilkinson, J. S., *Chalcogenide glass microspheres; their production, characterization and potential*, Opt Express, **15**(26), 17542-17553, 2007.

[291] Ward, J. M., Wu, Y. Q., Khalfi, K. and Chormaic, S. N., *Short vertical tube furnace for the fabrication of doped glass microsphere lasers*, Rev Sci Instrum, **81**(7), 2010.

[292] Hutchens, T. C., Darafsheh, A., Fardad, A., Antoszyk, A. N., Ying, H. S., Astratov, V. N. and Fried, N. M., *Characterization of novel microsphere chain fiber optic tips for potential use in ophthalmic laser surgery*, J Biomed Opt, **17**(6), 2012.

[293] Kosma, K., Zito, G., Schuster, K. and Pissadakis, S., *Whispering gallery mode microsphere resonator integrated inside a microstructured optical fiber*, Opt Lett, **38**(8), 1301-1303, 2013.

[294] Braginsky, V. B., Gorodetsky, M. L. and Ilchenko, V. S., *Quality-factor and nonlinear properties of optical whispering-gallery modes*, Phys Lett A, **137**(7-8), 393-397, 1989.

[295] Ilchenko, V. S., Gorodetsky, M. L. and Vyatchanin, S. P., *Coupling and tunability of optical whispering-gallery modes - a basis for coordinate meter*, Opt Commun, **107**(1-2), 41-48, 1994.

[296] Gorodetsky, M. L., Savchenkov, A. A. and Ilchenko, V. S., *Ultimate Q of optical microsphere resonators*, Opt Lett, **21**(7), 453-455, 1996.

[297] Dubreuil, N., Knight, J. C., Leventhal, D. K., Sandoghdar, V., Hare, J. and Lefevre, V., *Eroded monomode optical-fiber for whispering-gallery made excitation in fused-silica microspheres*, Opt Lett, **20**(8), 813-815, 1995.

[298] Serpenguzel, A., Arnold, S. and Griffel, G., *Excitation of resonances of microspheres on an optical fiber*, Opt Lett, **20**(7), 654-656, 1995.

[299] Ilchenko, V. S., Yao, X. S. and Maleki, L., *Pigtailing the high-Q microsphere cavity: a simple fiber coupler for optical whispering-gallery modes*, Opt Lett, **24**(11), 723-725, 1999.

[300] Vernooy, D. W., Furusawa, A., Georgiades, N. P., Ilchenko, V. S. and Kimble, H. J., *Cavity QED with high-Q whispering gallery modes*, Phys Rev A, **57**(4), R2293-R2296, 1998.

[301] Kippenberg, T. J. and Vahala, K. J., *Cavity opto-mechanics*, Opt Express, **15**(25), 17172-17205, 2007.

[302] Ward, J. and Benson, O., *WGM microresonators: sensing, lasing and fundamental optics with microspheres*, Laser Photonics Rev, **5**(4), 553-570, 2011.

[303] Li, H. Y., Hao, S., Qiang, L. S., Li, J. and Zhang, Y. D., *Observation of whispering gallery modes in microtube-microspheres system*, Appl Phys Lett, **102**(23), 2013.

[304] Wang, H. Z., Lan, X. W., Huang, J., Yuan, L., Kim, C. W. and Xiao, H., *Fiber pigtailed thin wall capillary coupler for excitation of microsphere WGM resonator*, Opt Express, **21**(13), 15834-15839, 2013.

[305] Soria, S., Berneschi, S., Brenci, M., Cosi, F., Conti, G. N., Pelli, S. and Righini, G. C., *Optical microspherical resonators for biomedical sensing*, Sensors-Basel, **11**(1), 785-805, 2011.

[306] Ward, J. M. and Chormaic, S. N., *Thermo-optical tuning of whispering gallery modes in Er:Yb co-doped phosphate glass microspheres*, Appl Phys B-Lasers O, **100**(4), 847-850, 2010.

[307] Ma, R., Schliesser, A., Del'Haye, P., Dabirian, A., Anetsberger, G. and Kippenberg, T. J., *Radiation-pressure-driven vibrational modes in ultrahigh-Q silica microspheres*, Opt Lett, **32**(15), 2200-2202, 2007.

[308] Allen, K. W., Darafsheh, A., Abolmaali, F., Mojaverian, N., Limberopoulos, N. I., Lupu, A. and Astratov, V. N., *Microsphere-chain waveguides: Focusing and transport properties*, Appl Phys Lett, **105**(2), 2014.

[309] Darafsheh, A., Fardad, A., Fried, N. M., Antoszyk, A. N., Ying, H. S. and Astratov, V. N., *Contact focusing multimodal microprobes for ultraprecise laser tissue surgery*, Opt Express, **19**(4), 3440-3448, 2011.

[310] Dantham, V. R., Bisht, P. B. and Namboodiri, C. K. R., *Enhancement of Raman scattering by two orders of magnitude using photonic nanojet of a microsphere*, J Appl Phys, **109**(10), 2011.

[311] Riedl, M., Optical design fundamentals for infrared systems, Second ed., SPIE Press, Bellingham, WA, 2001.

[312] Darafsheh, A. and Astratov, V. N., *Periodically focused modes in chains of dielectric spheres*, Appl Phys Lett, **100**(6), 2012.

[313] Darafsheh, A., Mojaverian, N., Limberopoulos, N. I., Allen, K. W., Lupu, A. and Astratov, V. N., *Formation of polarized beams in chains of dielectric spheres and cylinders*, Opt Lett, **38**(20), 4208-4211, 2013.

[314] Jewell, J. M., *Thermooptic coefficients of some standard reference material glasses*, J Am Ceram Soc, **74**(7), 1689-1691, 1991.

[315] Schuster, K., Unger, S., Aichele, C., Lindner, F., Grimm, S., Litzkendorf, D., Kobelke, J., Bierlich, J., Wondraczek, K. and Bartelt, H., *Material and technology trends in fiber optics*, Adv. Opt. Techn., **3**(4), 447–468, 2014.

[316] Lee, G. C. B., Su, S., Li, J. L., Sugden, K., Roohpour, N., Yan, H. X. and Ye, H. T., *Analysis of femtosecond laser surface patterning on bulk single-crystalline diamond*, J Exp Nanosci, **7**(6), 662-672, 2012.

[317] Su, S., Li, J. L., Lee, G. C. B., Sugden, K., Webb, D. and Ye, H. T., *Femtosecond laser-induced microstructures on diamond for microfluidic sensing device applications*, Appl Phys Lett, **102**(23), 2013.

[318] Rothhardt, M., Chojetzki, C. and Mueller, H. R., *High mechanical strength single-pulse draw tower gratings*, Photonics North: Applications of Photonic Technology, Pts 1 and 2, **5579**, 127-135, 2004.

[319] Wieduwilt, T., Bruckner, S. and Bartelt, H., *High force measurement sensitivity with fiber Bragg gratings fabricated in uniform-waist fiber tapers*, Meas Sci Technol, **22**(7), 2011.